# Effect of atmospheric boundary layer inflow and wind yaw angle on the aerodynamics of heavy duty vehicles and attached boat-tails

Prayash Panda

**Supervisor**
Dr. Marc Gerritsma
Professor
TU Delft

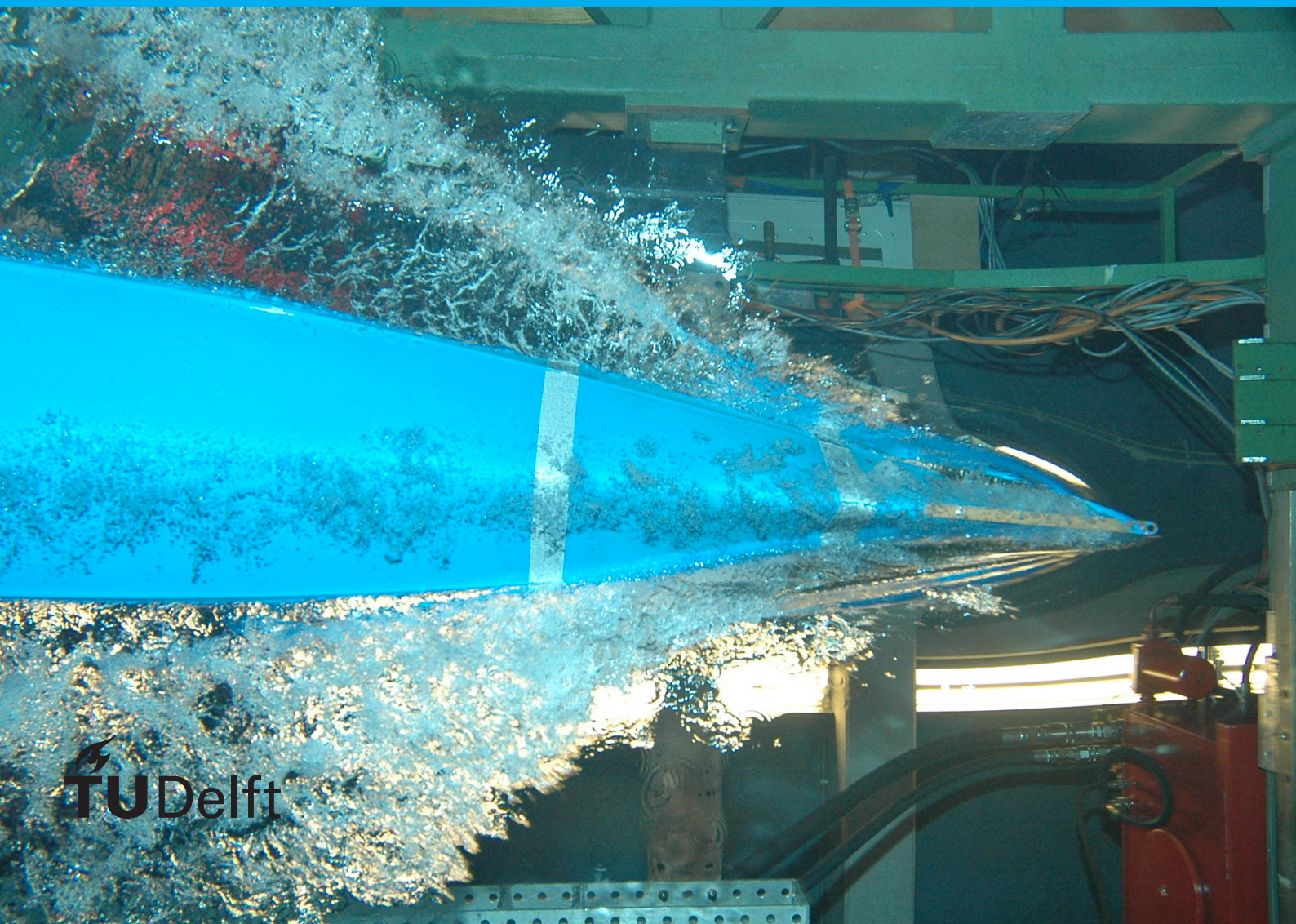

# Effect of atmospheric boundary layer inflow and wind yaw angle on the aerodynamics of heavy duty vehicles and attached boat-tails

by

Prayash Panda

to obtain the degree of Master of Science
at the Delft University of Technology,
to be defended publicly on Thursday October 31, 2019 at 2:00 PM.


| | | |
|---|---|---|
| Student number: | 4722493 | |
| Project duration: | April 1, 2019 – October 31 , 2019 | |
| Thesis committee: | Prof. dr. ir. M. I. Gerritsma, | TU Delft, supervisor |
| | Dr. R. P. Dwight, | TU Delft |
| | Ir. R. Veldhuizen, | WABCO Optiflow |


An electronic version of this thesis is available at `http://repository.tudelft.nl/`.

TU Delft

# Preface

During my M.Sc. studies, my interests leaned towards applied computational fluid dynamics. During my search for a thesis topic, I found this topic to be intriguing and challenging. This thesis which investigates the effect of an atmospheric boundary layer inflow on the aerodynamics of trucks taught me all the aspects involved in applied CFD such as modelling, meshing, solving etc. The work presented is a culmination of months of hardwork.

I would like to thank my friends who provided both sound advice and necessary respite during stressful times. They ensured that I never burned out because of the workload.

I would also like to thank my daily supervisors Marc Gerritsma and Roy Velduizen who provided insights which helped me to look at my results from a different perspective, taught me how to be critical about scientific results and how one needs to support their theory. These skills have helped me grow towards being a better professional. Both Marc and Roy took out time from their busy schedule to ensure that I could graduate in October.

A special thanks goes to Ankith for guiding me with the ANSYS Workbench interface and to Sampath for helping me out with Tecplot.

Finally, I would like to thank my family who have always been supportive not only during the thesis but throughout my M.Sc. studies at Delft. Without their financial backing, my M.Sc. journey in Delft would not have been this enjoyable.

*Prayash Panda*
*Delft, October 2019*

# Summary

Greenhouse gas emissions have globally increased temperatures and have led to global warming. A major part of these greenhouse gas emissions is emitted by motor vehicles in Europe. With an aim to limit global temperature increase by targeting emissions from heavy duty vehicles (HDV) which travel long-haul international journeys, this thesis aims to study the aerodynamics of heavy duty vehicles subjected to the inflow of an atmospheric boundary layer approaching the vehicle at a non-zero wind yaw angle.

Vehicles running on-road face a turbulent boundary layer which is generated due to friction from the earth's surface, also known as the atmospheric boundary layer (ABL). Current research literature on atmospheric boundary layers focuses on the aerodynamics of buildings when subjected to an atmospheric boundary layer. In such studies, the length scales of the geometry considered ranges in 10 to 100 m which is much greater than the scale of general heavy duty vehicles. The height of standard heavy duty vehicles ranges usually between 3 to 4 m, which pertains to the lower most region of the atmospheric boundary layer. Current literature has not yet focused on this lower region of the atmospheric boundary layer. Also, an atmospheric boundary layer does not necessarily approach the vehicle head-on and may come at a yaw angle. Considering studies investigating the effect of wind approaching the vehicle at a non-zero yaw angle, the inflow of an atmospheric boundary layer at a non-zero yaw angle may bring new insight into how the aerodynamics across the vehicle will be affected. Drag reduction devices are being widely used in the transportation industry to improve aerodynamic performance of heavy duty vehicles. One such device known as the boat-tail is attached to the trailer of a tractor-trailer configuration which aids in reducing drag by increasing base pressure. This study also aims to investigate how efficient the drag reduction mechanism of boat-tails is when subjected to the inflow of an atmospheric boundary layer which may approach the vehicle at a non-zero yaw angle.

Before investigating the effect of atmospheric boundary layer inflow on heavy duty vehicles, empty domain simulations are carried out to simulate solely the ABL. ANSYS Fluent is used with the SST $k-\omega$ model to solve the RANS equations. The logarithmic law is used to model the ABL. Wall sand-grain roughness $k_S$ is introduced to model elements of a realistic environment such as trees, buildings, other on-road vehicles etc. Appropriate values of turbulence intensity and turbulence length scale are chosen which are observed in a realistic environment. The aim of these simulations is to minimise the development of the ABL profile specified at the inlet. This is done to ensure that the vehicle geometry faces an ABL profile which is as close to the inlet profile as possible. The maximum deviation from the inlet profile is limited to 1 % at $z < 1\ m$ when the ABL profile crosses 25 $m$ from the inlet. This amount of deviation is considered as acceptable and the settings used in these simulations are then used as input for simulations involving the geometry. For simulations involving the HDV geometry, the maximum deviation from the inlet profile is limited to 2 % at $z < 1\ m$ when the ABL profile reaches 10 m in front of the HDV.

The GETS model is used to study the aerodynamics across an HDV for the thesis work. A computational domain of dimensions specified by SAE protocol is prepared. Refinement boxes are introduced to better capture areas of interest. A mesh sensitivity study is done to study the effects of discretisation on the drag coefficient. Validation of the settings used is carried out by comparing the results with wind tunnel studies by van Raemdonck.

To be able to compare the effect of an ABL inflow condition with constant velocity inflow, two cases are prepared namely the ABL inflow case (referred to as ABL) and the constant inlet velocity case (referred to as 'No-ABL'). The only difference in settings between the two cases is the inlet velocity profile. The constant velocity (referred to as $V_{T,eq}$ experienced at $z = z_{eq}$) for the 'No-ABL' case is calculated by equating the mass flow over the HDV height for both the cases. The ABL case faces higher velocities above $z_{eq}$ (4 % higher near the HDV's top surface) and lower velocities below $z_{eq}$ (3 % lower near the HDV's bottom surface), compared to the 'No-ABL' case. The portion of the HDV above $z_{eq}$ constitutes 74% of the total HDV volume.

Since higher velocities for the ABL case are experienced over a larger volume of the HDV, the ABL case faces 17% higher front surface drag and 2% higher side surface drag compared to the 'No-ABL' case. This finding is backed by higher pressure on the front surface and higher wall shear stress on the side surface above $z_{eq}$. Lower pressures on the rear surface and lower velocities in the wake region lead to 2% higher rear drag for the ABL case. The total drag comes out to be 3.5% higher for the ABL case. Considering the volume above $z_{eq}$, the ABL case has 5% higher drag, while for the volume below $z_{eq}$, the 'No-ABL' case has 3 % higher drag.

The efficiency of the drag reduction caused by the boat-tail is virtually unaffected by the ABL inflow effect. For both the cases, the drag reduction is 20 %. This occurs because the boat-tail reduces the rear surface pressure difference between the ABL and 'No-ABL' case to just 2 Pa. The boat-tail thus increases the base pressure by a higher amount for the ABL case.

Non-zero relative wind yaw angle $\psi$ is introduced by inducing crosswinds at both the inlets. Similar to the procedure for calculating $V_{T,eq}$, $\psi_{T,eq}$ is also calculated through trial and error method to obtain a value of 5°. The value of 5° is chosen after extensive literature study on yaw angles faced by on-road vehicles. The high pressure core near the front surface stagnation region shifts to the windward side of the HDV. This shifting is higher for the ABL case above $z_{eq,yaw}$ and lower for the ABL case below $z_{eq,yaw}$. This occurs because due to the ABL inflow, $\psi$ also varies in the z-direction, similar to how the velocity differs. While the side drag and rear drag for the ABL case are higher by 2.5% and 4%, the front drag is lower by 5.5%. Such a trend is caused by higher wall shear stress above $z_{eq,yaw}$, lower rear surface pressures and lower front surface pressures for the ABL case. Considering the volume above $z_{eq,yaw}$, the ABL case has 3% higher drag, while for the volume below $z_{eq,yaw}$, the ABL case has 2 % higher drag. Even though lower velocities are observed for the ABL case below $z_{eq,yaw}$, because of much lower rear surface pressures below $z_{eq,yaw}$ for the ABL case, the rear drag increase compensates for the lower velocities faced.

The ABL cases with and without the relative wind yaw angle $\psi$ are compared. Since $\psi$ is applied solely to the ABL wind profile $V_w(z)$ and not to the driving velocity, the equivalent velocity $V_{T,eq}$ faced by the vehicle when approached by a yawed ABL inflow actually decreases. This leads to higher pressures on the front surface, higher decelaration in the wake region and higher wall shear stress on the side surface for the zero $\psi$ case. This causes 44% lower front drag, 1.5% lower side drag and 0.5% lower rear drag. The combination of a lower equivalent velocity and the low sensitivity in terms of drag of the GETS model to changes in $\psi$ together lead to 5.5% lower drag for the 5° equivalent $\psi$ case.

The drag reduction efficiency of the boat-tail under a non-zero $\psi$ is once again practically unaffected by the ABL inflow effect. The drag reduction is approximately 20 % for both the ABL and 'No-ABL' cases. However, the difference between the ABL and 'No-ABL' cases is slightly larger when $\psi$ is non - zero. The rear surface pressure differences increase from 2 Pa for the zero $\psi$ case to 4.5 Pa for the non-zero $\psi$ case.

*Prayash Panda*
*Delft, October 2019*

# Contents

# List of Figures

# List of Tables

# Nomenclature

## Symbols

| | | |
|---|---|---|
| $z_O$ | Surface roughness | $m$ |
| $k_S$ | Sand grain roughness | $m$ |
| $y_P$ | Distance from wall to half height of wall-adjacent cell | $m$ |
| $y^+$ | Non-dimensional wall distance | - |
| $\alpha$ | Power law exponent | - |
| $\kappa$ | von Karman constant | - |
| $\rho$ | Density | $kg/m^3$ |
| $S$ | Wetted surface area | $m^2$ |
| $\psi$ | Relative wind yaw angle | - |
| $C_P$ | Pressure coefficient | - |
| $C_{pmb}$ | Mean base pressure coefficient | - |
| $C_f$ | Skin friction coefficient | - |
| $C_L$ | Lift coefficient | - |
| $C_S$ | Side force coefficient | - |
| $C_s$ | Roughness constant | - |
| $C_D$ | Drag coefficient | - |
| $p$ | Pressure | $[Pa]$ |
| $Re$ | Reynolds number | - |
| $C_{D_{wa}}$ | Wind averaged drag coefficient | - |
| $\phi$ | Wind angle | - |
| $\mu$ | Dynamic viscosity | $kg/(ms)$ |
| $\nabla.$ | Divergence operator | |
| $\nu$ | Kinematic viscosity | $m^2/s$ |
| $\sigma$ | Standard deviation | - |
| $\tau$ | Wall shear stress | $Pa$ |
| $u^*$ | Friction velocity | $m/s$ |
| $V_{HDV}$ | Driving velocity | $m/s$ |
| $V_T$ | Total relative velocity | $m/s$ |
| $V_w$ | Wind velocity | $m/s$ |

# Abbreviations

| | |
|---|---|
| ABL | Atmospheric Boundary Layer |
| HDV | Heavy Duty Vehicle |
| PIV | Particle Image Velocimetry |
| CFD | Computational Fluid Dynamics |
| EU | European Union |
| TI | Turbulence Intensity |
| TLS | Turbulence length scale |
| RSO | Road side obstacles |
| RANS | Reynolds Averaged Navier Stokes |
| GETS | Generalized European Transport System |
| SAE | Society of Automotive Engineers |
| SST | Shear Stress Transport |
| BC | Boundary condition |
| WSS | Wall shear stress |
| VP | Velocity plane |
| IBL | Internal boundary layer |
| USA | United States of America |

# 1 Introduction

## 1.1. Background

Global increase in temperatures, caused mainly by greenhouse gas emissions has given rise to climate change which has caused melting of snow at the poles, sea level rise and death of flora and fauna. Human-induced warming reached approximately $1°C$ above pre-industrial levels in 2017, according to The Intergovernmental Panel on Climate Change [20].

Figure 1.1 shows that 28 % of total U.S. greenhouse gas emissions by economic sector in 2016 arise from the transportation industry. The largest sources of transportation-related greenhouse gas emissions include passenger cars and light-duty trucks.

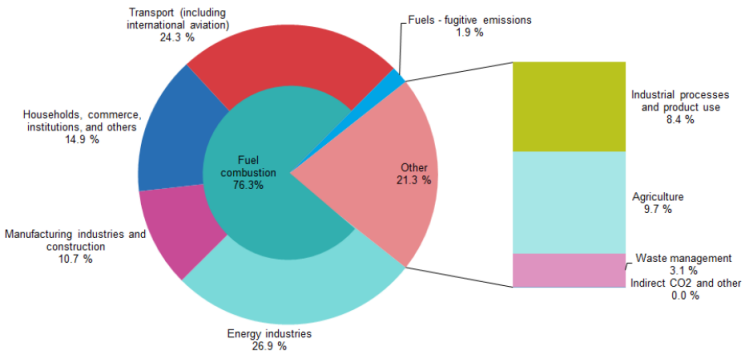


**Figure 1.1:** Greenhouse gas emissions by sector in the EU for 2016 [12]

According to International Council on Clean Transportation [24], HDVs are responsible for one-third of CO2 emissions in the EU resulting from transportation, which totals to 7% of total CO2 emissions. This is depicted in Figure 1.2. Seven member states (Germany, Poland, Spain, France, United Kingdom, Italy, and The Netherlands) are responsible for approximately three-quarters of the HDV CO2 emissions. The efficiency of tractor-trailers, the highest CO2 emitting segment in the EU, has remained constant for more than a decade [24].

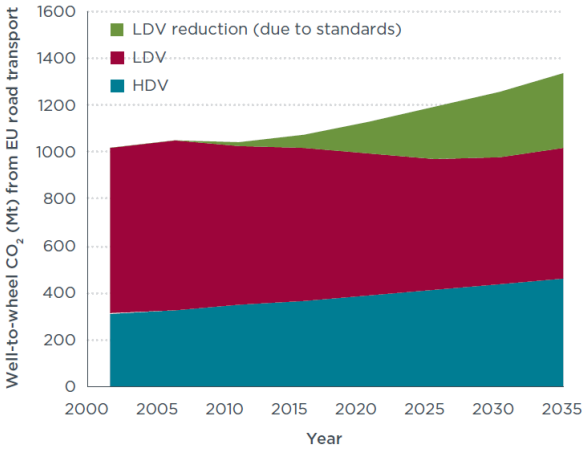


**Figure 1.2:** Road transport $CO_2$ emissions in the EU between 2000 and 2035 [24]

According to van Raemdonck [30] and as depicted in Figure 1.3, when the vehicle is driving at long-haul trajectories with a high constant vehicle velocity, almost 40 % of the engine delivered power is used to overcome the aerodynamic drag forces. Thus, efforts made to overcome the aerodynamic drag force can result in less total power requirement and thus fuel can be saved.

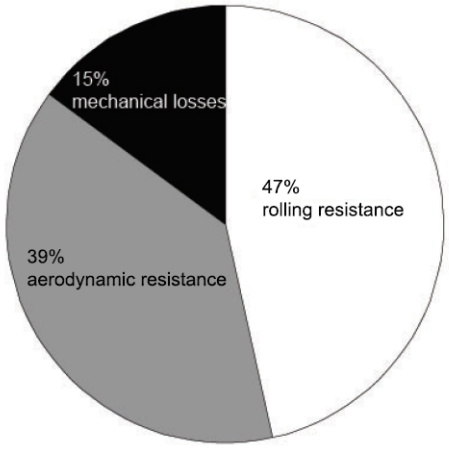


**Figure 1.3:** Percentage of the total engine delivered power used to overcome various losses/resistance for vehicles driving with a velocity of 23 $m/s$ or higher [30]

The U.S. Environmental Protection Agency estimates that improving the aerodynamics of typical U.S. combination trucks can improve fuel economy by up to 15 % (Curry [32]). On 17 May 2018, the European Commission presented a legislative proposal, setting CO2 emission standards for HDVs in the EU. From 2025, 15% lower average CO2 emissions than in 2019 and from 2030, at least 30% lower average CO2 emissions than in 2019 has been targeted.

The proposal will reduce fuel consumption costs and has provided an incentive to HDV manufacturers to adopt aerodynamic add-on devices to increase fuel savings. This, in turn motivates companies such as WABCO Optiflow to design such devices which enhance aerodynamics, reduce drag, reduce fuel consumption and thus reduce CO2 emissions.

To be able to design aerodynamic devices for HDVs so as to improve their aerodynamic performance, one needs to study bluff body aerodynamics, since HDVs by their design are bluff bodies. This shall be studied in the next chapter.

# 1.2. Bluff body aerodynamics

It is necessary to understand the aerodynamics associated with bluff bodies, as HDVs are in essence, bluff bodies. This chapter shall study how aerodynamics of bluff bodies is different from streamlined bodies such as airfoils and how this knowledge of aerodynamics is used to build aerodynamic devices for HDVs in the subsequent chapter.

## Aerodynamic drag

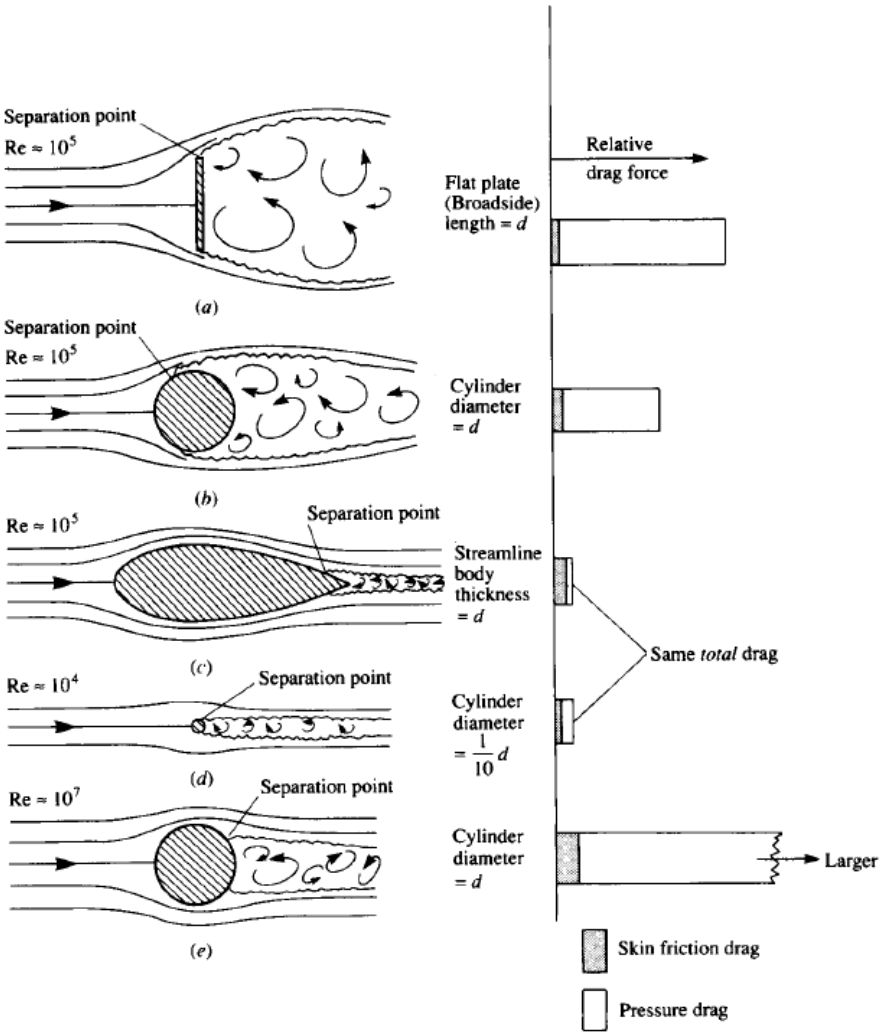


**Figure 1.4:** Relative comparison between skin friction and pressure drag for various aerodynamic shapes [3]

Every object, regardless of its geometry, experiences a retarding force called aerodynamic drag which occurs when the object is moved through a fluid (in this case, air). The drag force experienced depends on several factors such as velocity of air-flow/velocity of the moving object, density of air, the size and shape of the object, and also the surface roughness. One should note that drag will be discussed only in the incompressible regime (Mach number < 0.3).

The equation which relates the drag force on an object to its drag coefficient $C_D$ by incorporating the above mentioned factors, is expressed as follows (Anderson [3]):

$$\mathbf{D} = \frac{1}{2}\rho V^2 S C_D, \tag{1.1}$$

where, S represents the reference area, $C_D$ the drag coefficient, $\rho$ the density and $V$ the velocity. Drag force experience by a body is affected by the air's viscosity and compressibility, the size and shape of the body, and the body's inclination to the flow. In general, all these dependencies are complex as they result in a flow field around the body which determines the $C_D$. To deal with these complex dependencies, a single variable called the drag coefficient $C_D$ is introduced. (NASA [25])

## Types of drag in incompressible regime

As explained in Anderson [3], aerodynamic drag on an object is generally composed of two components - skin friction drag and pressure drag. Skin friction drag is drag occurring due to the shear stress exerted by the air on the body surface. Pressure drag is due to the differences in the pressure distribution over the body surface. The ratio of these two components is useful in identifying the difference between a bluff body and a streamlined body, as shown in Figure 1.4.

Aerodynamic bodies such as an airfoil experience less pressure drag. This is because the flow field around aerodynamic bodies is not very different from that corresponding to potential flow, apart from the displacement effect of the boundary layer (Buresti [5]). Therefore, the pressure distribution is only slightly different from the potential one. Consequently, the pressure in the aft part of the body has values which don't differ much from those acting on the front part. Thus, the resulting pressure drag is small. The main contribution to the drag of an aerodynamic body comes from tangential viscous stresses which lead to skin friction drag.

However, for bluff bodies, because of boundary layer separation, reattachment in the rear part of the body does not occur, due to which the pressure in this region is considerably smaller than pressure in the front. This gives rise to significant pressure drag. It is much higher than friction drag.

Figure 1.4 shows that bluff bodies such as cylinders have higher pressure drag. Buresti [5] states that bluff bodies are characterized by a premature separation of the boundary layer from their surface, large wakes varying spatio-temporally and unsteady velocity fields.

## Bluff body wake formation

As fluid approaches the HDV, due to viscosity, boundary layer starts developing from the anterior region of the vehicle. As flow traverses downstream, boundary layer thickness increases. Towards the rear end, due to a sudden change in flow passage area, the boundary layer separates leading to a low pressure turbulent wake downstream, as shown in Figure 1.5.

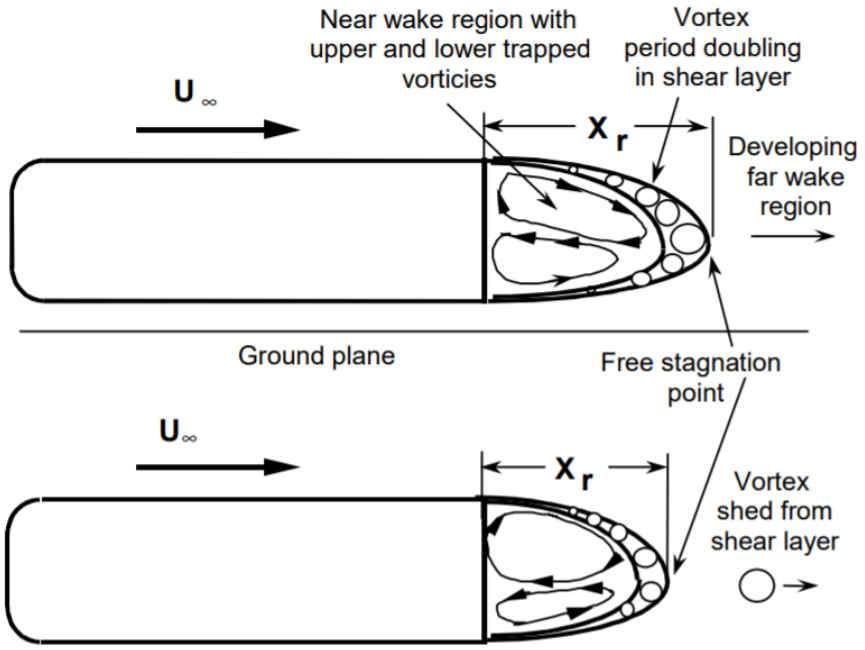


**Figure 1.5:** Unsteady near and far wake development mechanism [11]

The time averaged wake contains a ring vortex enclosed by shear layers which start where the boundary layer separates from the body (Duell [11]). As these vortices convect along the shear layer, vortex pairing is observed as shown in Figure 1.5. Pairing continues until the shear layers from all sides coalesce at the free stagnation point. The vortices are shed periodically into the far wake from the free stagnation point. The free stagnation point of a separated flow is actually a quasiperiodically fluctuating point that shifts as vortices are shed from the shear layer that bounds the recirculation region. The vortex pairing continues along the shear layer, increasing the size of the vortices, until they are shed from the near wake region at the free stagnation point.

The fluid that exits the near wake at the free stagnation point in the form of a vortex balances the fluid that is entrained into the near wake through the shear layers. As fluid is entrained, the amount of fluid in the near wake increases along with the recirculation length. Recirculation length is defined as the distance between the model base and the mean location of the free stagnation point (Duell [11]). When the recirculation length reaches a critical size, the near wake becomes unstable and a vortex is shed at the free stagnation point. This moves the free stagnation point closer to the body and reduces the size of the near wake. This periodic process provides an explanation for the pumping phenomena in the unsteady near wake.

## Reynolds number $Re$ and effect of turbulence

One of the most important parameters defining aerodynamic flow behaviour is the Reynolds number. It is physically a measure of the ratio of inertial forces to viscous forces in a flow. It was devised by Osborne Reynolds, while researching instabilities and turbulence in fluid flow. Reynolds number, Re, can be defined as follows:

$$\mathbf{Re} = \frac{vL}{\nu}, \tag{1.2}$$

where L is a characteristic dimension of the body, $\nu$ is the kinematic viscosity and v is the flow velocity.

For heavy duty vehicles, due to the shape of the body being blunt in nature, the characteristic dimension normally chosen is the width, height or square root of the frontal area of the vehicle (Raemdonck [30]).

Reynolds number is a parameter which defines the type of flow - laminar, transition or turbulent. Turbulent flow is achieved as the Reynolds number increases to sufficiently high values. Considering HDVs, since the velocity and characteristic dimension are high, the Reynolds number of the flow is in the region of 2-5 million. This leads to turbulence at the inflow or the flow becoming turbulent as it passes the HDV due to instabilities which occur due to viscosity or surface roughness (Tsinober [35]).

Choice of Reynolds numbers for numerical or experimental simulations is thus very critical, as the wrong value of $Re$ can give inaccurate values of $C_D$. In Figure 1.4, the drag coefficient varies based on the Reynolds number chosen for all bodies. Thus, performing an aerodynamic drag analysis in an unrepresentative $Re$ region can give a wrong result [30].

Due to the turbulent, highly viscous and unsteady nature of the flow field around them, these bodies cannot undergo simplified mathematical treatment and flow field variables need to be evaluated either from the solution of the complete Navier-Stokes equations or from experiments.

## Turbulence intensity and length scale

As mentioned above that a large portion of the flow surrounding a bluff body is turbulent in nature, apart from the Reynolds number, two more important turbulence properties which also need to be studied are turbulence intensity and turbulence length scale.

The turbulence intensity represents the magnitude of turbulent fluctuations [22], and the turbulence length scale represents the size of the main energy-containing eddies in the flow [22].

McAuliffe [22] extensively tested, on road, the flow behaviour around a full scale vehicle by means of probes attached to the vehicle and the main properties studied were the turbulence intensities and length scales around the vehicle. The turbulence intensities and length scales depend on several factors, most importantly wind speed, type of surroundings, height of surroundings and wind direction. Turbulence intensity and length scale affect the flow-field of the HDV and its wake. This shall eventually affect the drag faced by the HDV and thus turbulence intensity and length scale are governing parameters in HDV simulations, which is also shown in Cooper [6].

Turbulence intensity can be defined as:

$$T.I. = \frac{\sqrt{\frac{1}{3}.\left(\overline{u'^2} + \overline{v'^2} + \overline{w'^2}\right)}}{U}, \tag{1.3}$$

where $\overline{u'^2}, \overline{v'^2}, \overline{w'^2}$ are the time averaged components of the turbulent fluctuation velocity. The average of these fluctuations is divided by a local time-averaged velocity $U$.

For the traditional CFD approach, low turbulence parameters are usually specified. For the turbulent intensity a default value of 1% is used and for the turbulent length scale 0.01 m.

However, in the real world driving environment, Cooper and Watkins [10] indicated that most likely the turbulent intensity will be around 5% while the length scale ranges from a few meters to 30$m$.

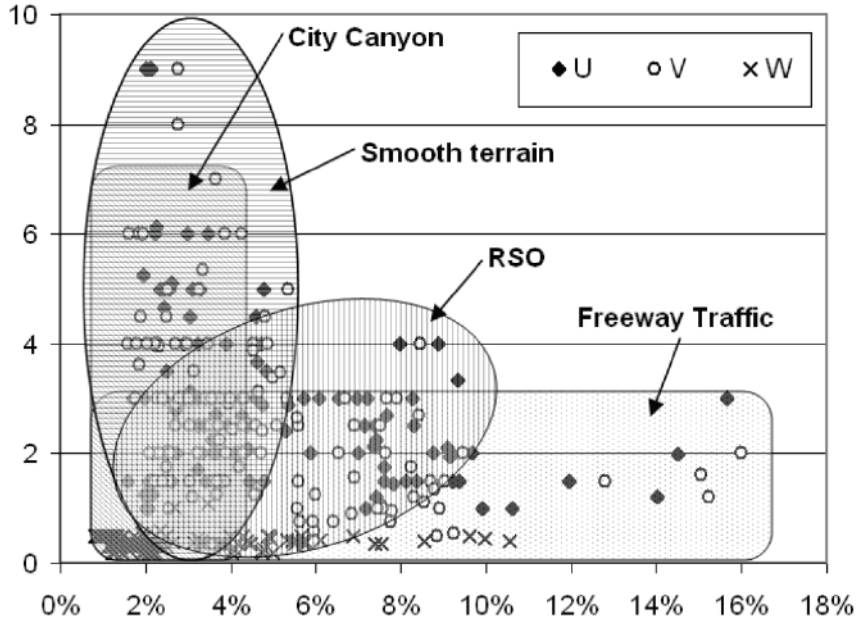


**Figure 1.6:** Turbulent length scale versus the turbulent intensity for various terrain types [43] (RSO - Roadside obstacles)

Wordley and Saunders [43] showed the results of measurements of turbulent intensity and turbulent length scale on different terrain types in Figure 1.6. The measurements were performed close to 25$m/s$, which is the highway driving speed of a tractor-trailer configuration. They indicated that all datasets overlapped for the region with turbulent intensity up to 5% and a length scale of 5 m.

To conclude, a turbulent intensity of 5% and turbulent length scale of 5 m will be the most appropriate to simulate realistic on-road conditions.

## 1.3. HDVs as bluff bodies

According to van Raemdonck [30], HDVs, being bluff bodies face drag profiles similar to that of bluff bodies since they have large separated flow regions behind, due to the blunt rear end of the vehicle.

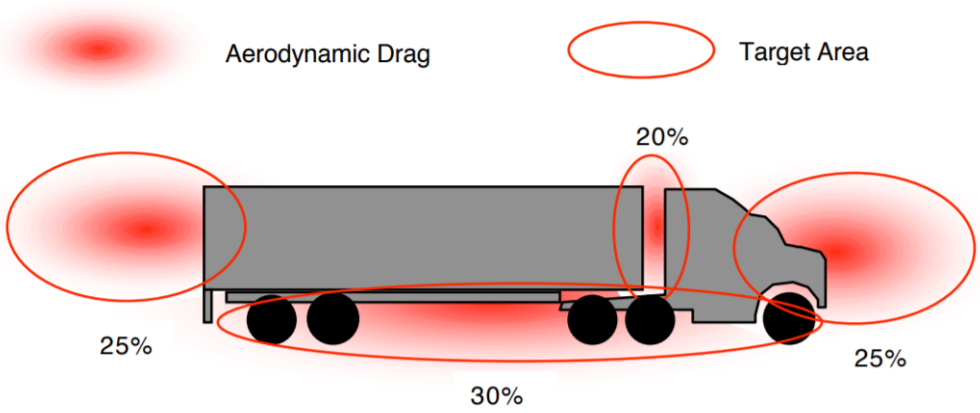


**Figure 1.7:** Contributions to total drag from various components of an HDV [42]

Figure 1.7 shows the regions which are the major contributors of drag faced by an HDV. One can conclude that the biggest contributions to HDV drag come from the posterior region, the tractor-trailer gap, the anterior region and the underbody.

The identification of these contributors has inspired the academia and the industry to research innovative aerodynamic devices which shall utilise flow control techniques to ameliorate the aerodynamics of the flow across an HDV and thus mitigate the aerodynamic drag faced. Since HDVs traverse large distances, an improvement in the flow field shall result in considerable fuel savings and thus lower CO2 emissions.

Figure 1.8 shows an illustration of various such aerodynamic devices that can be attached to a tractor-trailer combination [16].

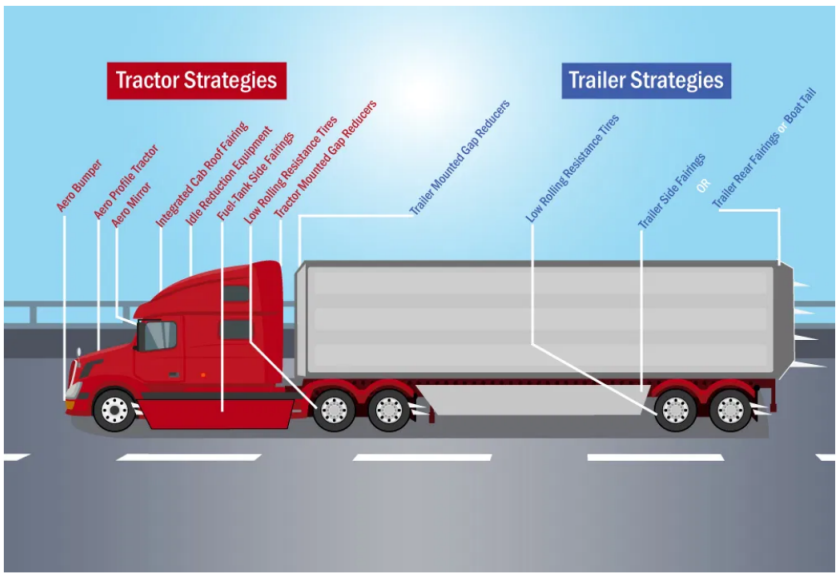


**Figure 1.8:** A schematic showing the several types of aerodynamic devices on an HDV in the USA [16]

For the purpose of our thesis, we focus on the boat-tail. As explained before and depicted in Figure 1.5, the trailer posterior region contributes significantly to total drag. Cooper [9] defines boat-tail as an inflatable or folding fairing attached to the rear of the trailer which is inclined at a certain angle to the base region. It reduces pressure drag by increasing base pressure, thus aiding in pressure recovery. It does so by making the change in geometry less abrupt, thus improving the aerodynamic shape of the HDV, as shown in Figure 1.9. By increasing the base pressure, the pressure difference across the front and back of an HDV decreases. According to Cooper [9], a 3-sided Maka BoatTail$^{TM}$ provides 688 US gallons of annual savings for one conventional tractor-trailer, based on an assumed 20,000 annual miles at 65 mph.

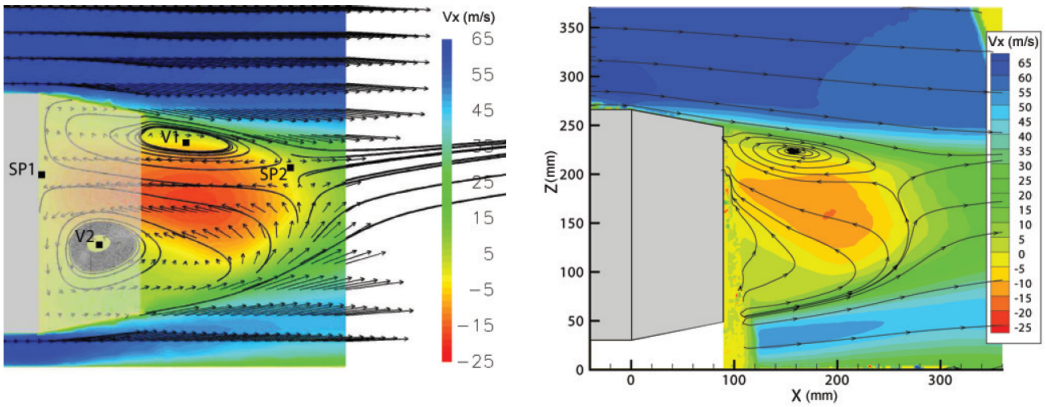


(a) numerical simulation (b) PIV measurements

**Figure 1.9:** Typical flow field behind a rear mounted boat-tail [30]

# 1.4. Atmospheric Boundary Layer

We have now studied the aerodynamics of HDVs and attached boat-tail. However, it must be noted that these studies have been performed in idealistic conditions and have not taken realistic operating conditions into account. It is imperative that taking into account real world operating conditions will not alter the physics we studied but will instead add details and bring changes in magnitudes of physical quantities. Qualitative deviations won't be observed.

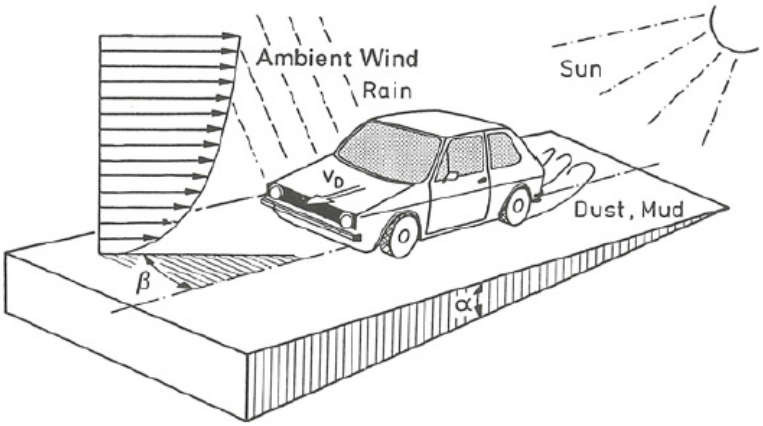


**Figure 1.10:** A road vehicle in its real environment [30]

An international long-haul HDV is subjected to several operating conditions during its journey. Changing weather conditions, especially crosswinds and gusts, have an influence on aerodynamic flow behaviour around road vehicles and thus their energy consumption. Rain and the accumulation of dust and snow also have an effect on the vehicles efficiency. The inclination of the road, i.e. driving through mountainous areas and the presence of the Earth's boundary layer called the Atmospheric Boundary Layer (ABL) at the vehicle's anterior have also been identified as an important factor for fuel consumption. An overview of these conditions is illustrated in Figure 1.10.

We focus on the effect of the ABL on the aerodynamics across an HDV in this section and the effect of the presence of a non-zero relative wind yaw angle in the next section.

## Definition

Boundary layers are generated over a surface due to viscosity retarding the flow of fluid very close to the surface. Since fluids are abundant in our environment, boundary layers are a common phenomenon, observed

over automotives, airplanes, naval vehicles etc.

Chen [39] states that Earth also, has its own boundary layer, which is termed as the Atmospheric Boundary Layer (ABL). Similar to boundary layers, the friction of the Earth's surface leads to the ABL, which has zero wind speed at the surface and keeps increasing till it reaches a constant value at the boundary layer thickness (which occurs in the range of 100s of metres). The shape and height of the ABL depends on the surface roughness length $z_O$.

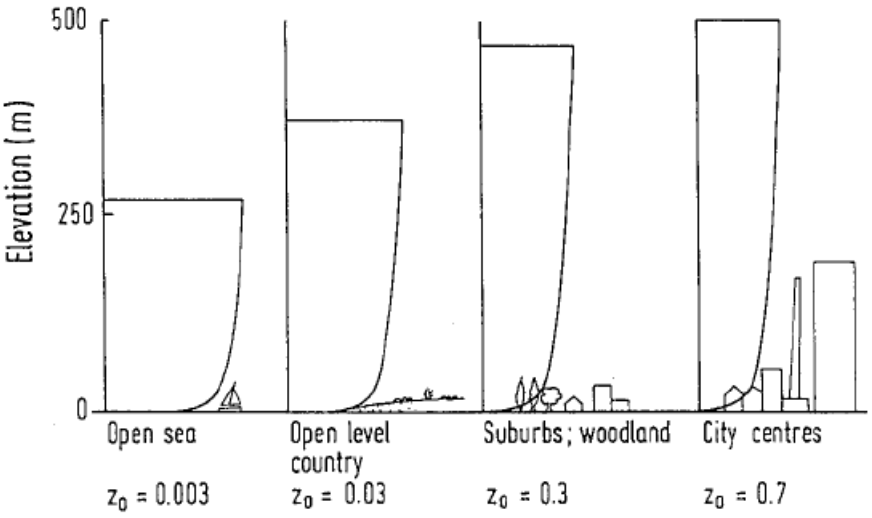


FIGURE 12.47: Mean wind profiles for different terrains.

**Figure 1.11:** Surface roughness classification
[39]

**Surface roughness length** $z_O$- According to Larsen [19], the roughness length $z_O$ is the height at which the ABL profile extrapolates to zero due to surface friction. It must be noted that it is not a physical length by itself but actually a representation of the length scale of the roughness elements on the surface. Depending on the terrain, one can determine the roughness in a particular environment. Roughness elements include natural and man-made structures such as different forms of vegetation and building infrastructure.

In Figure 1.11, one can get an idea of the measure of the surface roughness $z_O$ based on the environment and the elements in it. As we go from open sea to the city centre, we observe that the number of elements in the environment increase which act as roughness elements and thus increase the surface roughness.

One must note that theoretically, we only concern ourselves with the near neutrally stable ABL which is statistically stationary and horizontally homogeneous. Larsen [19] states that neutral stability indicates that there is no heat flux and water vapor flux between the surface and the atmosphere. Even though such assumptions may seem strict and unrealistic, realistic results can still be obtained such as ABL studies done by Blocken [4].

We begin by studying the laws which govern the ABL. Two kinds of law are prevalent in literature which define the ABL (Zaaijer and Vire [23]):

- **Log law** - Under near-neutral conditions, as defined earlier, $z_o$ is the surface roughness which lends shape to the ABL profile. U*, called the friction velocity lends magnitude to the ABL profile. $\kappa$ is the von Karman constant i.e. 0.4.

$$V(z) = \frac{u*}{\kappa} ln\Big(\frac{z+z_O}{z_O}\Big). \tag{1.4}$$

- **Power law** - By using a reference height $z_{ref}$ and the velocity at reference height $V(z_{ref})$, and an exponent $\alpha$ which represents the surface roughness and height range, and thus the shape of the ABL profile. The reference data imparts magnitude to the profile.

$$V(z) = V(z_{ref})\left(\frac{z}{z_{ref}}\right)^{\alpha}. \tag{1.5}$$

We wish to investigate the effect of the ABL on the drag experienced by an Heavy Duty Vehicle (HDV). Since, in reality, the HDV experiences Earth's ABL as inflow, it is prudent to observe how the airflow and thus the drag experienced, changes when constant freestream conditions are replaced by an ABL profile. This may also modify the streamline directing effect of aerodynamic devices such as tails (discussed before) since incoming flow conditions have changed.

Extensive studies, both computational and experimental, have been performed to study the aerodynamics of HDVs being driven in realistic environments, both with and without aerodynamic add-on products. However, not all studies have investigated the effect of the Atmospheric Boundary Layer (ABL). Inflow conditions in CFD simulations and incoming air in wind tunnel studies is often unidirectional, laminar and uniform. However, in reality, HDVs shall experience the Earth atmosphere's boundary layer which is a non-uniform, turbulent profile that may not approach the vehicle head-on but can have a certain yaw angle relative to the vehicle velocity.

We may utilise either of the two laws discussed above, to use the ABL as inflow condition for the HDV. For the sake of simplicity, only headwind direction is considered while using the ABL as inflow condition for the HDV in this thesis. However, commercial HDVs whose height ranges only up to 3-4 m (Raemdonck [30]) are in the lowermost region of the Atmospheric Boundary Layer. To be sure whether the laws can still be used for ABL simulations across an HDV, Panda [27] uses MATLAB's inbuilt genetic algorithm [21] to calculate parameters $\alpha$ and $z_0$ for the power law and the log law respectively such that the resulting ABL profile fits equally close to full scale experimental data sets obtained from Toloui [33] and Hutchins [15], as shown in Figure 1.12. The normalised SLTEST data and the PIV data in Figure 1.12 correspond to studies by Toloui [33] and Hutchins [15] respectively.

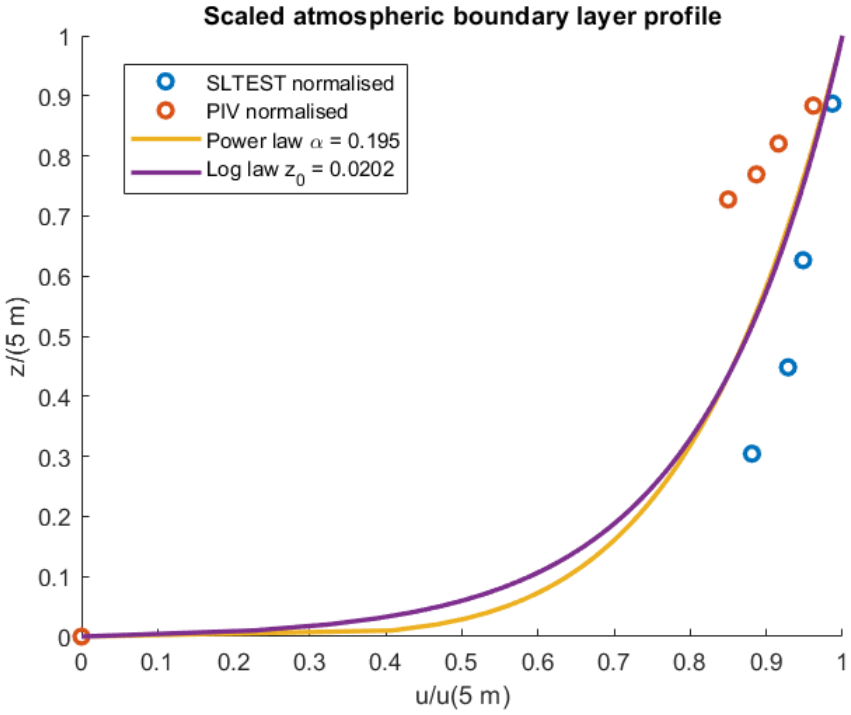


**Figure 1.12:** Optimisation to obtain $\alpha$ and $z_o$

Comparing the ABL profiles obtained by both the laws with their respective optimised parameters, to the full scale data sets, it can be observed that both laws are capable of giving a reasonably good fit at heights below 4 m, as long as one figures out the correct parameter ($\alpha$ or $z_0$) value.

Since both the laws give similar results, one can choose which one to proceed with. The only difference lies in the region z ≤ 2 m, where the log law is steeper than the power law. Since the log law deviates more from the constant freestream conditions compared to the power law, to observe changes brought in by the ABL, it is decided to use the logarithm law.

Computational research investigating the effect of ABL on HDV is slowly picking up and extensive literature isn't available yet. van Dijk [36] has attempted to study the effect of ABL as inflow on the flow field across an HDV for the XF and FAT HDV model.

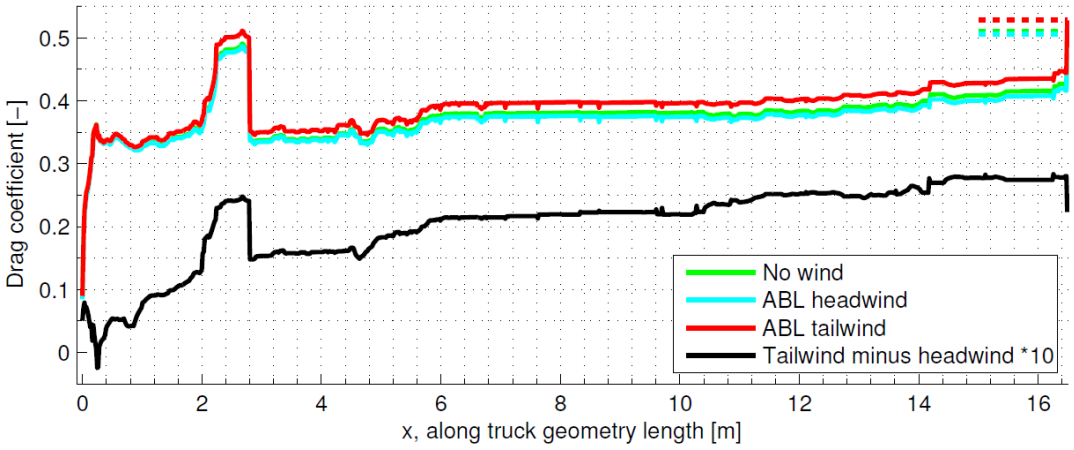


**Figure 1.13:** Accumulated drag coefficient over length of the XF truck model [36]

One can observe the difference in the drag coefficient trend with and without ABL as inflow condition. This shows that $C_d$ calculations which don't take into account ABL as inflow in on-road external aerodynamics may not give an accurate prediction.

This is why it is important to consider ABL as inflow condition for simulating airflow across an HDV in a realistic environment. van Dijk's [36] research investigates the effect of ABL on trailer side-skirts but not on rear boat-tails however. It is intuitive to assume that there will be a change in the aerodynamics due to the ABL for the boat-tail too.

# 1.5. Relative wind yaw angle

We discuss that a realistic environment always induces a non-zero yaw angle to the incoming wind which an HDV faces, by referring to existing literature. We proceed by elaborating on how a non-zero yaw angle can affect the aerodynamics and the drag characteristics of an HDV.

## Impact of crosswind

In the scenario of wind approaching a vehicle at a non-zero yaw angle, the vector schematic looks as shown in Figure 1.14.

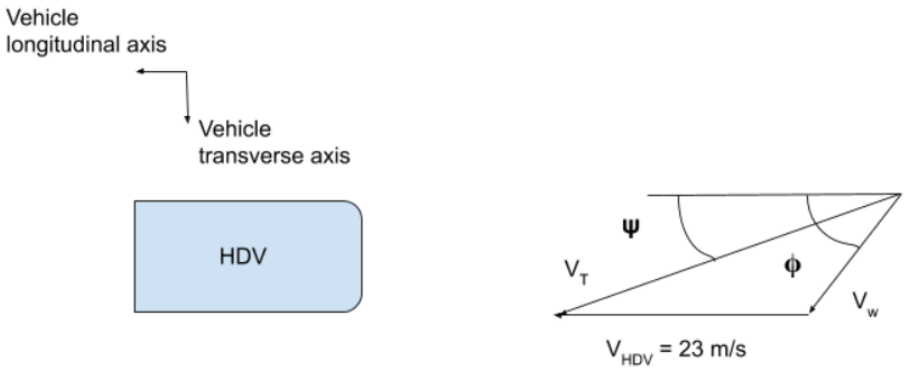


**Figure 1.14:** Wind vector schematic

The wind angle $\phi$ is the angle that the wind velocity $V_w$ makes with the driving velocity $V_{HDV}$ i.e. with the vehicle. $\psi$ is the relative wind yaw angle experienced by the vehicle while moving and is the angle between the total velocity $V_T$ and the driving velocity $V_{HDV}$.

If the vehicle is traveling at a velocity $V_{HDV}$ with respect to the roadway and the crosswind has a velocity $V_w$ acting at a wind angle $\phi$ with respect to $V_{HDV}$, the total velocity $V_T$ of the wind relative to the vehicle can be calculated by taking components of the vectors $V_{HDV}$ and $V_w$ along the vehicle's longitudinal and transverse direction. The total velocity $V_T$ then shall be the magnitude of the two components, as shown below:

$$V_T = V_{HDV}\sqrt{1+2(V_w/V_{HDV})cos\phi+(V_w/V_{HDV})^2}. \tag{1.6}$$

The relative wind yaw angle $\psi$ can then be calculated by taking the inverse tangent of the ratio of the transverse to longitudinal component. This is given by:

$$\tan\psi = \frac{(V_w/V_{HDV})\sin\phi}{1+(V_w/V_{HDV})\cos\phi}. \tag{1.7}$$

During experimental or computational runs, the drag obtained is a function of the relative wind yaw angle, D($\psi$), and is used to compute the drag coefficient:

$$C_D(\psi) = \frac{D(\psi)}{0.5\rho V^2 S}, \tag{1.8}$$

where $\rho$ is the air density, V is the total velocity, S is the wetted surface area.

While the information obtained from $C_D(\psi)$ is useful, Ortega [26] states that it does not summarize the performance of a drag reduction device into a single quantity that can be compared with that of other devices. Taking the mean of the $C_D(\psi)$ is also insufficient since it does not account for the fact that the crosswind velocities cause a vehicle traveling at a particular speed to experience certain yaw angles more than others.

A quantity that resolves both of these issues is the wind-averaged drag coefficient $C_{D_{wa}}$ . $C_{D_{wa}}$ helps to assess real world aerodynamic performance of vehicles, by weighting the vehicle's drag under different yaw conditions.

It is important to discuss the effect of yaw on the drag characteristics of HDVs because in real world conditions, an HDV will not experience incoming flow at a zero yaw angle. It is necessary to deduce the drag coefficient not only at $\psi = 0$, but also over a range of yaw angles that the vehicle will experience under typical operations. Efforts to design an aerodynamic device that reduces drag at zero yaw but increases it for other values of the relative wind yaw angle $\psi$ in the range of $-10°$ to $10°$ shall be futile. According to van Raemdonck [30], a relative wind yaw angle of $-10°$ to $10°$ represents 88% of all measured directions, obtained during an average long-haul ride through Europe. This is shown in Figure 1.15.

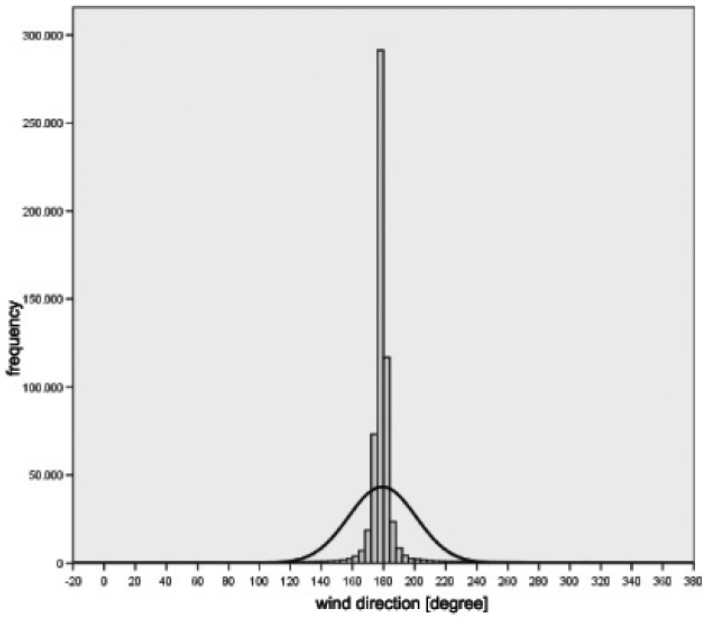


**Figure 1.15:** Wind direction histogram depicting the major range of yaw angles faced by HDVs [30]

Panda [27] attempts to calculate the average wind yaw angle $\psi$ across 145 locations in Europe at 2 $m$ height, which is considered to be half of a standard HDV's height. For every location, wind angle $\phi$ data is obtained from the European Wind Atlas [34], yaw angle $\psi$ is calculated and then an average value is obtained. The results are shown in Figure 1.16. The algorithm and procedure used can be found in Panda [27].

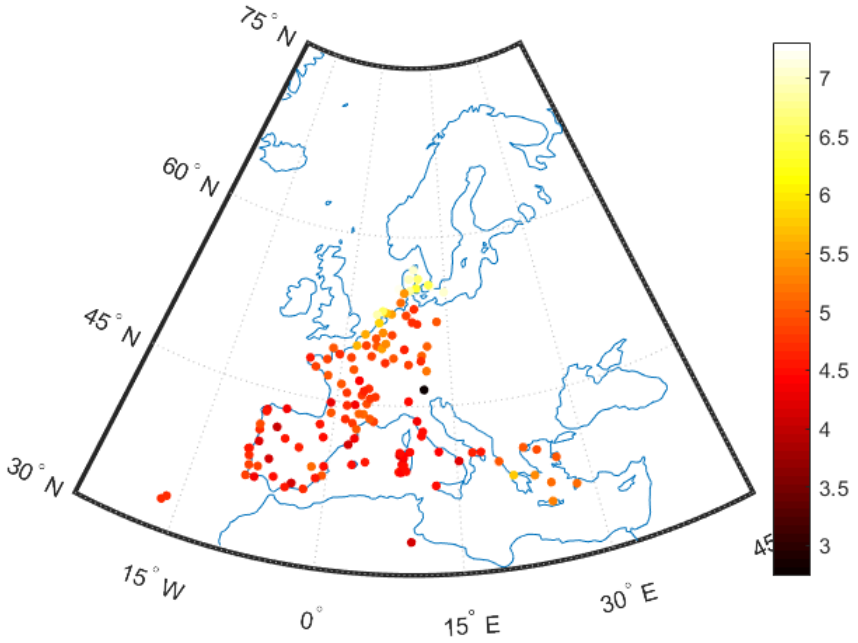


**Figure 1.16:** Average yaw angle at 145 locations across Europe [27]

One can see that for most of the locations, the absolute value of the average yaw angles lies between 4 to 5.5°. Locations which have yaw angles at the ends of the spectrum i.e. close to 3 or 7° are either near the coast

or in a mountainous region. Hence, for the non-zero yaw simulations in the M.Sc. thesis, a yaw angle of 5° is chosen.

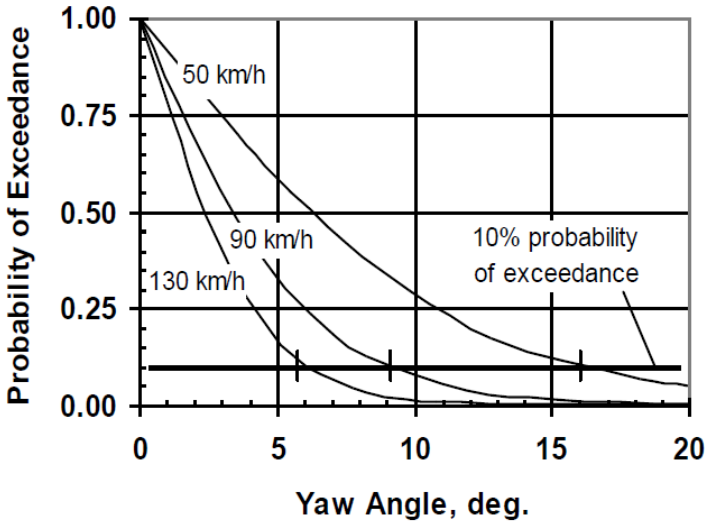


**Figure 1.17:** Probability of Occurrence of Yaw Angles Induced by a Circular 11 km/h Wind Distribution [7]

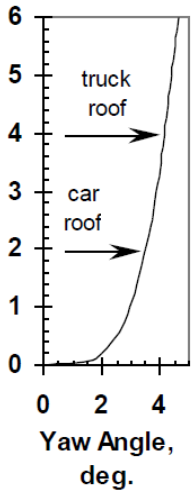


**Figure 1.18:** Variation of yaw angle with height above ground for a 11 km/h side wind at a vehicle moving 120 km/h. Y axis represents 'Height above ground in m'. [7]

The probability of exceeding a given mean hourly relative wind yaw angle $\psi$, for several ground speeds is shown in Figure 1.17. Exceeding 10° even at low ground speeds leads to a probability of at most 0.25. Highway driving velocity is usually taken to be 25 $m/s$ or 90 $km/h$. It can be observed that exceeding a yaw angle of 10° has a probability of less than 0.1 for a driving velocity of 25 $m/s$. It may be important to understand the aerodynamics of a vehicle at higher angles from the handling/safety point of view, but these angles are not necessary to study for fuel savings studies. Hence, for simulations investigating the drag faced by an HDV encountering a wind with non-zero $\psi$, an absolute yaw angle value of greater than 10° need not be considered.

Cooper [7] shows the variation of yaw angle with height above ground in Figure 1.18. This variation in the wall normal direction occurs because $V_w(z)$ varies in the wall normal direction due to the ABL profile. From (1.7), the relative wind yaw angle $\psi$ will also vary in the wall normal direction.

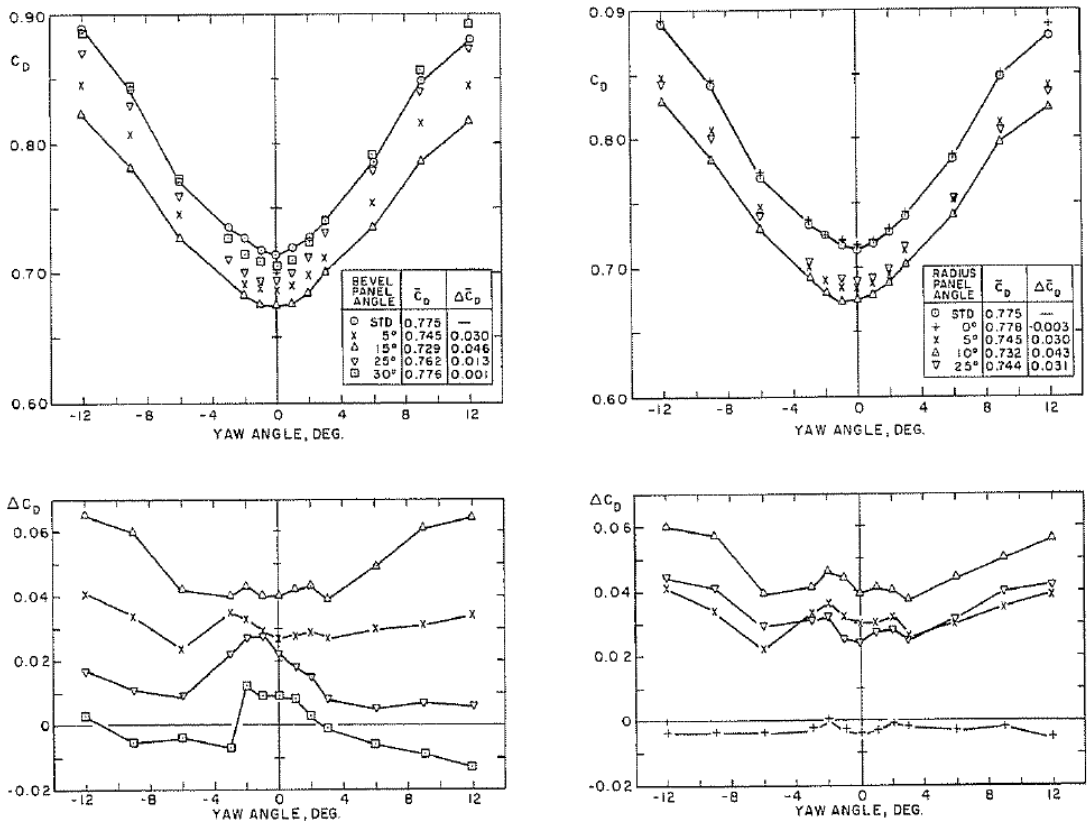


**Figure 1.19:** Drag coefficient and drag coefficient reduction with variation in yaw angle due to the effect of bevelled (Left) and curved (Right) boat-tail [8]

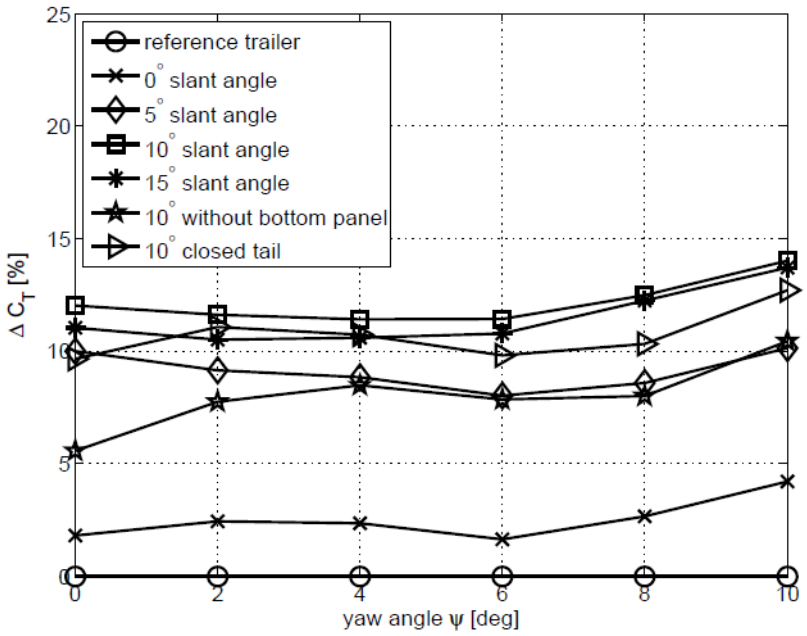


**Figure 1.20:** Drag coefficient of different tail configurations [30]

In Cooper [8], as shown in Figure 1.19, it is shown that for both the bevelled and curved boat-tail, $C_D$ increases with an increase in absolute yaw angle $\psi$. This indicates the importance of studying the effect of yaw on the efficiency of drag reduction devices.

Raemdonck [30] conducted wind tunnel studies on various boat tail configurations whose drag characteristics are shown in Figure 1.20.

Regardless of the configuration of the boattail, one can conclude from the above research that a change in the relative wind yaw angle $\psi$ to a non-zero value affects the aerodynamics across an HDV with attached aerodynamic devices, thus influencing the drag characteristics. It is thus intuitive that a non-zero relative wind yaw angle $\psi$ imparted to an ABL inflow condition shall further influence the aerodynamics across an HDV. This forms the basis of our $2^{nd}$ research goal in the M.Sc. project.

## 1.6. Research questions

The literature review aims to give an overview of our research goals which focus on studying the aerodynamics of HDVs and attached boattails. What sets apart the proposed thesis work from current literature is that it wishes to investigate the flow field when the incoming freestream represents the atmospheric boundary layer with a non-zero relative wind yaw angle. We wish to answer the following research questions:

- Which factors does the development of ABL in space depend on?
  - What are the necessary specifications such as the turbulent intensity, turbulent length scale, inlet velocity profile, that have to be provided?
- How does utilizing the ABL as inflow condition affect the HDV aerodynamics?
  - Which regions are most affected by the presence of an ABL profile with and without a wind yaw angle?
  - How is the flow different from a constant velocity profile inflow?
- How does utilizing the ABL as inflow condition influence the mechanism of the boat-tail with and without a wind yaw angle?

# 2

# Atmospheric Boundary Layer

Before running simulations for the HDV with ABL as an input, one needs to run empty domain simulations where the HDV geometry is absent. The objective is to come up with a numerical setup that ensures that the HDV experiences an ABL profile which is as close to the input profile as possible. To achieve this, minimal development (i.e. streamwise gradient) of the input profile has to occur, as it proceeds from the inlet to a few metres in front of the HDV. Various numerical settings are explored in the absence of the HDV geometry to achieve our objective such as boundary conditions, roughness effects etc.

## 2.1. ABL Modelling

While simulating the ABL in the computational domain, the upstream and downstream region of the domain are supposed to contain roughness elements such as buildings, trees etc. However, these elements are modelled instead of being explicitly represented. Their physical geometry is not included but their effect on the flow is modelled in terms of $z_O$ or by an computational equivalent sand-grain roughness $k_S$ used in wall functions. By employing $k_S$, we model the effect of these roughness elements instead of explicitly representing them.

In reality, roughness in the domain varies due to all kinds of elements, which shall always lead to a developing ABL. However, in the process of modelling the ABL, since only one parameter $z_O$ is used, the ABL profile gets 'fixed' or 'developed'. Development of the ABL in the domain shall lead to a change in $z_O$ thus deviating from the specified parameters.

Blocken [4] states three guidelines for resolving an ABL with $k_S$ - type wall functions:

1. A sufficiently high mesh resolution in the vertical direction close to the bottom of the computational domain
2. A distance $y_P$ from the centre point of the wall-adjacent cell (bottom of domain) that is larger than the sand-grain roughness height $k_S$ of the terrain i.e. :

$$y_P > k_S. \tag{2.1}$$

3. Satisfying the relationship between $k_S$ and $z_O$, as specified by Blocken [4]:

$$k_S = \frac{9.793 z_O}{C_s} \quad \text{(ANSYS Fluent)}, \tag{2.2}$$

where $C_s$ is a roughness constant in Fluent wall functions whose values ranges from 0 to 1.

For the ABL logarithmic law, aerodynamic roughness $z_0$ determines the shape of the ABL profile. To maintain this shape throughout the empty domain, one needs to match $z_0$ with the $k_S$ of the floor of the computational domain, according to (2.2).

One should note from the guidelines stated above that the 1st and 2nd point contradict each other. According to Eq. 2.2, if $z_O$ increases, $k_S$ shall increase. This will increase $y_P$, which is opposite of what Point 1 states. This contradiction is stated in Blocken [4] and will be illustrated in ABL simulation figures later on.

## 2.2. Input profile

We use the logarithmic law to represent the ABL input profile. Not only is the logarithmic law used in turbulent boundary layer profiles, the surface roughness parameter is embedded in the equation. The power law on the other hand is an empirical law.

Before using it, a slight modification is made by using a reference velocity and reference height as input. Watkins [40] states that $V_{ref} = 3m/s$ is the mean wind speed faced by an HDV at mid height ($z_{ref} = 2m$) in on-road conditions. The logarithm law then looks like:

$$V_w(z) = \frac{3}{ln(21)} ln \frac{z + z_O}{z_O}. \tag{2.3}$$

The profile shown in Figure 2.1 represents solely the wind velocity and not the HDV driving velocity which is $V_{HDV} = 23\ m/s$.

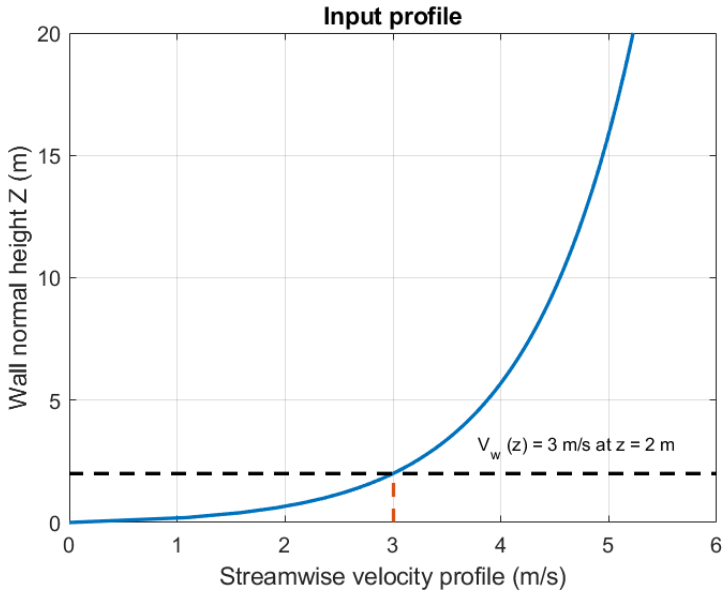


**Figure 2.1:** Input profile containing only logarithmic wind velocity profile $V_w(z)$ (without yaw)

## 2.3. Turbulence modeling

For our numerical simulations, ANSYS Fluent is used. Three different turbulence modelling methods are available in FLUENT:

1. Large Eddy Simulation (LES)
2. Detached Eddy Simulation (DES)
3. Reynolds Averaged Navier Stokes (RANS)

A steady RANS solver is used, so as to save computational time as the computational domain shall have cells in the range of $10^7$. Gheyssens [14] and Leeuwen [37] both used RANS for computational studies of the GETS model and were able to validate force coefficient data such as $C_D$, $C_L$ by comparing them to wind tunnel studies on the GETS model by van Raemdonck [30]. This indicates that RANS methodology is sufficiently accurate to meet our research objectives which focus on studying the drag trend of an HDV when faced by an ABL inflow. Also, numerous CFD solvers can perform RANS simulations whose licences are available for students and which have extensive support.

The assumption of incompressible flow is made because the driving velocity $V_{HDV}$ of our geometry is 23 $m/s$ [38], which means that the Mach number is 0.076 << 0.3. Even when acceleration occurs near the

geometry, the maximum Mach number reached is 0.12. Consequently, we solve the incompressible RANS equations which consist of the incompressible mass conservation and momentum conservation equation:

$$\nabla.\overline{V} = 0 \text{ (Mass conservation equation)}, \tag{2.4}$$

$$\frac{\partial \overline{V}}{\partial t} + \nabla.(\overline{V}\,\overline{V}) = -\frac{\nabla p}{\rho} + \frac{1}{Re}\nabla^2\overline{V} - \nabla.(\overline{V'V'}) \text{ (Momentum conservation equation)}, \tag{2.5}$$

where $\overline{V}$ is the mean velocity vector and $V'$ is the velocity fluctuation vector.

A turbulence model needs to be chosen to be able to model the term $\nabla.(\overline{V'V'})$, otherwise known as the Reynolds stress tensor. The SST $k-\omega$ model is chosen, which uses the $k-\epsilon$ model to resolve external flows and the $k-\omega$ model near the wall to resolve boundary layers. Pieterse [28] states that for ABL simulations, the SST $k-\omega$ model is best suited for predicting separation compared to $k-\epsilon$ variants. Since the wake region which consists of separated flow is the most relevant region in our simulation, the SST $k-\omega$ model was chosen. Also, the option to specify equivalent sand - grain roughness $k_S$ as input is available in the SST $k-\omega$ model but not in the 'Enhanced wall treatment' wall function in the Realizable $k-\epsilon$ model which is usually used for external aerodynamics simulations.

## 2.4. Solver settings

We use ANSYS Fluent to run our simulations and ICEM CFD to prepare the computational mesh. The settings listed below are for the initial setup which use traditional settings and whose results shall give some insight on the important steps for ABL modelling in an empty domain.

| **Boundary conditions** | |
|---|---|
| Inlet | Velocity inlet |
| Outlet | Pressure outlet |
| Top | Velocity plane |
| Bottom | No-slip stationary floor |
| Geometry surface (when geometry is present) | No-slip stationary floor |
| Left boundary | Symmetry (no yaw) and<br>Velocity inlet (non-zero yaw) |
| Right boundary | Symmetry (no yaw) and<br>Pressure outlet (non-zero yaw) |
| **Flow physics** | |
| Flow type | Steady, 3D, Incompressible |
| Flow solver | Segregated, SIMPLE |
| Turbulence modelling | RANS, SST $k-\omega$ |
| Turbulence intensity | 5 % |
| Turbulence length scale | 5 $m$ |
| Aerodynamic roughness $z_O$ | 0.1 |
| Domain size | [100 m,40 m,20 m] in x,y,z respectively |
| **Operating conditions** | |
| Density | 1.225 $kg/m^3$ |
| Driving velocity | $V_{HDV}$ = 23 $m/s$ |
| Pressure | 1 atm |
| | |

The top boundary condition is chosen as velocity plane instead of the traditional symmetry plane. This is because according to van Dijk [36], velocity plane boundary condition ensures minimal deviation from the inlet profile in the upper part of the domain. Blocken [4] also states that explicitly specifying the value of $V_w$ on the top plane further reduces any streamwise gradients in the ABL profile.

A segregated solver is chosen over a coupled solver because in an empty domain, convergence is not an issue, the flow physics is not complex and the mesh is not very fine. When we switch to HDV simulations, the coupled solver is used.

With $z_O = 0.1\ m$, $k_S = 0.9793/C_s$. We are aiming for a $y_P$ which is as low as possible to have sufficient resolution near the wall. According to (2.1), for a low $y_P$, we need a low $k_S$. $k_S$ will be lowest when $C_s$ is maximum i.e. 1. This leads to $k_S = 0.9793\ m$.

This shall mean that $y_P > 0.9793\ m$. This means that the height of the wall-adjacent cell has to be greater than 1.9586 $m$. This guideline is too restrictive for our simulation. We start by choosing $k_S = 0.9793/2\ m = 0.48965\ m$. This value of $k_S$ neither respects (2.1) nor (2.2). However, by choosing a smaller $k_S$, we have a less strict restriction on $y_P$.

## 2.5. Flow problem

### Domain

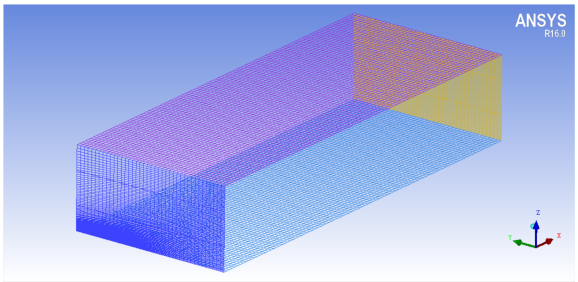


**Figure 2.2:** Empty domain for ABL simulations with no HDV with inlet(dark blue), outlet(orange), top plane (purple) and floor(light blue)

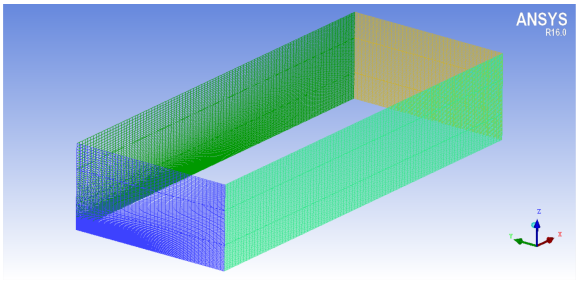


**Figure 2.3:** Empty domain for ABL simulations with no HDV with inlet, outlet, left symmetry plane (light green) and right symmetry plane (dark green)

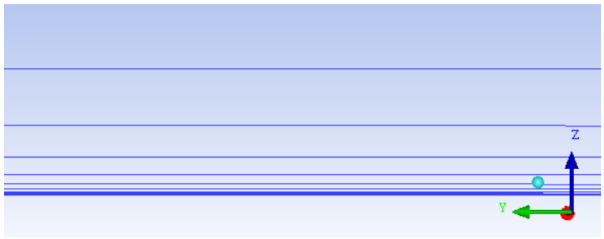


**Figure 2.4:** Near floor meshing showing the geometric spacing

Figures 2.2 and 2.3 shows the computational mesh built using ICEM CFD for the empty domain ABL simulation. The dimension of the domain in the x and y direction are of less significance because the ABL travels only in the x-direction in an empty domain. The dimension of the z-direction simply decides the height of the ABL which is to be simulated.

Data is plotted after averaging along the y-direction. Also, a geometric law is applied in the z-direction to capture the steep lower part of the ABL, as shown in Figure 2.4.

Figure 2.5 illustrates how the ABL profile deviates from the inlet profile after travelling 25 m from the inlet, when no corrections are applied. In Figure 2.6 which quantifies the deviation, one can see that without corrections, the deviation shoots up below $z = 1\ m$. However, above $z > 1\ m$, the deviation stays negligible. Figures 2.7 and 2.8 show the same phenomena observed with a zoomed view on $z < 1\ m$.

Figures 2.5 and 2.6 represent the case where the 1st cell spacing from the wall is ($2y_p = 0.1\ m$). Figures 2.9 and 2.10 compare two cases with different 1st cell spacing from wall i.e. ($2y_{p_1} = 0.1\ m$) and ($2y_{p_2} = 0.01\ m$).

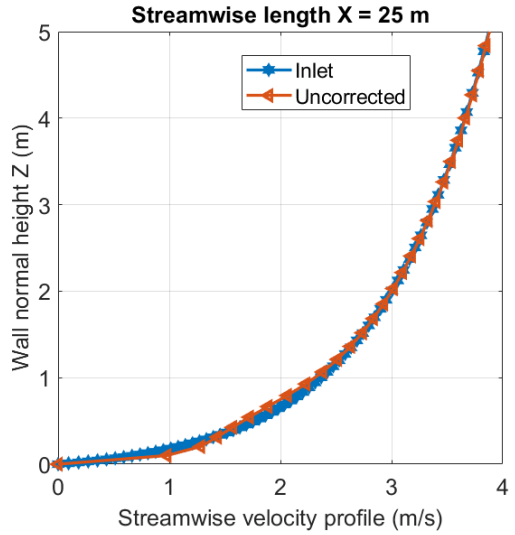


**Figure 2.5:** Development of the ABL input profile without corrections at X = 25 m

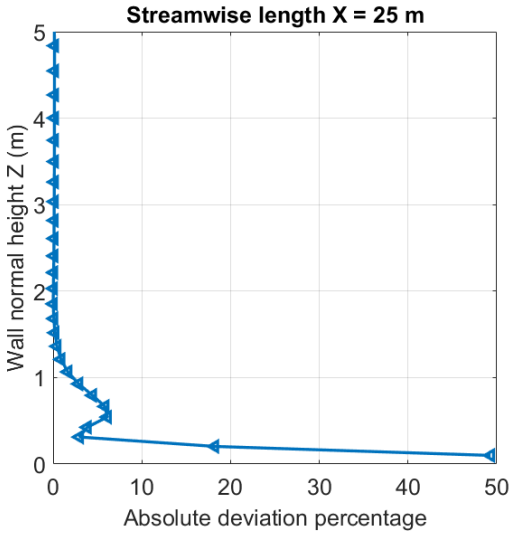


**Figure 2.6:** Absolute value of deviation (as percentage) from the input profile at X = 25 m

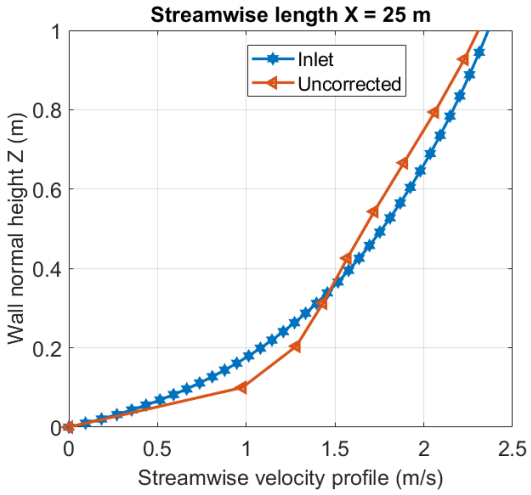


**Figure 2.7:** (first 1 m) Development of the ABL input profile without corrections at X = 25 m

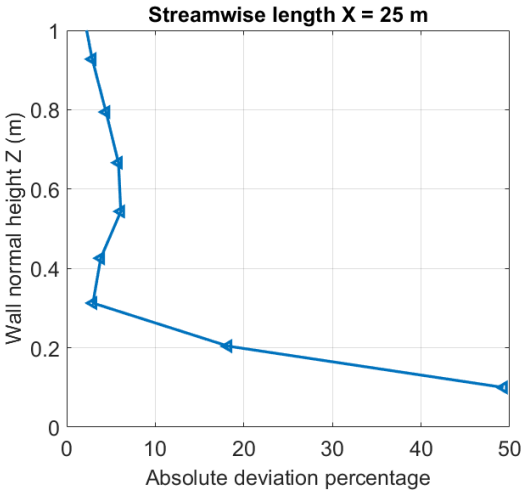


**Figure 2.8:** (first 1 m) Absolute value of deviation (as percentage) from the input profile at X = 25 m

Figures 2.9 and 2.10 illustrate the contradiction presented in the guidelines by Blocken. By refining the mesh near the wall, the ABL profile actually deviates more from the input profile, as can be seen in Figure 2.9.

Near the wall, when the finer 1st cell spacing from the wall ($2y_p = 0.01\ m$) is used, deviation percentage significantly increases below $z < 1\ m$ in Figure 2.10. This is in contradiction with the 1st guideline which requires a sufficiently high resolution near the wall.

One can see in Figure 2.9, that the traditional no slip floor boundary condition introduces significant errors near the wall (especially for $z < 1\ m$) when roughness height $k_S = 0.48965\ m$. This deviation from the input profile occurs because, due to a mismatch in the input $k_{S_{input}} = 0.48965\ m$ and the $k_S$ calculated from (2.2) i.e. $k_{S_{exact}} = 0.9793\ m$, an internal boundary layer (IBL) develops which adjusts the ABL profile to the $z_O$ calculated from $k_{S_{input}}$ according to (2.2), which is $z_{O_{new}} = 0.05\ m$. The ABL profile thus adjusts to $z_{O_{new}} = 0.05\ m$ when $k_{S_{input}} = 0.48965\ m$ is used, even though the ABL profile input uses $z_O = 0.1\ m$.

Since by choosing a $k_S$ that is not compatible with (2.2), the ABL profile deviates from the input profile, (2.2) is followed and by using $z_O = 0.1\ m$, we use $k_{S_{exact}} = 0.9793\ m$ in the subsequent calculations.

Also, since maximum deviation occurs near the floor, it is intuitive that the floor boundary condition also has an effect on the development of the ABL profile. The next section uses $k_S = 0.9793\ m$ and tests the effect

of two boundary conditions.

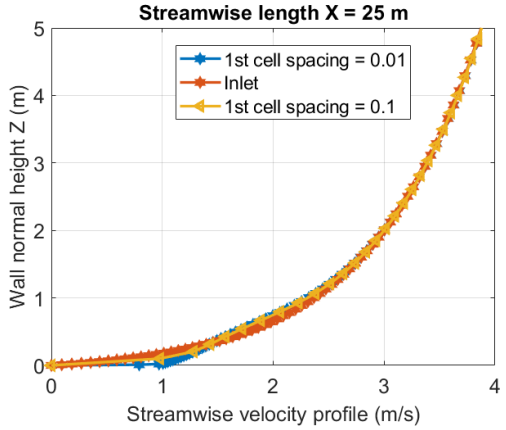


**Figure 2.9:** Development of the ABL input profile without corrections from the inlet to X = 25 m for the two cases

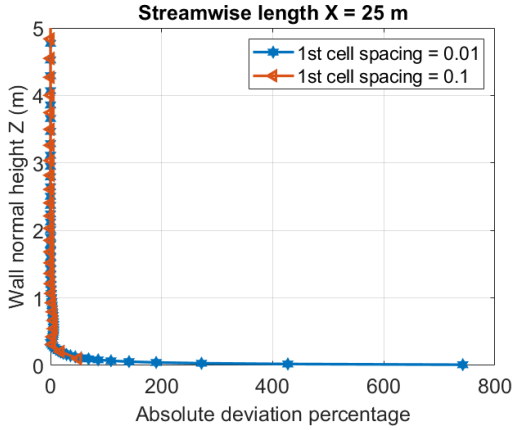


**Figure 2.10:** Absolute value of deviation (as percentage) from the input profile for the two cases at X = 25 m

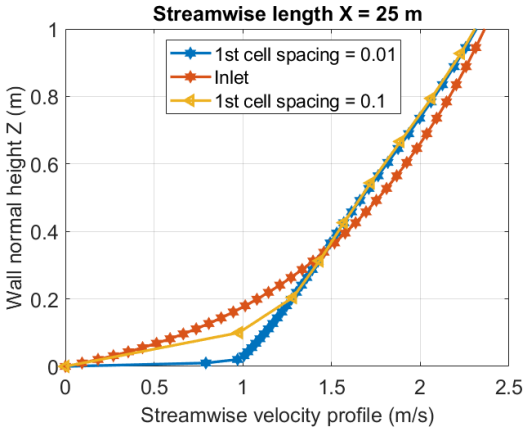


**Figure 2.11:** (first 1 m) Development of the ABL input profile without corrections from the inlet to X = 25 m for the two cases

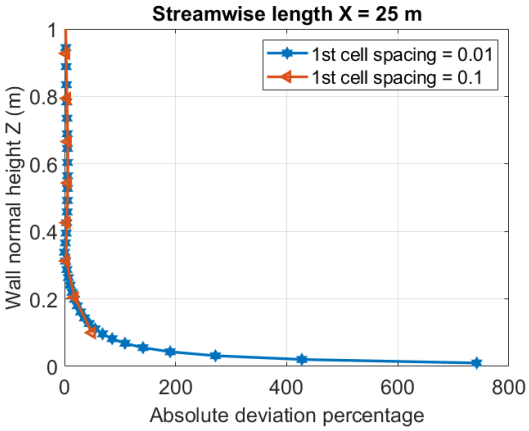


**Figure 2.12:** (first 1 m) Absolute value of deviation (as percentage) from the input profile for the two cases at X = 25 m

## 2.6. Effect of alternate floor boundary conditions

Two alternate floor boundary conditions were tested to see their effect on the development of the ABL profile:

1. Wall shear stress (WSS) BC - Blocken [4] states that one can explicitly specify the wall shear stress $\tau_w = \rho(u^*_{ABL})^2$ associated with the ABL profile at the bottom of the domain. This forces the ABL profile friction velocity $u^*_{ABL}$ to be equal to the wall function friction velocity $u^*$. This procedure can be thought of as artificially putting a wall shear stress value that shall produce the friction force necessary to sustain the ABL profile without any changes. However, according to Blocken, this BC should be used outside of the part of the domain which experiences flow disturbance due to presence of geometry because it might interfere with the actual physics of the flow around the geometry

2. No slip moving plane (VP) BC - The constant HDV driving velocity $V_{HDV} = 23\ m/s$ is added to the ABL profile. The ABL profile then begins from 23 $m/s$ at the floor instead of 0 $m/s$. The floor BC is then set to a moving plane whose velocity is equal to $V_{HDV}$. The total input profile $V_T(z)$, then consists of the driving velocity $V_{HDV}$ and the ABL wind profile $V_w(z)$. In principle, this floor boundary condition is the same as in the previous section, but with the truck velocity $V_{HDV}$ added.

For subsequent results considering zero yaw, the constant HDV driving velocity $V_{HDV} = 23\ m/s$ is simply added to the ABL wind profile $V_w(z)$, both for the WSS and VP boundary condition. Since the wind angle $\phi$ is zero here, both $V_{HDV}$ and $V_w(z)$ are in the +ve streamwise direction. The total input profile $V_T(z)$ thus can be obtained by simple scalar addition as shown in (2.6) and displayed in Figure 2.13.

$$V_w(z) + V_{HDV} = V_T(z) = 23 + \frac{3}{ln(21)} ln \frac{z + z_O}{z_O}. \tag{2.6}$$

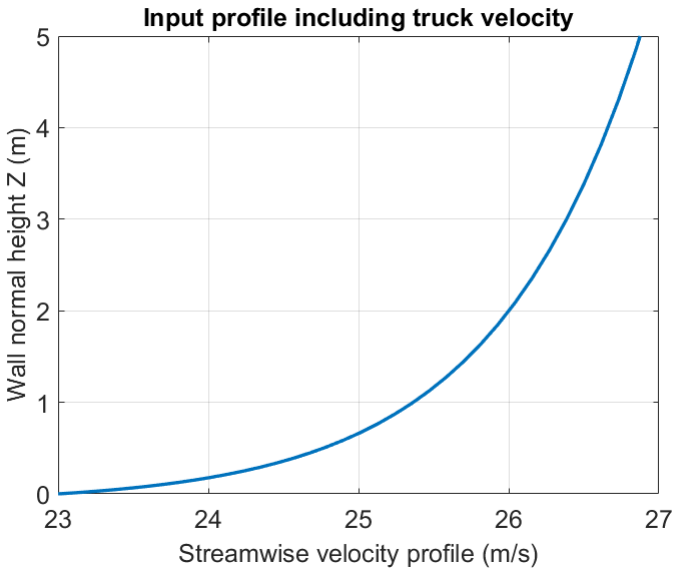


**Figure 2.13:** Input profile $V_T(z)$ containing logarithmic ABL velocity profile $V_w(z)$ and constant $V_{HDV} = 23 m/s$ (without yaw)

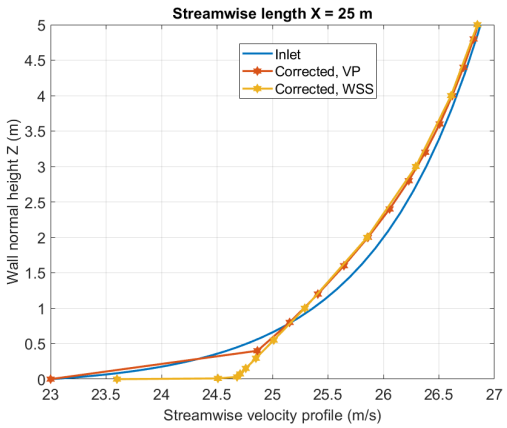


**Figure 2.14:** Development of the ABL input profile after travelling 25 m, for the two floor BCs (Corrected indicates $k_S = 0.9793\ m$)

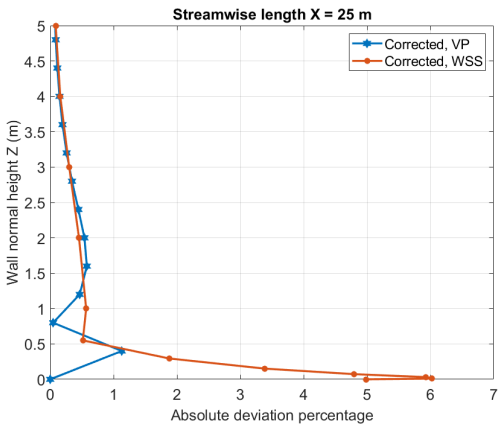


**Figure 2.15:** Absolute value of deviation (as percentage) from the input profile after travelling 25 m, for the two floor BCs (Corrected indicates $k_S = 0.9793\ m$)

Figure 2.14 shows the velocity profile at a streamwise position of $X = 25\ m$ from the inlet, with $k_S = 0.9793\ m$. For both the WSS and VP floor BC, the ABL profile undergoes acceleration near the floor (significantly more for the WSS case), even after putting $k_S = 0.9793\ m$. According to Blocken [4], the amount of development of the ABL profile depends on a number of factors such as the turbulence model used, wall functions, values of $y_P, k_S, C_s$ and top and outlet boundary condition. Hence, even after satisfying (2.2), if all the other factors are not compatible, an internal boundary layer (IBL) will develop changing the ABL profile

to a new one which is compatible with these factors. The acceleration seen in Figure 2.14 near the floor shows the development of an IBL.

From Figure 2.15, one can see that the VP floor BC results in a lower error for $z < 1\ m$, compared to the WSS BC. The maximum deviation percentage encountered goes up to just 1 %. This amount of deviation from the input profile can be considered as allowable. However, the WSS BC increases the maximum deviation percentage to 6%, higher than that of the VP floor BC.

It seems intuitive to thus go ahead with the VP floor BC. However before choosing the VP floor BC for our HDV simulations, to be sure that (2.2) helps in minimizing ABL development, a study on effect of $k_S$ was conducted and the results are plotted in Figures 2.16 and 2.17.

## 2.7. Effect of sand-grain roughness $k_S$

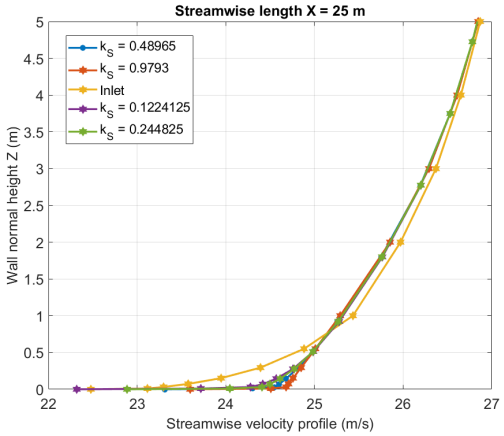


**Figure 2.16:** Development of the ABL input profile in the streamwise direction after travelling 25 m for various $k_S$ (with WSS floor BC)

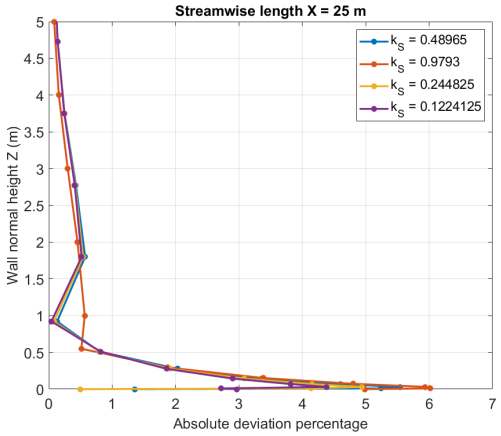


**Figure 2.17:** Absolute value of deviation (as percentage) from the input profile after travelling 25 m, for various $k_S$ (with WSS floor BC)

Figures 2.16 and 2.17 show how the ABL profile develops after travelling 25 m, for various $k_S$ by employing the WSS floor BC. While Figure 2.16 denotes significant acceleration near the floor for all values of $k_S$, Figure 2.17 shows that the maximum deviation percentage does not go below 4 %. It stands to reason that even after satisfying (2.2), considerable development still occurs for the WSS floor BC case. This is due to the contribution from other factors specified by Blocken such as incompatibility in turbulence model, wall functions, values of $y_P, k_S, C_s$ etc.

Also, due to an artificially imposed wall shear stress on the floor, the inlet ABL profile no longer has a value of 23 $m/s$ at $z = 0$ in Figure 2.16. It goes below 23 $m/s$. Since the wall shear stress value is explicitly imposed on the floor, the no-slip condition is omitted. This leads to slip on the floor which includes the $z = 0$ point at the inlet. Thus, the velocity changes at the $z = 0$ point of the inlet too.

The acceleration caused due to IBL formation near the floor is apparent in Figure 2.18 also, for all values of $k_S$ except $k_S = 0.9793\ m$. This is because on satisfying 2.2, we choose a $k_S$ which is compatible with the input ABL profile. Hence, no IBL is formed.

The same is observed in Figure 2.19 where the maximum deviation percentage for $k_S = 0.9793\ m$ goes down to approximately just 1%, while it is higher for all other values of $k_S$. Hence, with the VP floor BC, (2.2) is obeyed and all settings used are compatible with $z_O = 0.1\ m$ due to which development is minimized. One should note that minimal development still exists and thus in simulations involving the geometry, the upstream distance needs to be minimised to ensure that ABL development stays minimal.

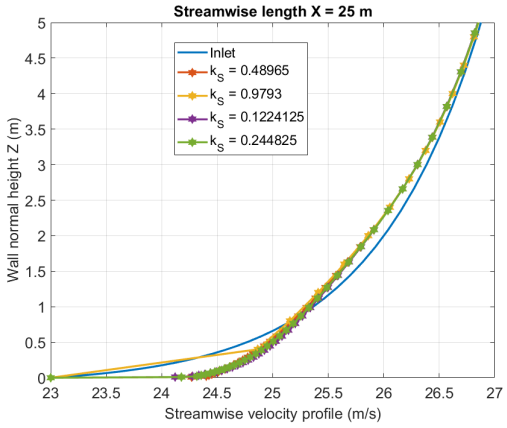


**Figure 2.18:** Development of the ABL input profile in the streamwise direction after travelling 25 m for various $k_S$ (with VP floor BC)

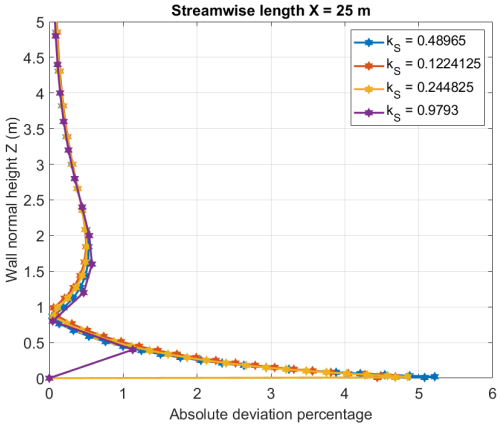


**Figure 2.19:** Absolute value of deviation (as percentage) from the input profile after travelling 25 m, for various $k_S$ (with VP floor BC)

Also, unlike the WSS floor BC, the inlet profile stays intact at the $z = 0$ point. Thus, the VP floor BC is used for simulations where an HDV is present in the domain. It should be noted that the floor moving plane has a velocity always in the streamwise direction as it represents the driving velocity $V_{HDV}$.

To summarise, the following BCs are used finally for the HDV simulations:

| **Boundary conditions** | |
|---|---|
| Inlet | Velocity inlet - $V_T(z)$ consisting of both the ABL wind profile $V_w(z)$ and driving velocity $V_{HDV}$ |
| Geometry surface (when geometry is present) | No-slip stationary surface |
| Outlet | Pressure outlet |
| Top | Velocity plane |
| Left boundary | Symmetry (no yaw) and<br>Velocity inlet (non-zero yaw) |
| Right boundary | Symmetry (no yaw) and<br>Pressure outlet (non-zero yaw) |
| Floor | No-slip moving plane with $V_{HDV} = 23\ m/s$ |
| Sand-grain roughness $k_S$ | 0.9793 m |

**Table 2.1:** Boundary conditions to be used for HDV simulations

# 3

# HDV Aerodynamics - Effect of the ABL inflow

This chapters deals with the numerical setup of the simulation of flow across an HDV with ABL as an inflow by using ANSYS Fluent, followed by an analysis of the results obtained, for the zero yaw case. The domain and mesh setup are shown in sections 3.3 and 3.4. Strategies to resolve the boundary layer are shown in section 3.5 and solver settings are presented in section 3.6. Validation procedures and solution results are specified in sections 3.7 and 3.8. Drag force trends are shown and explained in section 3.8.1. Finally, our findings are explained in section 3.9.

## 3.1. Geometry

HDVs have a complex geometry consisting of parts such as the tractor-trailer gap, underbody geometry, wheels etc. Meshing such a realistic geometry shall require immense computational time and effort which is outside the scope of this project. Since our project focuses on fundamental concepts such as effect of yaw and ABL, it is not necessary to use a realistic HDV geometry for our calculations . We instead choose the GETS (Generic European Transport System) model [30]. As can be observed in Figure 3.1, the geometry has none of the complex features which a realistic HDV has apart from the front surface curvature. The purpose of using the GETS model is to focus on the key phenomena such as base drag and wake formation and how factors such as ABL and non-zero yaw affect them. Figures 3.2 and 3.3 label the various parts of the GETS model. Table 3.1 shows the dimensions of the GETS model used and Figure 3.4 illustrates the dimensions of the GETS model in the computational domain.

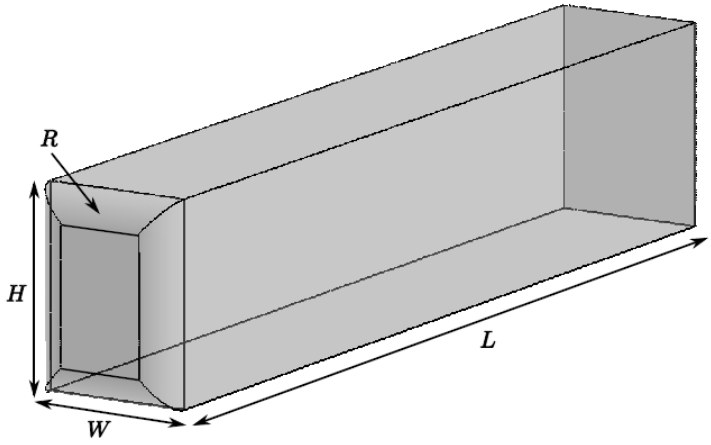


**Figure 3.1:** GETS Model

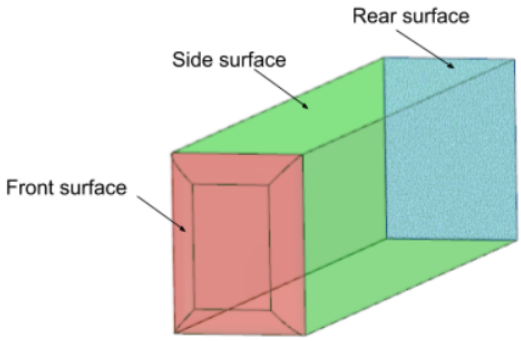


**Figure 3.2:** Isometric view of the GETS model showing its front, side and rear surfaces

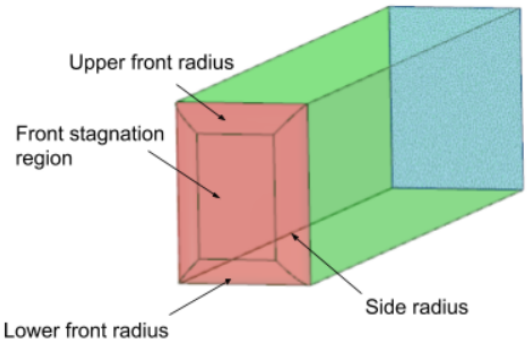


**Figure 3.3:** Isometric view of the GETS model showing parts of the front surface

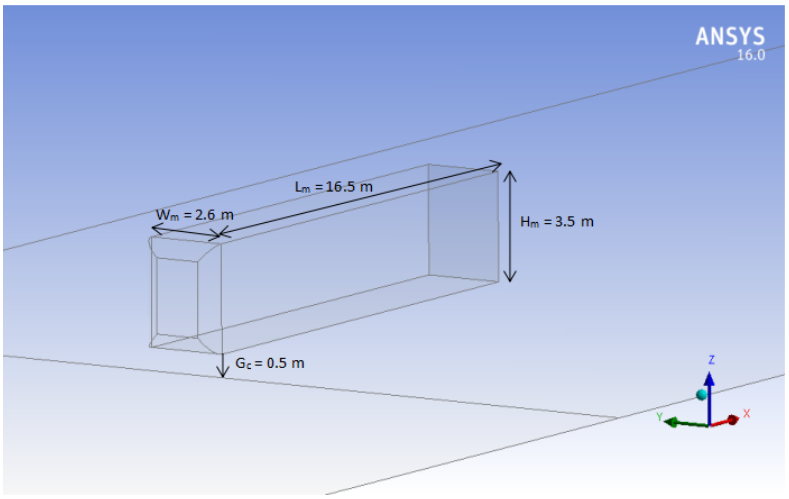


**Figure 3.4:** Isometric view of the GETS model showing its dimensions and its distance from the ground

| **HDV** | |
|---|---|
| **Dimension** | **Value** |
| Height $H_m$ | 3.5 $m$ |
| Length $L_m$ | 16.5 $m$ |
| Width $W_m$ | 2.6 $m$ |
| Ground clearance $G_c$ | 0.5 $m$ |
| Radius $R$ | 0.54 $m$ |

**Table 3.1:** Dimensions of the GETS model

## 3.2. Reynolds number

In [30], the dependency of the drag coefficient $C_D$ on the Reynolds number based on the model width was studied by conducting a Reynolds number sweep from 0.8 to 1.5 million. In this range, no Reynolds dependency was detected for the drag coefficient.

Based on the model width, for our case $Re > 1.9M$. Hence, we can conclude that there is no dependency on the Reynolds number for the $C_D$.

## 3.3. Domain setup

According to guidelines stated by SAE [2], the sizing of the computational domain is chosen as shown in Table 3.2:

| **Outer domain** | |
|---|---|
| **Dimension** | **Value** |
| Height $H_d$ | $6H_m = 21$ $m$ |
| Length $L_d$ | $9L_m = 148.5$ $m$ ($3L_m$ in front of geometry and $5L_m$ at the back) |
| Width $W_d$ | $5W_m = 13$ $m$ on both sides |

**Table 3.2:** Dimensions of the computational domain

$$\text{Blockage ratio:} \frac{A_{model}}{A_{domain}} = \frac{1}{9}.\frac{1}{10} = 1.11\%. \tag{3.1}$$

| **Outer refinement box** | |
|---|---|
| **Dimension** | **Value** |
| Height | $0.5L_m$ |
| Length | $0.5L_m$ in front of geometry, $L_m$ at the back |
| Width | $0.5L_m$ |
| **Inner refinement box** | |
| **Dimension** | **Value** |
| Height | $1.31H_m$ |
| Length | $0.1L_m$ in front of geometry, $0.5L_m$ at the back |
| Width | $1.2W_m$ |

**Table 3.3:** Dimensions of the refinement boxes used

Since the entire domain is symmetrical in the $Y = 0$ i.e. centre spanwise plane, only half the domain is considered for the zero yaw case.

Using the dimensions mentioned above, the blockage ratio comes out to be 1.11%, which is sufficiently small according to Lanfrit [18].

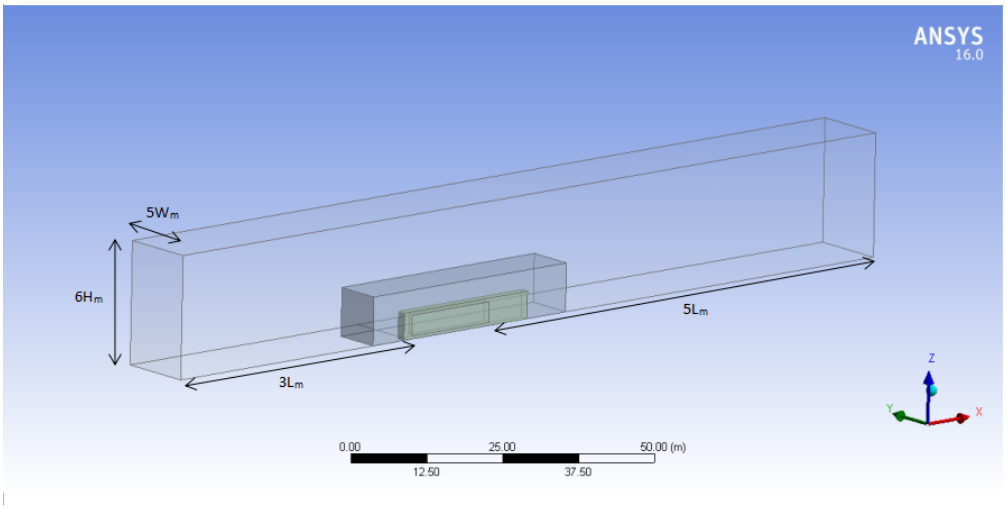


**Figure 3.5:** Isometric view of the computational domain showing dimensions of the outer domain

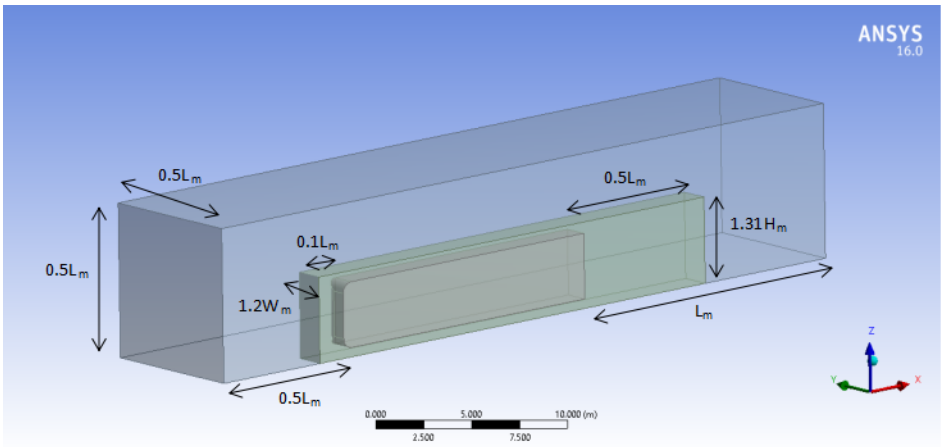


**Figure 3.6:** Isometric view of the computational domain showing dimensions of the refinement boxes

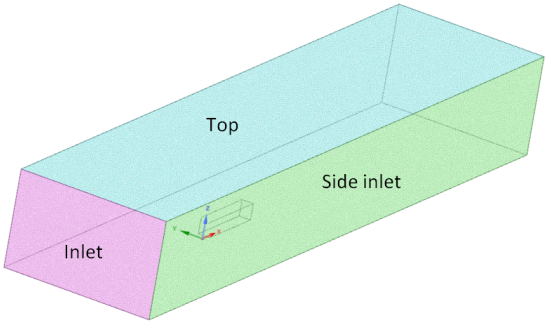


**Figure 3.7:** Isometric view of the computational domain showing the boundary conditions

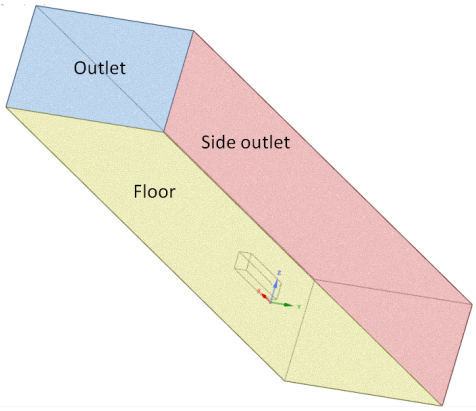


**Figure 3.8:** Isometric view of the computational domain showing showing the boundary conditions

Refinement boxes are introduced in the domain to capture flow phenomena more accurately as we ap-

proach the HDV. This way, we save the computational size of the mesh and also solve the flow more accurately. Two refinement boxes are used, similar to those used in Kruijssen [17]. Their dimensions are shown in Table 3.3. The inner refinement box is mainly used to capture the backflow region in the wake while the outer refinement box is used to capture the environment around the GETS model and particularly a major part of the wake. This is why the inner refinement box is finer than the outer one. Figures 3.5 and 3.6 illustrate the dimensions of the inner and outer refinement boxes used in the computational domain.

## 3.4. Mesh setup

The results of every computational simulation depend on the number of cells used in the mesh. Discretisation error keeps decreasing as one moves from a coarser to a finer mesh, till a point comes where the decrease in the discretisation error is negligible. Until that point, the results have a dependency on the mesh sizing used. To determine this dependency and thus choose the right mesh sizing, a mesh sensitivity study is performed as shown in Figure 3.13 by using various mesh sizings listed in Table 3.4. The mesh gets refined with every subsequent setting. The various mesh sizes listed below are specified for only half the domain due to the GETS model being symmetric about the XZ plane when experiencing wind with zero yaw angle $\psi$.

| | **Outer domain cell size (m)** | **Outer refinement box cell size (m)** | **Inner refinement box cell size (m)** | **Number of cells (in millions)** |
|---|---|---|---|---|
| **Mesh 1** | 1.6 | 0.4 | 0.1 | 1.97 |
| **Mesh 2** | 1.28 | 0.32 | 0.08 | 3.52 |
| **Mesh 3** | 1.12 | 0.28 | 0.07 | 4.95 |
| **Mesh 4** | 1 | 0.25 | 0.0625 | 6.71 |
| **Mesh 5** | 0.88 | 0.22 | 0.055 | 9.41 |
| **Mesh 6** | 0.8 | 0.2 | 0.05 | 12.12 |
| **Mesh 7** | 0.72 | 0.18 | 0.045 | 16.14 |

**Table 3.4:** Various meshes used for mesh sensitivity study

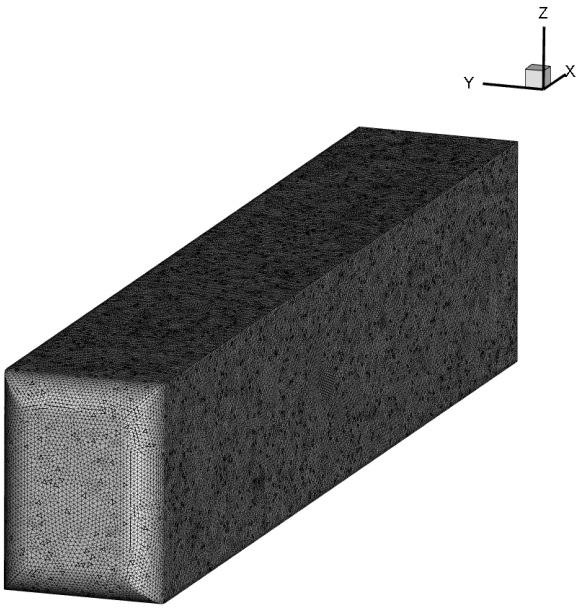


**Figure 3.9:** Isometric view of the surface mesh

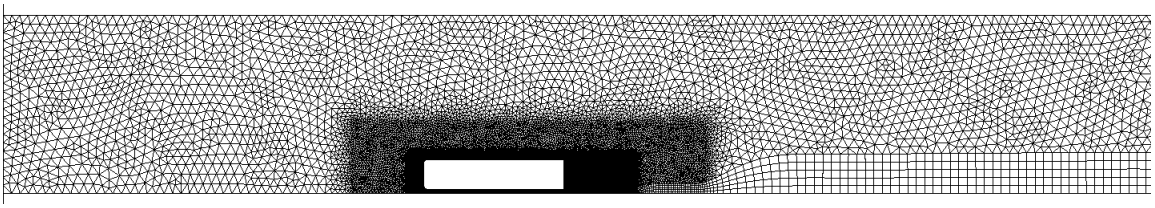

**Figure 3.10:** Computational mesh showing the outer domain and the refinement boxes

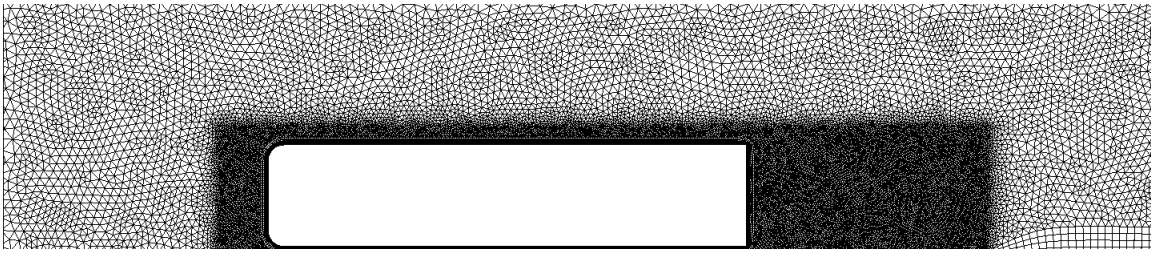

**Figure 3.11:** Computational mesh showing the refinement boxes

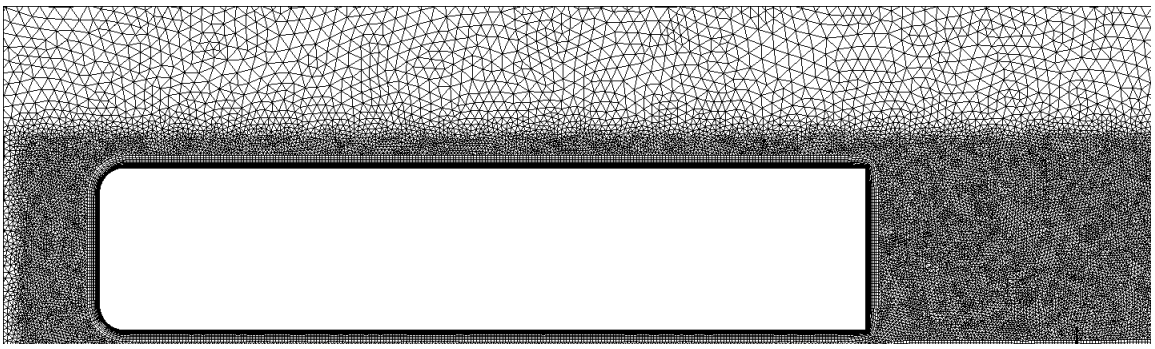

**Figure 3.12:** Computational mesh showing the refinement boxes and the prism layers on the geometry and the floor

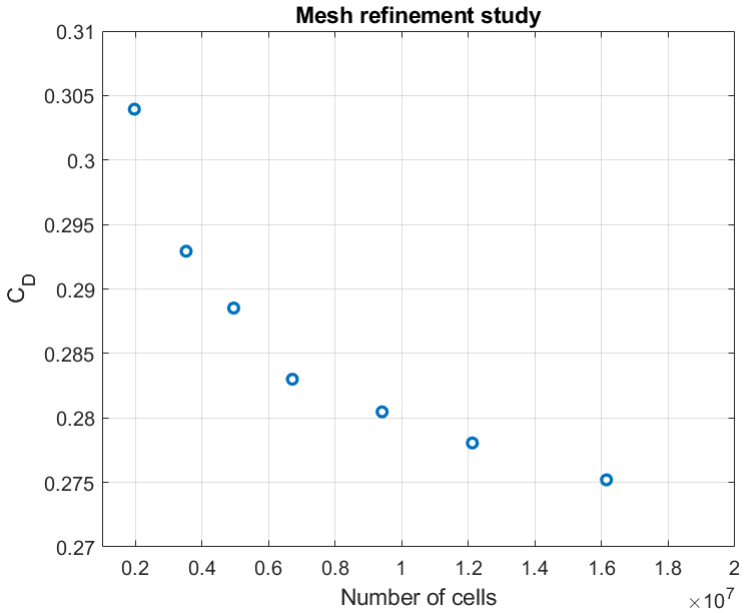


**Figure 3.13:** Mesh sensitivity study

The mesh size is increased by refining the outer domain and both the refinement boxes in such a way

that both the ratio of outer domain size to outer refinement box size and the ratio of outer refinement box to inner refinement box size are kept equal to 0.25. This is to ensure that the volume change of the cells is gradual, thus leading to good mesh quality. The surface mesh sizing uses the same values as that of the inner refinement box. This is to ensure smooth transition from the volume mesh to surface mesh and thus achieve good skewness and aspect ratio values.

Figure 3.13 uses validation settings specified in Section 3.7. It can be observed in Figure 3.13 that the drag coefficient decreases asymptotically with an increase in mesh size. Even though ideally, one should go for the finest mesh to obtain mesh-independent values, to save computational effort, a mesh size of 6.7 million cells is chosen. This is because the non-zero yaw cases will not have symmetry about the XZ plane and thus the full domain will have to be considered. Also, the size of the inner refinement box will be increased due to the lateral wind component inducing a side force on the vehicle. This will drastically increase the amount of cells.

## 3.5. Boundary layer

Whenever a fluid flows on an object, due to surface friction, a boundary layer is generated on the surface. A boundary layer consists of an inner layer and an outer layer. Both layers partially overlap. The inner layer outside of the overlap region consists of the viscous sub layer and the buffer layer while the overlap region consists of the log-law layer. These layers are illustrated in Figure 3.14

As one can see in Figure 3.14, these layers can be described by using a non-dimensional wall-normal coordinate called $y^+$ . The value of $y^+$ chosen decides how well the boundary layer is resolved.

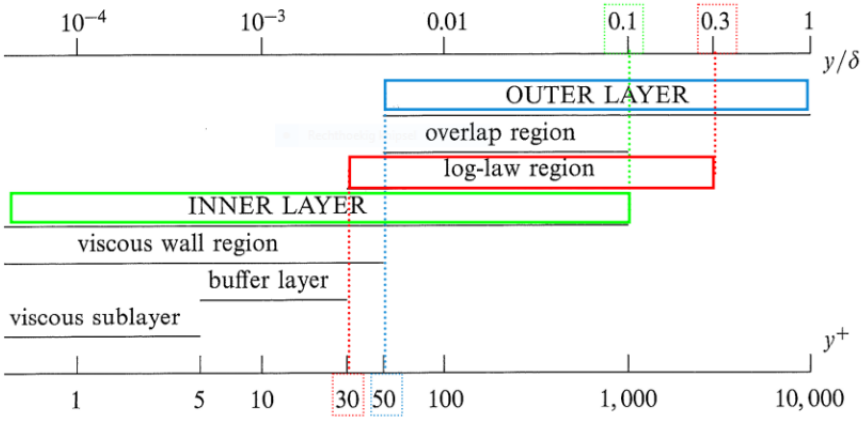


**Figure 3.14:** Various regions of a turbulent boundary layer for different $y^+$ [29]

The boundary layer on an object is modelled using prism layers [18]. Calculations are done between nodes or elements and prism layers gives you more elements perpendicular to the surface. This is an efficient way to achieve better resolution of the boundary layer, without increasing the number of elements along the surface. This gives a more accurate solution than can be achieved with a fine tetra mesh.

The first prism layer thickness, y, is dependent on the value of $y^+$ used, as shown in Pope [29].

$$y = y^+ \frac{\nu}{u_\tau} \quad [29], \tag{3.2}$$

where, $u_\tau$ is the friction velocity and $\nu$ is the kinematic viscosity. $u_\tau$ is defined in Pope [29] as:

$$u_\tau = \sqrt{\frac{\tau}{\rho}} \quad [29]. \tag{3.3}$$

The skin friction coefficient $C_f$ is a dimensionless number which characterises the frictional force experienced by the fluid at the flow boundary [41]. The wall shear stress, $\tau$ is related to the skin friction coefficient $C_f$, as defined in:

$$\tau = \frac{1}{2}\rho C_f V^2 \quad [29]. \tag{3.4}$$

By specifying the value of $y^+$ and using (3.2), (3.3), (3.4), one can calculate the first layer thickness. The only unknown left is $C_f$ which can be calculated by assuming that the boundary layer over the HDV is similar to that of a turbulent boundary layer over a flat plate. Therefore, we can define $C_f$ as:

$$C_f = \frac{0.027}{Re_x^{1/7}} \quad [41]. \tag{3.5}$$

After calculating the first prism layer's thickness, the amount of prism layers needed to model the entire boundary layer must be defined. The amount of prism layers is dependent on the growth factor, which is the ratio of the thickness of two consecutive prism layers and the maximum boundary layer thickness. Once again, we assume a flat plate turbulent boundary layer and according to the assumption, the boundary layer thickness at a streamwise position $x$ can be computed using:

$$\delta = \frac{0.16}{Re_x^{1/7}} \quad [41]. \tag{3.6}$$

By using (3.6), the maximum boundary layer thickness comes out to be 0.231 m. According to Pope [29], to fully solve the boundary layer, a value of $y^+ < 1$ is needed. However, this will not only create a very small first prism layer thickness but also with $\delta = 0.231m$, this leads to too many layers. This will significantly increase the computational cost for the calculations.

To work around this issue, Lanfrit [18] suggests using wall functions which model the boundary layer using empirical formulae. The boundary layer part which is modelled with the empirical formulae and the parts which are solved by the RANS equations is dependent on the value of $y^+$. For an HDV, according to Lanfrit [18] and SAE [2] , $y^+$ should be between 30 and 300 to use wall-functions.

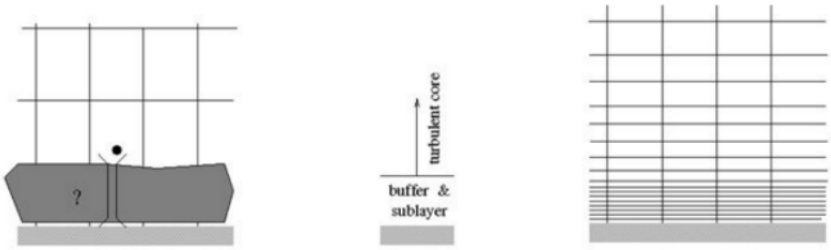


**Figure 3.15:** Left: When wall functions are applied close to the wall (Region below the black dot represents the region where wall functions are applied), Right: When near-wall modelling is used

In Figure 3.15, the difference between the wall functions and the near wall modelling is shown. When using near-wall modelling, $y^+ < 1$ and the RANS equations are solved all the way to the wall. When using wall functions, the RANS equations are only solved until the point where the prism layers start and from there on, the wall functions are used [13]. However, since the $y^+$ value is based on the skin friction coefficient, this value will not always remain between 30 and 300. On surfaces which face stagnation, the $y^+$ value may go below 30. In these regions, one should not use wall functions. To solve this, we use Fluent's Enhanced Wall Treatment that uses wall functions if the $y^+$ is within the valid range and uses the near wall treatment when $y^+$ is small enough [13]. This procedure is present in the SST $k-\omega$ model by default.

The entire HDV is surrounded by 14 prism layers where the first layer thickness is 0.0045 m and which grow with a growth rate of 1.2. On the floor, starting from the position of the HDV, 5 prism layers extend from the surface and continue till the rear outlet. These prism layers depend on an aspect ratio of 0.8 instead of a first layer thickness. This allows them to have variable thickness as the mesh cells above them increase in size. Prism layers can capture the development of internal boundary layers which can occur when flow is redirected by a geometry to the ground and therefore interacts with the ground

## 3.6. Solver settings

All physical variable are discretised with a first order scheme and solved using the SIMPLE algorithm for the first 150 iterations. After 150 iterations, the pressure is discretised with a second order scheme and the other variables use a second order upwind scheme for the spatial discretisation. Also, the coupled solver is used after 150 iterations to accelerate convergence. Gradients are modelled using Green-Gauss node based approach. The required limits for the convergence residuals is $1e-6$.

## 3.7. Validation

Before running ABL simulations, we validate our mesh and solver settings by running HDV simulations with a constant flow at the inlet, instead of an ABL inflow and comparing the results to wind tunnel studies by van Raemdonck [30] on the GETS model.

The settings used are the same as specified in Table 2.1, except that the top boundary condition is a symmetry plane and the driving velocity is $V_{HDV} = 25\ m/s$. The turbulent length scale is chosen as 1.3 m.

We first compare the drag coefficient $C_D$, lift coefficient $C_L$ and the mean base pressure coefficient $C_{pmb}$. $C_{pmb}$ is calculated by averaging all the pressure coefficients over the rear surface of the HDV.

| | $\psi = 0°$ | | | $\psi = 3°$ | |
|---|---|---|---|---|---|
| | $C_D$ | $C_L$ | $C_{pmb}$ | $C_D$ | $C_S$ |
| **CFD** | 0.283 | -0.032 | -0.203 | 0.289 | 0.293 |
| **Wind tunnel** | 0.297 | -0.036 | -0.163 | 0.300 | 0.305 |

**Table 3.5:** Comparison of the various force coefficients between CFD and wind tunnel studies [30]

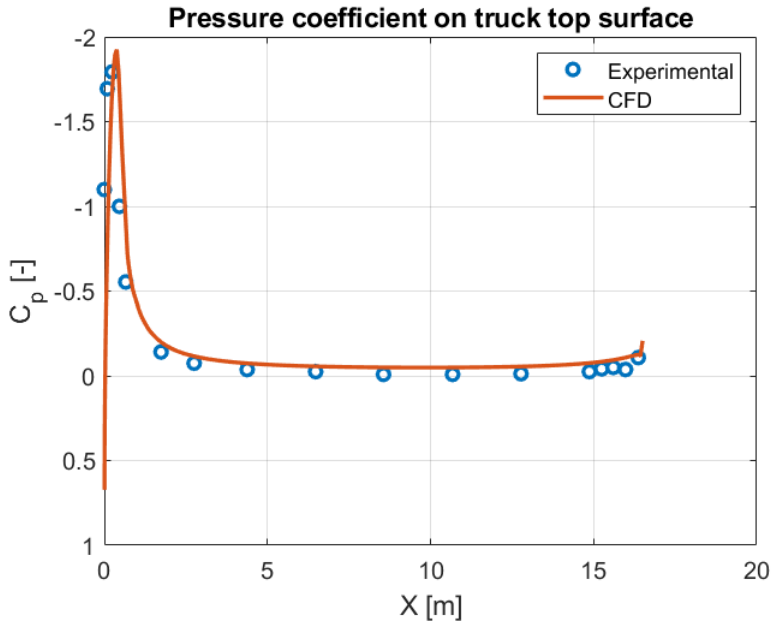


**Figure 3.16:** Pressure coefficient variation over the HDV's top surface obtained from the centerline along the streamwise direction (X = 0 $m$ represents the front surface and X = 16.5 $m$ represents the rear surface of the truck

While $C_L$ data agrees well with the wind tunnel studies, $C_D$ is a little lower and $C_{pmb}$ data doesn't agree. A major reason why $C_D$ does not match is because according to Raemdonck, the wind tunnel model was mounted on struts which led to an extra drag component. These struts are not modelled in our geometry due

to which a lower drag is observed in our numerical results. This is the same reason why $C_S$ values are higher for the wind tunnel studies for the non-zero yaw case.

$C_{pmb}$ values don't match primarily because the rear surface pressure is affected by the wake region which is inherently unsteady and is captured much better in wind tunnel studies compared to our steady state solver. Gheyssens [14] compares the pressure coefficient on the rear surface obtained from CFD data with wind tunnel data by van Raemdonck [30]. A stark difference is observed. This difference is also reflected in the x velocity contours in the wake region. Both the location and the size of the wake vortices don't agree with the wind tunnel PIV data. This inability to accurately capture rear pressure behaviour and wake structures can be attributed to the steady nature of the RANS solver.

Figure 3.16 shows the pressure coefficient trend over the HDV's top surface. The data is obtained by extracting pressure values from the centerline along the streamwise direction. Even though a very minute offset between CFD and experimental data is observed and the pressure peak is under predicted by the CFD calculations, the CFD data still matches well with the experimental values.

## 3.8. Results

This sections presents the various findings for the simulation of an HDV facing an ABL inflow. An equivalent 'No-ABL' case is setup which faces a constant velocity inflow and is used to compare the results with the ABL inflow case. Contours presenting the difference between the ABL and 'No-ABL' case shall also be presented hereforth. They shall represent $C$(ABL) - $C$('No-ABL') where $C$ represents any physical variable such as pressure, x-velocity etc. The black line in the contours marks the $z = z_{eq}$ line. The maximum and minimum values of the contours are adjusted both for easier comparison between figures and to represent flow phenomena more clearly.

### $Y^+$

We check whether we truly obtained the desired $y^+$ range for the use of wall functions i.e. $30-300$. Figure 3.17 shows that $y^+$ values range between 13 to 300. $y^+$ values less than 30 are observed in the stagnation region, where near wall modelling will be applied because of enhanced wall treatment inbuilt in the $k-\omega$ model. Apart from these regions, the HDV model overall lies in the desirable $y^+$ range. Hence, wall functions can be applied.

On the lower corners of the HDV model in Figure 3.17, dark blue dots are observed which are not present in the upper corners. It is tough to ascertain the cause behind this phenomenon. It may be attributed to the high sand-grain roughness $k_S = 0.9793\ m$, which is higher than the ground clearance $G_c = 0.5\ m$.

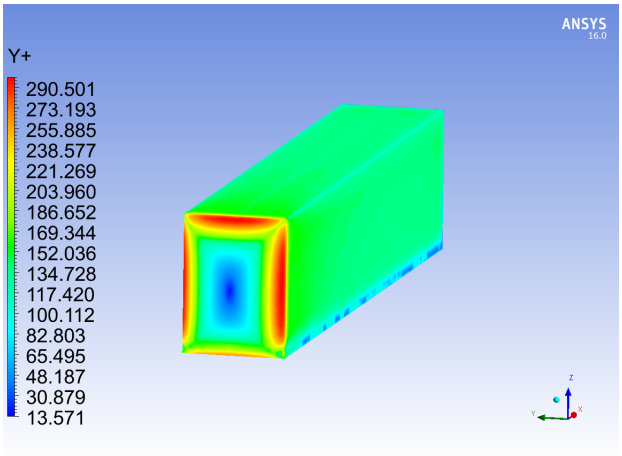


**Figure 3.17:** Y + values on the GETS model

Before analysing results from our ABL simulations, to be able to compare these results to traditional constant velocity inflow, we calculate an 'equivalent' constant velocity profile. This is done by equating the total mass flow over the HDV height for both the traditional and ABL cases.

$$\int_0^{H_m} \rho V_w(z)\,dz = \rho V_{w,eq} H_m. \tag{3.7}$$

$$V_{w,eq} = \frac{1}{H_m}\int_0^{H_m} \frac{3}{ln(21)} ln\frac{z+z_O}{z_O}\,dz. \tag{3.8}$$

$$V_{w,eq} = 2.6\ m/s. \tag{3.9}$$

$$V_{T,eq} = V_{HDV} + V_{w,eq} = 23 + 2.6\ m/s = 25.6\ m/s. \tag{3.10}$$

The traditional inflow case is thus given a constant inlet velocity of $V_{T,eq} = 25.6\ m/s$. The top plane and floor also move at $V_{T,eq} = 25.6\ m/s$ in the streamwise direction. $V_{T,eq} = 25.6\ m/s$ is used as the reference velocity for the $\psi = 0°$ case.

Aside from the inlet, top plane and the floor, the settings for the traditional and ABL cases are exactly the same. For the results hereforth, the traditional case shall be referred to as 'No-ABL'.

We input $V_{w,eq}$ in the logarithmic law (2.3) and calculate $z_{eq}$. This shall help us to find out at what height the ABL experiences $V_{w,eq}$. Below $z_{eq}$, the ABL shall have velocities lower than $V_{w,eq}$, and above $z_{eq}$, velocities will be higher than $V_{w,eq}$. This trend shall help us to compare the ABL case with the 'No-ABL' case. The value of $z_{eq}$ comes out to be 1.37 $m$. The input velocity profiles for the ABL and 'No-ABL' cases are depicted in Figure 3.18.

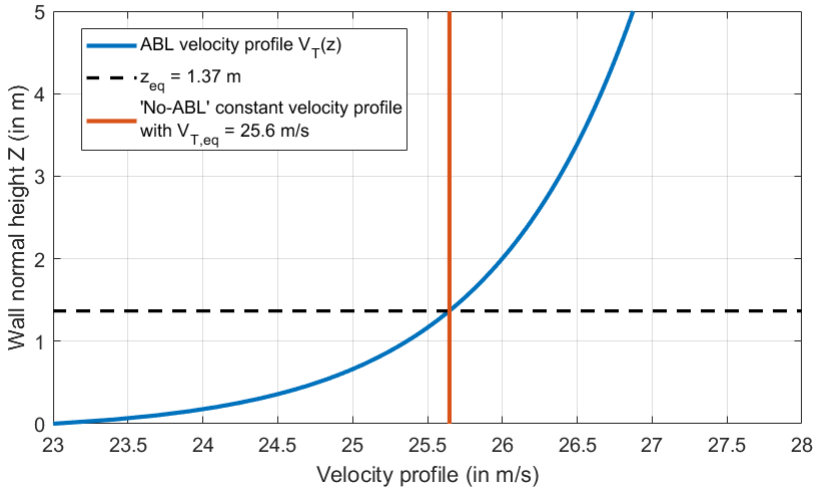


**Figure 3.18:** Input velocity profiles for the inlets of the two cases: ABL and 'No-ABL'

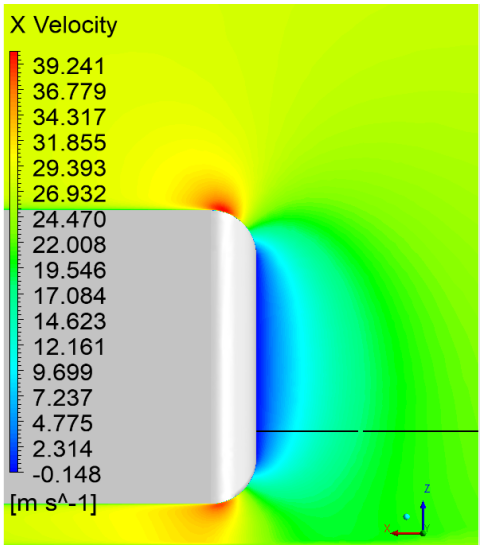


**Figure 3.19:** X Velocity contours (for the ABL case) near the HDV's front surface (y = 0 plane i.e. side view) (Black line marks the $z = z_{eq}$ line)

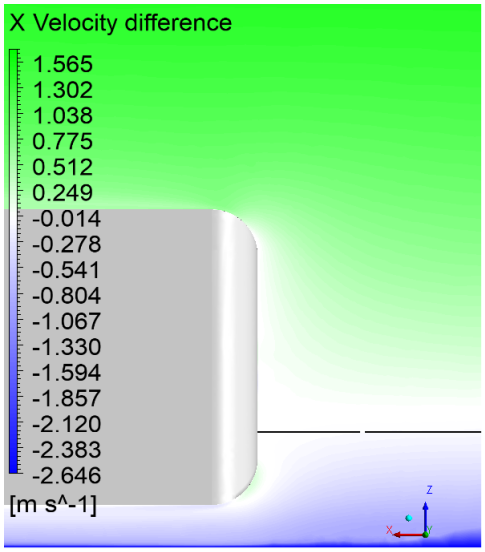


**Figure 3.20:** X Velocity difference [$V_x$(ABL) - $V_x$('No-ABL')] contours near the HDV's front surface (y = 0 plane i.e. side view) (Black line marks the $z = z_{eq}$ line)

Figure 3.19 shows that the ABL profile slows down as it approaches the HDV's front surface stagnation point, eventually reaching zero. As it flows around the corners, the flow accelerates as is represented by the red concentrated areas above and below the front surface curvature. This flow behaviour is similar to what is experienced in traditional constant inflow cases.

The incoming ABL profile is more evident in the difference contour Figure 3.20. The x velocity difference between the 'No-ABL' and the ABL inflow goes from negative (blue) near the lower front radius where $V_T(z)$ is the lowest (3 % lower than $V_{T,eq}$) , zero (white) near $z_{eq}$, where $V_T(z)$ is close to $V_{T,eq}$ to positive (green) above $z_{eq}$, where $V_T(z)$ is higher than $V_{T,eq}$ (4 % higher than $V_{T,eq}$ near the upper front radius). The reader should note that the volume of the HDV above $z_{eq}$ constitutes 74 % of the total HDV volume.

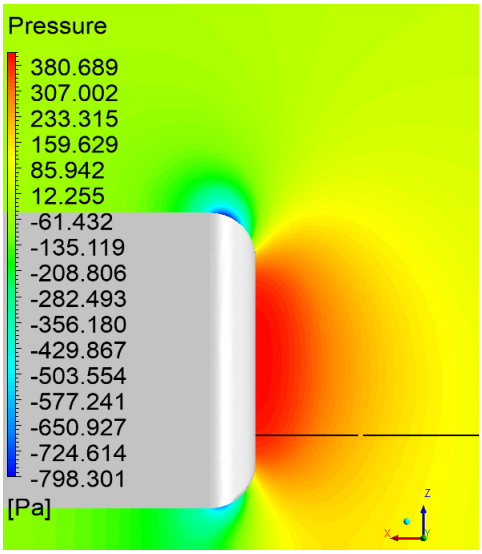


**Figure 3.21:** Pressure contours (for the ABL case) near the HDV's front surface (y = 0 plane i.e. side view) (Black line marks the $z = z_{eq}$ line)

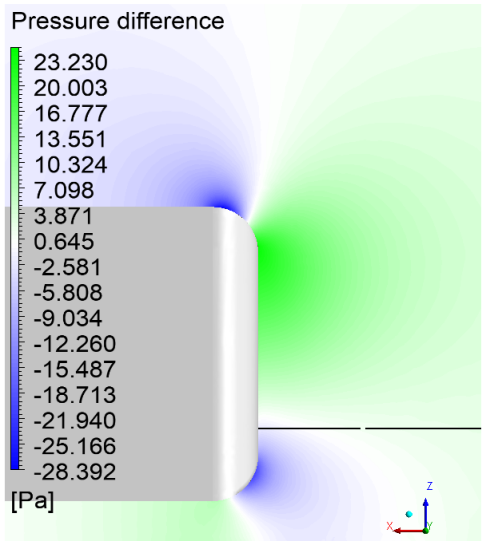


**Figure 3.22:** Pressure difference [p(ABL) - p('No-ABL')] contours near the HDV's front surface (y = 0 plane i.e. side view) (Black line marks the $z = z_{eq}$ line)

Figure 3.21 shows the pressure distribution near the HDV's front surface. As the ABL profile approaches the HDV and comes close to the front surface stagnation point, velocity gets converted to static pressure. The trend is similar to but not fully governed by Bernoulli's theorem, as the flow is not inviscid. This leads to a high pressure region near the front surface. The low pressure cores near the front radius are asymmetrical with the one above being larger than the one below. This is because the upper front radius faces a higher velocity from $V_w(z)$, which upon being accelerated leads to much lower pressure compared to the region near the lower front radius, which faces lower velocity from $V_w(z)$.

Since the ABL case has higher velocities than $V_{T,eq}$ above $z_{eq}$ and velocities lower than $V_{T,eq}$ below $z_{eq}$, that will correspond to higher pressure compared to 'No-ABL' for $z > z_{eq}$ and lower pressure compared to 'No-ABL' for $z < z_{eq}$. This is reflected in Figure 3.22 which represents the pressure difference between the two cases. The area near the stagnation region goes from dark blue at the bottom of the stagnation region to green as one crosses $z_{eq}$ while traversing the HDV's front surface in the z-direction, indicating a transition from a negative difference to a positive difference, as expected.

On the upper front radius, the low pressure core area has a negative difference while on the lower front radius, the low pressure core has a positive difference. This is because on the upper front radius, due to $V_T(z) > V_{T,eq}$, the ABL case gets accelerated to a higher velocity compared to the 'No-ABL' case. From Bernoulli's theorem, the ABL case will have lower pressures there, compared to 'No-ABL'. Similarly, on the lower front radius, the ABL case shall have higher pressures than 'No-ABL'. This phenomenon is marked by a dark blue region on the upper front radius and a green region on the lower front radius in Figure 3.22. One can note that a major portion of the front surface faces higher pressures (by around 20 $Pa$) for the ABL case. This is why the ABL case has a 17% higher front drag than the 'No-ABL' case, as shown in Table 3.6

Figures 3.23, 3.25 and 3.27 further illustrate the increase in pressure as one progresses in the z-direction near the HDV's surface. Figure 3.29 shows the planes on which the data is plotted.

As we proceed in positive z-direction, the high pressure core increases in size. This is again because of higher velocities from $V_w(z)$ at larger heights being converted to higher pressures near the front surface

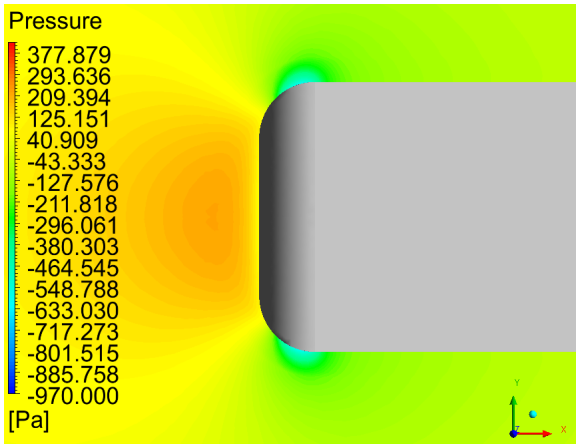


**Figure 3.23:** (Top view) Pressure (for ABL case) contours near the HDV's front surface ($z = 0.75\ m$ plane)

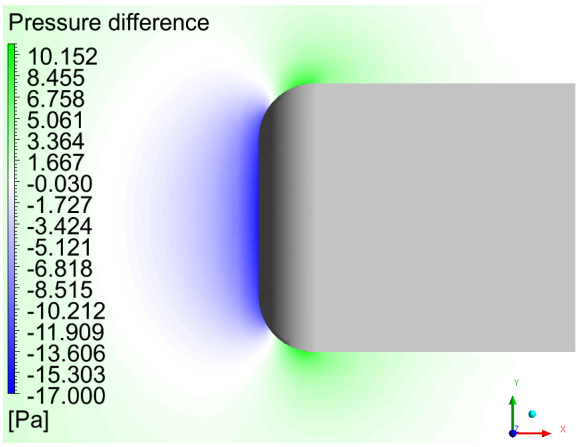


**Figure 3.24:** (Top view) Pressure difference [p(ABL) - p('No-ABL')] contours near the HDV's front surface ($z = 0.75\ m$ plane)

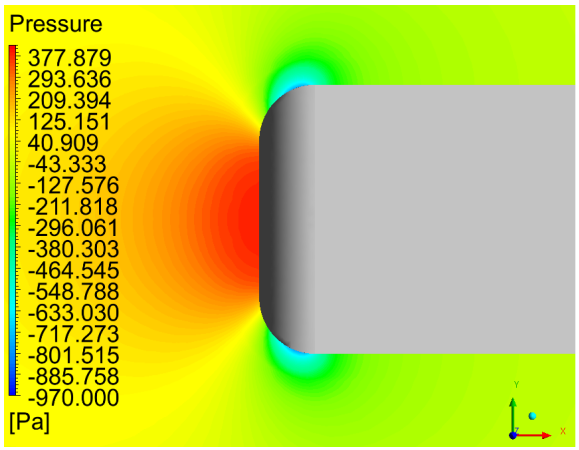


**Figure 3.25:** (Top view) Pressure (for ABL case) contours near the HDV's front surface ($z = z_{eq} = 1.37\ m$ plane)

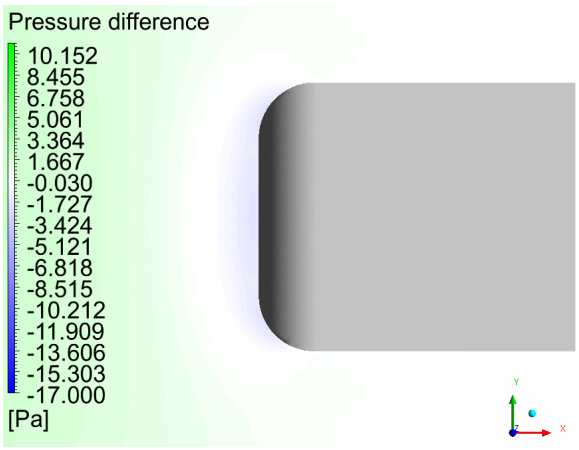


**Figure 3.26:** (Top view) Pressure difference [p(ABL) - p('No-ABL')] contours near the HDV's front surface ($z = z_{eq} = 1.37\ m$ plane)

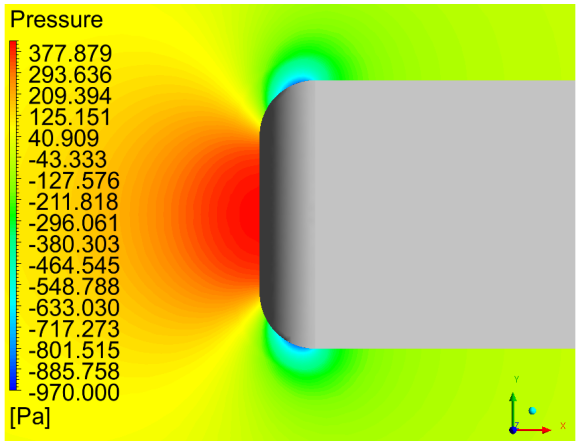


**Figure 3.27:** (Top view) Pressure (for ABL case) contours near the HDV's front surface ($z = 2.25\ m$ plane i.e. mid-HDV height)

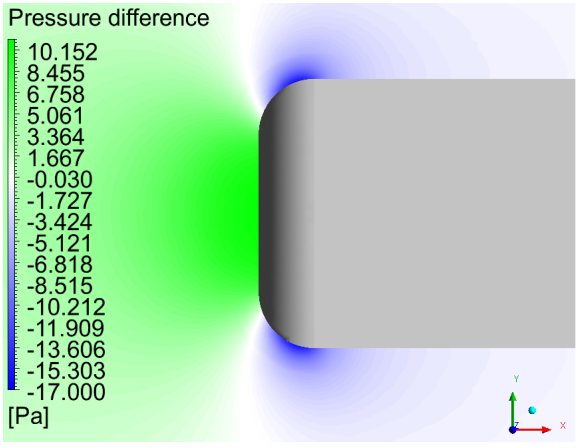


**Figure 3.28:** (Top view) Pressure difference [p(ABL) - p('No-ABL')] contours near the HDV's front surface ($z = 2.25\ m$ plane i.e. mid-HDV height)

The pressure difference between the two cases is illustrated in Figures 3.24, 3.26 and 3.28. Below $z_{eq}$,

negative values are observed in front of the HDV which indicate that the 'No-ABL' case has higher pressure (due to $V_T(z) < V_{T,eq}$) while above $z_{eq}$, positive values are observed in front of the HDV which indicate that the ABL case has higher pressure (due to $V_T(z) > V_{T,eq}$).

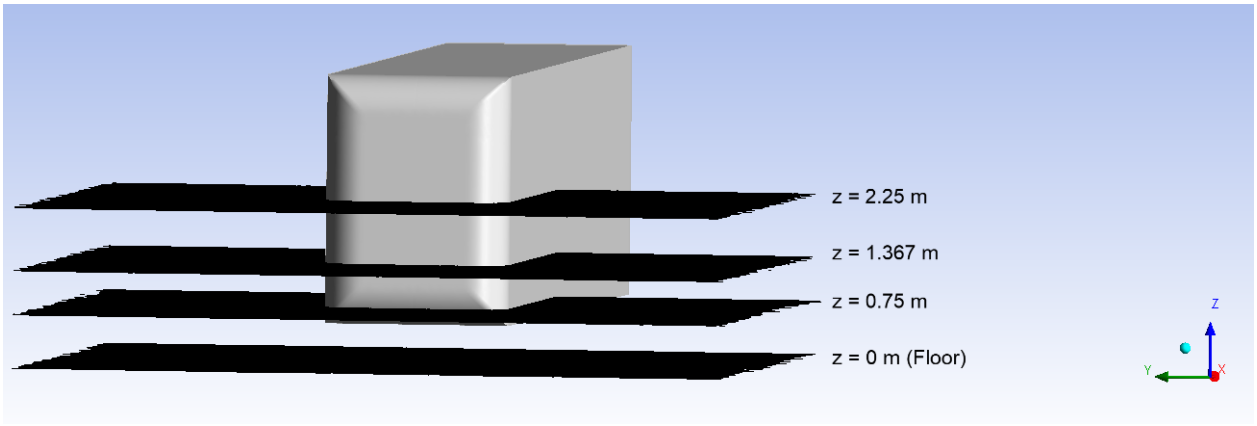


**Figure 3.29:** Various XY planes used to depict pressure contours from the top view

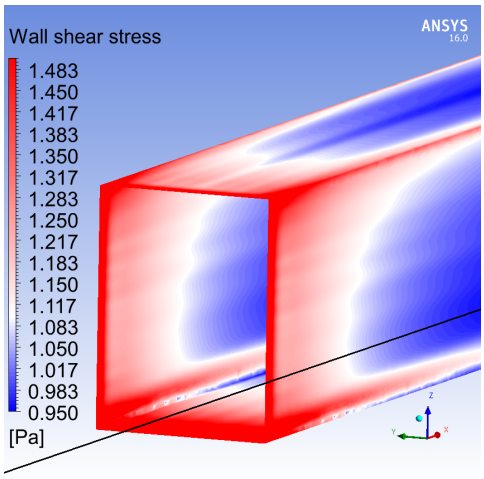


**Figure 3.30:** Wall shear stress (for ABL case) contours on the HDV's side surface (Black line marks the $z = z_{eq}$ line)

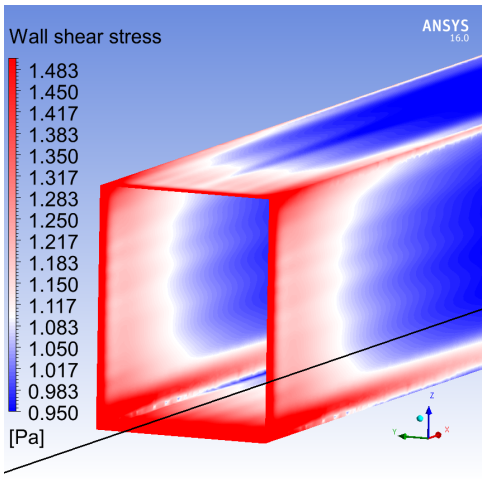


**Figure 3.31:** Wall shear stress (for 'No-ABL' case) contours on the HDV's side surface (Black line marks the $z = z_{eq}$ line)

In Figure 3.30, near the HDV's front radius, the velocity increases and reaches a peak value. However, near the wall, due to friction, flow retards. This creates a large velocity gradient, thus leading to high wall shear stress near the front radius.

When we compare Figures 3.30 and 3.31, this velocity gradient is higher for the ABL case for $z > z_{eq}$ because velocity there is higher for $V_T(z)$ compared to $V_{T,eq}$. This leads to higher wall shear stress compared to the 'No-ABL' case for $z > z_{eq}$. The opposite happens for $z < z_{eq}$ where the 'No-ABL' case has higher wall shear stress than the ABL case. Since the area above $z_{eq}$ is larger than the area below, the ABL case overall faces higher wall shear stress (by a few $Pa$) on the side surfaces. This is the reason the ABL case has 2 % higher side drag as shown in Table 3.6.

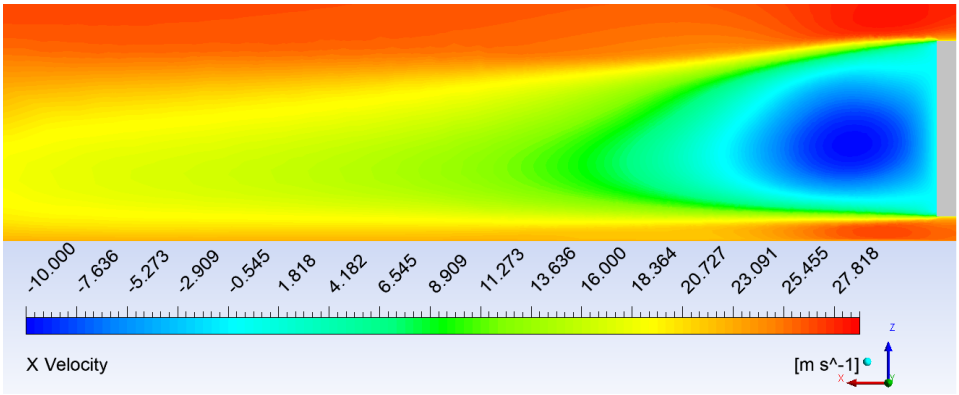


**Figure 3.32:** X Velocity (for ABL case) contours near the HDV's wake region ($y = 0$ plane i.e. side view)

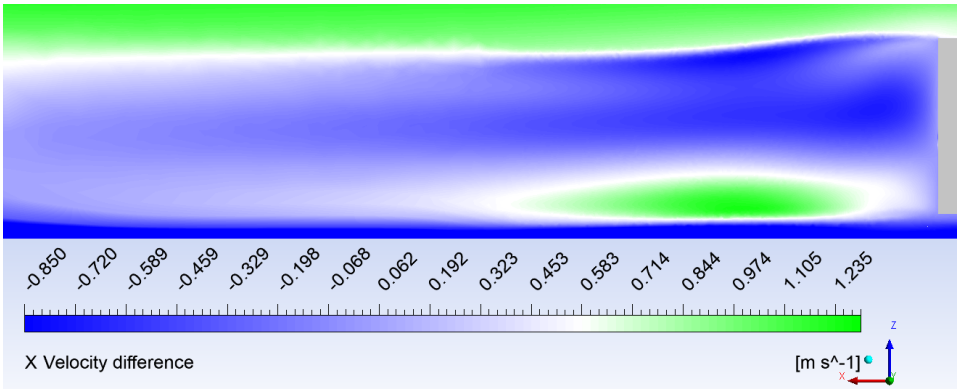


**Figure 3.33:** X Velocity difference [$V_x$(ABL) - $V_x$('No-ABL')] contours near the HDV's wake region ($y = 0$ plane i.e. side view)

While Figure 3.32 shows a wake region for the ABL case which is similar to wake regions experienced with traditional constant inflow cases, Figure 3.33 gives a more detailed look by showing the difference in the wake region between the ABL and 'No-ABL' cases. The backflow region in Figure 3.32 is marked by the dark blue oval surrounded by a light blue border where negative values of x velocity are observed. Beyond this region, reattachment begins and velocity slowly begins to recover.

The upper part of the backflow region has more deceleration for the ABL case than the 'No-ABL' case, as can be noted by the dark blue spot in Figure 3.33. However, the differences are very small, only up to a maximum of 0.85 $m/s$ in the backflow region. The vertical asymmetry above and below $z_{eq}$, which was observed near the HDV's front surface is not observed here on first notice. On a closer look, the upper wake region including the vortex area in the backflow region has darker shades of blue indicating higher deceleration of maximum 0.85 $m/s$ than the 'No-ABL' case while the lower wake region has mixed shades of light blue, white and green, indicating lower deceleration of maximum 1.2 $m/s$ than the 'No-ABL' case. This actually leads to a bigger upper vortex and a smaller lower vortex for the ABL case.

The upper vortex in the backflow region is usually bigger than the lower vortex for bluff bodies in general as observed by Kruijssen [17]. The ABL inflow further increases this difference by enlarging the upper vortex and contracting the lower vortex, which is observed in Figures 3.34 and 3.35. The upper vortex being more dominant due to its size, leads to higher deceleration for the ABL case throughout the wake but more so in the upper wake region.

However in Figure 3.33, as one proceeds in the streamwise direction and reaches the end of the wake region, this deceleration trend vanishes and becomes more uniform portrayed by a whitish blue region indicating negative x velocity differences of only around 0.45 $m/s$. As flow momentum begins to recover and starts approaching the freestream conditions after crossing the wake region, the deceleration trend recedes and the ABL case again has higher velocities above $z_{eq}$ and vice versa.

Figures 3.34 and 3.35 show the iso-surfaces of zero total pressure for both the cases. On the first look, the iso-surfaces look similar. However, on having a closer look, one shall notice that the ABL case iso-surface is

larger in the upper vortex and smaller in the lower vortex. As shown in Figure 3.33, this is because of higher deceleration in the upper wake region and lower deceleration in the lower wake region.

Figures A.1 shows the development of free shear layers as flow crosses the HDV's rear surface, by representing vorticity magnitude in the wake region. These shear layers contribute to the development of the wake region by interacting with the boundary layer and the wake Mastenbroek [1]. Figure A.2 shows that the upper free shear layer has higher vorticity and the lower free shear layer has lower vorticity for the ABL case. This again indicates why the ABL inflow leads to a larger upper vortex and a smaller lower vortex in the wake.

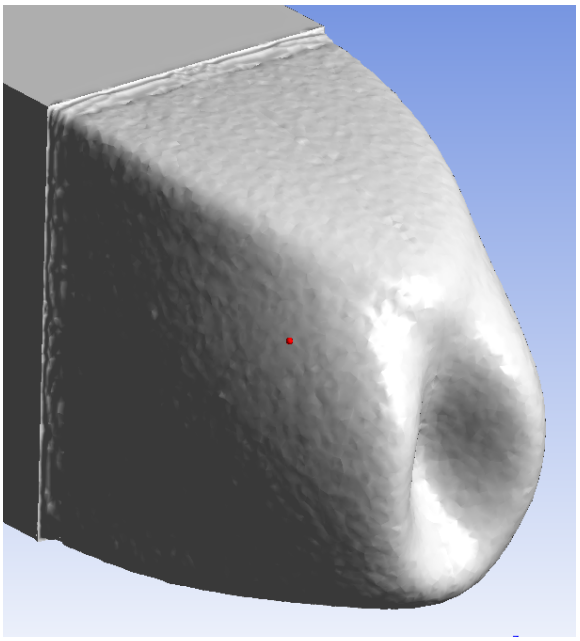

**Figure 3.34:** Total $C_P = 0$ (for ABL case) isosurface in the HDV's wake region

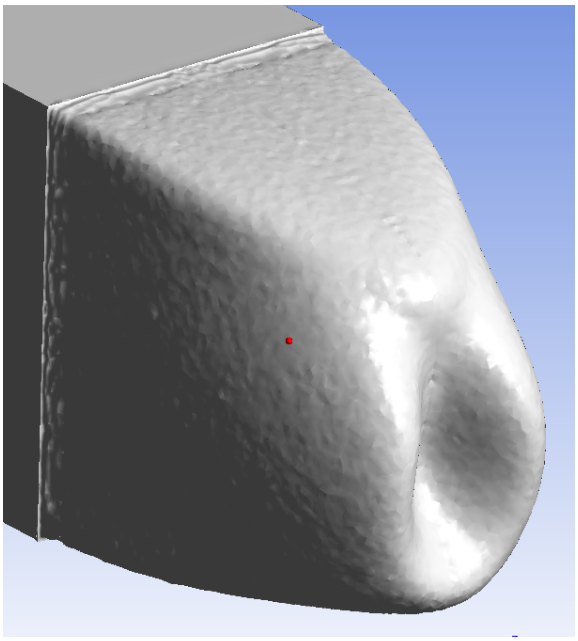

**Figure 3.35:** Total $C_P = 0$ (for 'No-ABL' case) isosurface in the HDV's wake region

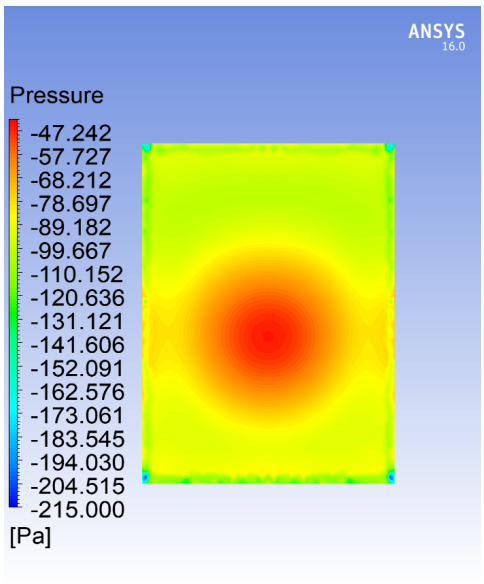


**Figure 3.36:** Pressure (for ABL case) contours on the HDV's rear surface

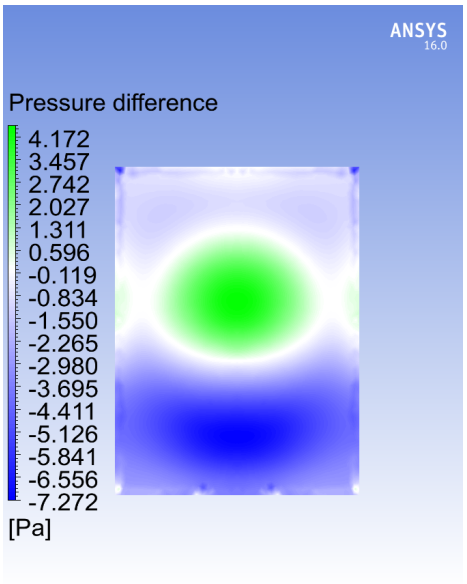


**Figure 3.37:** Pressure difference [p(ABL) - p('No-ABL')] contours on the HDV's rear surface

Flow separation at the rear surface leads to negative pressure, as shown in Figure 3.36. There is a pressure

peak region in the lower middle portion of the rear surface which is observed by Leeuwen [37] also for the GETS model.

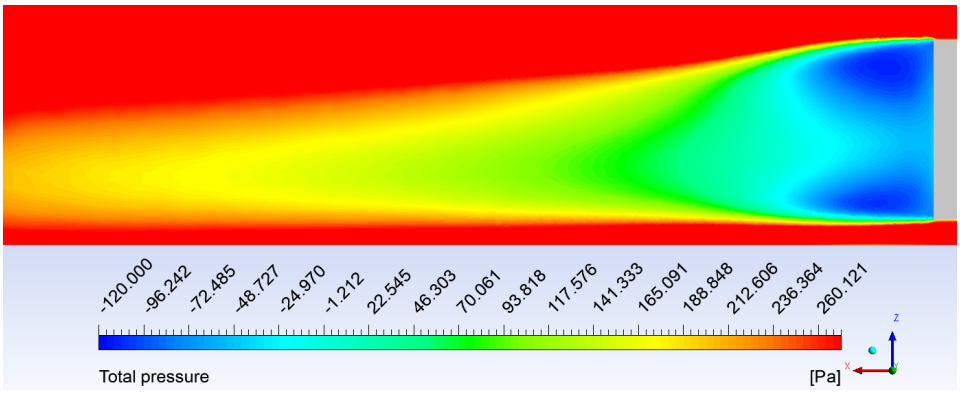


**Figure 3.38:** Total pressure (for ABL case) contours in the HDV's wake region (y = 0 plane i.e. side view)

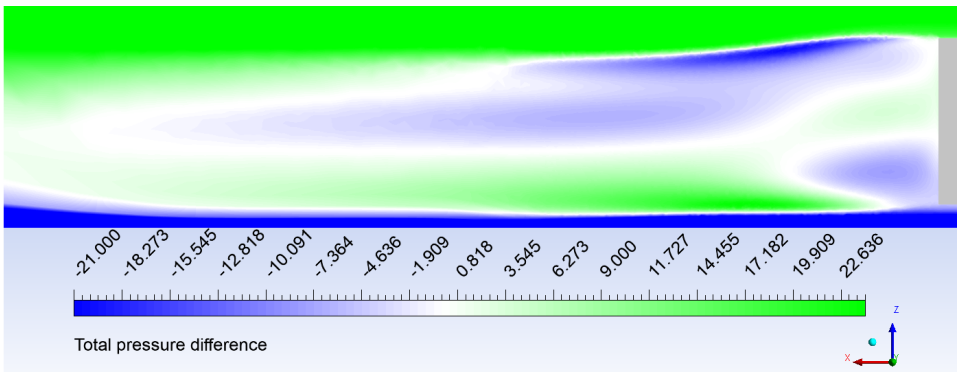


**Figure 3.39:** Total pressure difference [$p_t$(ABL) - $p_t$('No-ABL')] contours in the HDV's wake region (y = 0 plane i.e. side view)

The difference contour Figure 3.37 shows that the central core of the upper rear surface -has positive values, meaning the 'No-ABL' case has lower pressures than the ABL case. However, since the rest of the surface has negative values, this means that the majority of the rear surface has lower pressures for the ABL case. This coincides with the higher decelaration observed for the ABL case in Figure 3.33. This is the reason why the rear drag is slightly higher for the ABL case. Since the maximum negative pressure decrease is only around 7 Pa, the drag increase is also minute. The ABL case suffers 2% higher rear drag as shown in Table 3.6.

Even then, the negative values are less pronounced on the upper portion of the rear surface (less than 2 $Pa$) and more pronounced on the lower portion of the rear surface (up to 7 $Pa$). This means that the pressure decrease is smaller on the upper surface and higher on the lower surface. This will also be observed right behind the HDV's rear surface in Figure 3.39 where the velocity is almost zero. This does not go in line with the explanation that the upper wake faces more decelaration for the ABL case than the lower wake. The mechanism behind such a trend observed in Figure 3.37 is unknown as of now and can be attributed to the unsteady vortex circulation present in the highly viscous backflow region.

Figure 3.38 shows negative total pressure around the backflow region indicating total pressure loss caused by flow separation due to the formation of wake vortices as discussed in chapter 1. One can see that the upper vortex is greater in size than the lower one similar to the wake observed by Duell [11] and discussed in chapter 1.

Figure 3.39 shows that the area right behind the rear surface around the backflow region follows a difference trend similar to Figure 3.37. Post thte backflow region, as reattachment begins, the upper portion of the wake has lower total pressure for the ABL case (by up to 20 $Pa$) and the lower portion has higher total pressure for the ABL case (by up to 22 $Pa$). This is in line with the results showed in Figure 3.33 where higher decelaration was observed in the upper wake region and lower decalaration was observed in the lower wake region post reattachment, for the ABL case. Since this decelaration trend in the wake post reattachment, is observed

in both total pressure and x velocity plots, this means that differences in static pressure values between the two cases are not high.

Once again as the wake region ends and the flow starts regaining momentum, the total pressure trend goes back to values observed at the inflow where higher total pressure will be observed above $z_{eq}$ and lower below $z_{eq}$.

### 3.8.1. Drag force

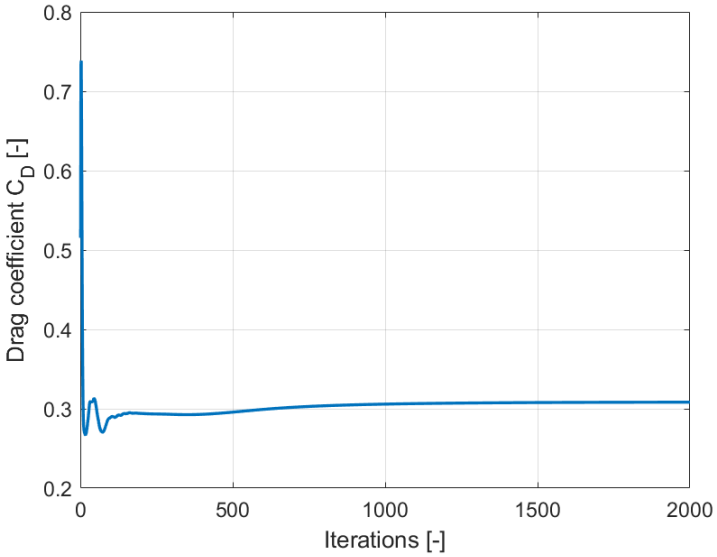


**Figure 3.40:** Residual of $C_D$ showing convergence

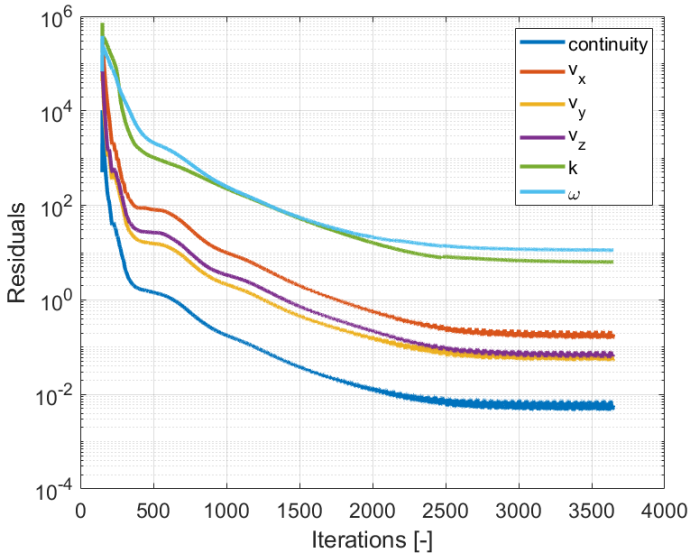


**Figure 3.41:** Residual of the physical variables showing convergence

First the convergence of the drag coefficient is checked. The $C_D$ residual is plotted in Figure 3.40. Convergence is obtained within 1500 iterations as can be seen by the flattening of the residuals. This is because of the use of the coupled solver which accelerates convergence.

Figure 3.41 shows that all physical variables attain convergence even though the specified convergence value of O($10^{-6}$) has not been reached. Most residuals oscillate about a mean value after a certain number of iterations. When this mean value becomes constant, the residuals have converged. This is observed after

approximately 3500 iterations in Figure 3.41. The oscillations occur because a steady solver is being used to simulate unsteady flow.

As can be noticed in Table 3.6, the drag force and all of its components are higher for the ABL case. For the rear drag, one can understand by looking at Figures 3.33 and 3.39 show that the ABL case faces more decelaration than the 'No-ABL' case, in a larger portion of the wake region, hence facing 2% higher rear drag. This also explains why the pressure drag is 4% higher.

$z = z_{eq}$ marks the height of the bottom one-fourth part of the HDV. This is why the front drag is higher for the ABL case because the area above $z_{eq}$ (which is three-fourth of the HDV) is larger than the area below $z_{eq}$. This means that for the ABL case, a larger area faces higher velocities while a smaller area faces lower velocities. Thus, the larger area above $z_{eq}$ shall face more drag while the smaller area below $z_{eq}$ faces much lesser drag. Overall, this leads to a 17% higher drag on the front surface for the ABL case.

Side drag and skin friction drag are minutely (2%) higher for the ABL case. This is because of the overall higher wall shear stress faced by the ABL case as shown in Figure 3.30.

Due to higher drag components for the ABL case, the total drag for the ABL case is 3.5% more than the 'No-ABL' case.

Table 3.7 shows that the bottom portion of the HDV $z < z_{eq}$ faces a 3% higher drag force for the 'No-ABL' case because the 'No-ABL' case faces higher velocities. The opposite happens for $z > z_{eq}$ where the ABL case faces higher velocities and thus faces 5% higher drag.

| | Front drag (N) | Side drag (N) | Rear drag (N) | Drag (N) | Pressure drag (N) | Skin friction drag (N) |
|---|---|---|---|---|---|---|
| **HDV with ABL** | 122.2 | 212.3 | 796.2 | 1130.7 | 895.6 | 235.1 |
| **HDV with no ABL** | 104.6 | 207.5 | 781 | 1093.1 | 863.2 | 229.8 |

**Table 3.6:** Drag force and its components

| **Drag force (N)** | $z > z_{eq}$ | $z < z_{eq}$ |
|---|---|---|
| **ABL** | 935.6 | 195.1 |
| **'No-ABL'** | 891.8 | 201.3 |

**Table 3.7:** Drag force faced by the HDV for $z > z_{eq}$ and $z < z_{eq}$

## 3.8.2. Effect of the geometry on ABL development

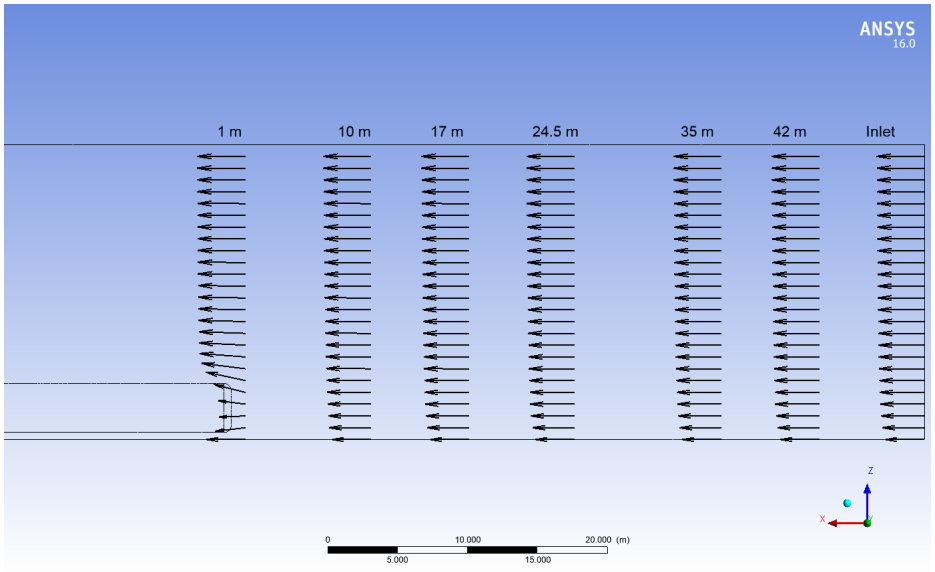


**Figure 3.42:** ABL profile development from inlet to 1 m in front of the HDV ($y = 0$ plane)

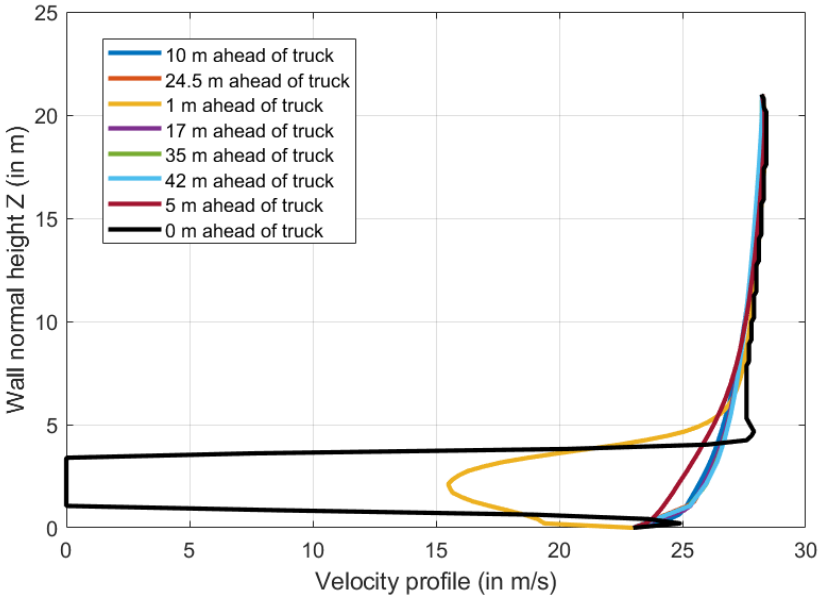


**Figure 3.43:** Development of the ABL input profile from the inlet to 1 m in front of the HDV ($y = 0$ plane)

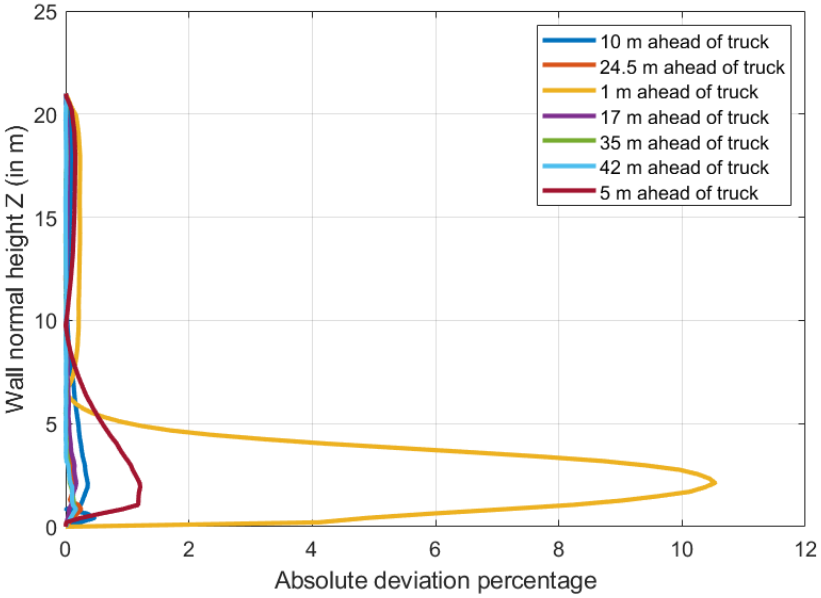


**Figure 3.44:** Absolute value of deviation from the input profile (as percentage) through the domain till 1 m in front of the HDV ($y = 0$ plane)

The effect of the HDV geometry on the development of the ABL profile is shown qualitatively in Figure 3.42 and quantitatively in Figures 3.43 and 3.44. Figure 3.42 shows that there is minimal development as the profile traverses through the domain. Development becomes significant only when the ABL profile comes very close to the HDV as shown in Figure 3.43 where deviation is observed qualitatively when the profile comes 5 m in front of the inlet.

Figure 3.44 shows that even when the ABL profile comes 10 m in front of the HDV, the maximum deviation incurred is only 2%. The increase in deviation post this point can be attributed to the presence of the geometry. Hence, the upstream effect of the HDV begins less than 10 m from the truck front surface. The above figures also show that the objective of limiting the development of the ABL till the point that it reaches

the HDV has been successful.

### 3.8.3. Effect of an attached boat-tail

To analyse the effect of an attached boat-tail to an HDV and its efficacy when an ABL inflow is used, we attach a boat-tail to the rear surface of the GETS model. The boat-tail has its top and side panels curved at an angle of 12°. The bottom panel is parallel to the HDV. The modified geometry is shown in Figures 3.45, 3.46 and 3.47. The numerical setup including the domain, mesh, prism layer and the solver settings are exactly the same for the modified geometry.


**Figure 3.45:** Modified GETS model with the boat-tail attached (side view)


**Figure 3.46:** Top panel of the attached boat-tail (top view)

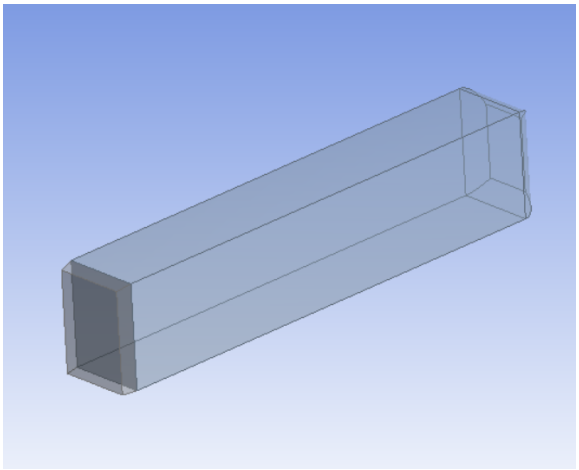

**Figure 3.47:** Isometric view of the boat-tail

As discussed before in chapter 1, the boat-tail reduces pressure drag by increasing base pressure. It does so by making the change in geometry at the HDV's rear surface less abrupt. This is shown in Figure 3.48 where the pressure experienced is much less than what is shown in Figure 3.36 where a boat-tail is absent. Both the minimum and maximum values have increased, thus exhibiting good pressure recovery. The pressure peak is shifted downwards by the boat-tail. Since the upper panel is curved but the lower panel is not, the upper wake vortex decreases in size much more than the lower wake vortex as shown in Figure 3.50. This shift in mass and momentum is the reason behind the pressure peak shifting downward. The positive circular region in Figure 3.49 also shifts downwards because of this. One should note that this behaviour is depicted only for this particular configuration of the boat-tail.

Looking at Figure 3.49, the pressure difference between the ABL and the 'No-ABL' case has decreased so much that the maximum value of the difference is only a mere 2 $Pa$. This means that this boat-tail reduces the differences brought by the ABL inflow. The ABL inflow only slightly increased the size of the upper vortex while the boat-tail decreased its size significantly. On the other hand, the ABL inflow only slightly decreased the size of the lower vortex while the boat-tail decreased it moderately. This can be observed by comparing Figures 3.32 and 3.50. The size reducing effect on the wake caused by the boat-tail is more dominant than the changes brought by the ABL inflow.

Another thing to note is the pressure difference trend observed in Figure 3.49 which is similar to what is seen in Figure 3.37. A central circular positive pressure difference region surrounded by mildly negative pressure difference above and strongly negative pressure difference observed below. Even though the magnitudes have decreased, the pressure difference trend does not change. This is also observed in the backflow region right behind the rear surface of the boat-tail in Figure 3.53. The mechanism behind this is unexplained but it is present even when the boat-tail is attached.

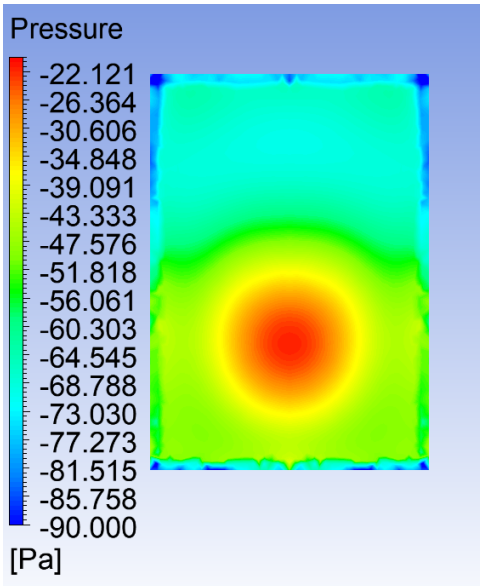


**Figure 3.48:** Pressure (for ABL case) contours on the boat-tail's rear surface

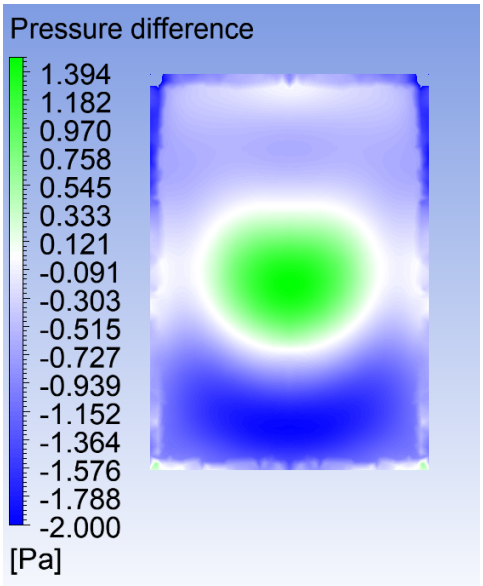


**Figure 3.49:** Pressure difference [p(ABL) - p('No-ABL')] contours on the boat-tail's rear surface

Figure 3.50 shows the reduced wake size caused by the boat-tail attachment. Figure 3.51 shows that the difference in the x-velocity magnitudes for the two cases has significantly decreased. The backflow region has x-velocity differences of only $0.1-0.2$ $m/s$, compared to $0.7-0.8$ $m/s$ in Figure 3.33.

The deceleration trend observed in Figure 3.33 in the wake region is not present in the wake region behind the boat-tail in Figure 3.51. This is because of the boat-tail reducing the size of the wake vortices and therefore reducing the effect of the ABL inflow. Since the ABL inflow effect is reduced, the deceleration in the wake region becomes uniform.

Total pressure values shown in Figure 3.52 display higher total pressure ($-75$ $Pa$) in the backflow region compared to Figure 3.38 where the total pressure in the backflow region goes down to a minimum of ($-120$ $Pa$). The size of the backflow region has also reduced. The backflow region shown in Figure 3.53 mostly has negative difference values but their values mostly lie between -2 and 0 $Pa$, stating that both cases have similar flow pattern in the wake region

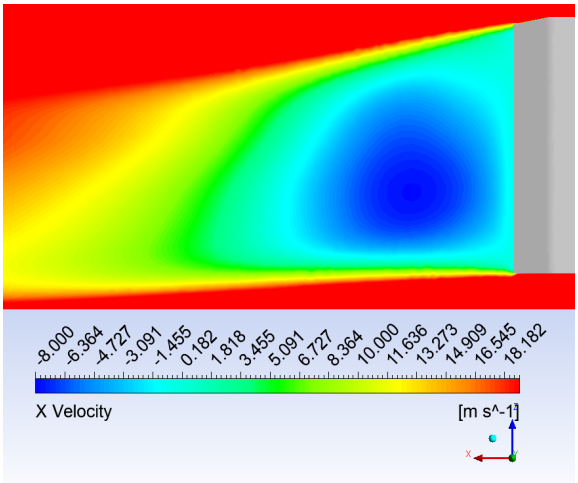


**Figure 3.50:** X Velocity (for ABL case) contours near the boat-tail's wake region ($y = 0$ plane i.e. side view)

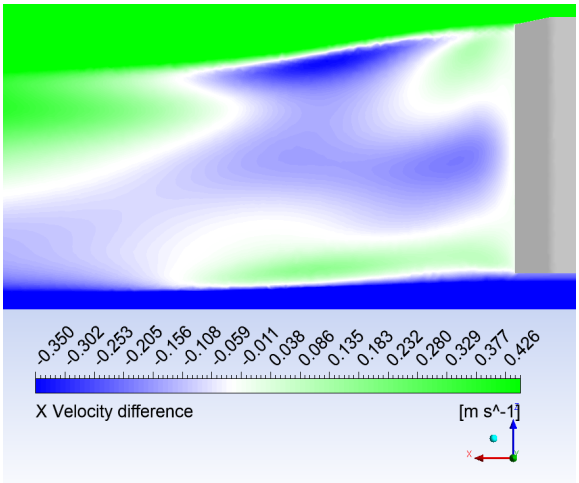


**Figure 3.51:** X Velocity difference [$V_x$(ABL) - $V_x$('No-ABL')] contours near the boat-tail's wake region ($y = 0$ plane i.e. side view)

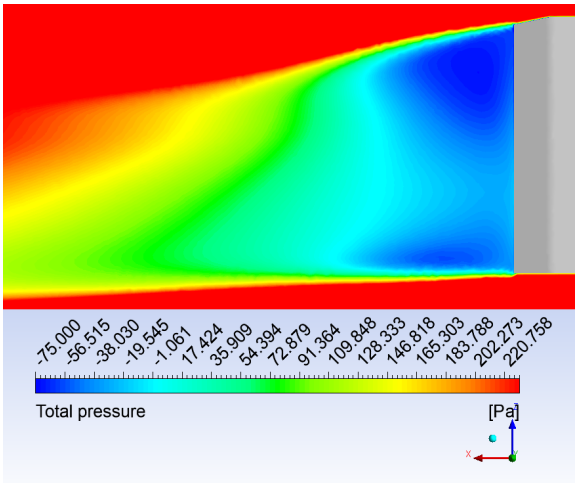


**Figure 3.52:** Total pressure (for ABL case) contours near the boat-tail's wake region ($y = 0$ plane i.e. side view)

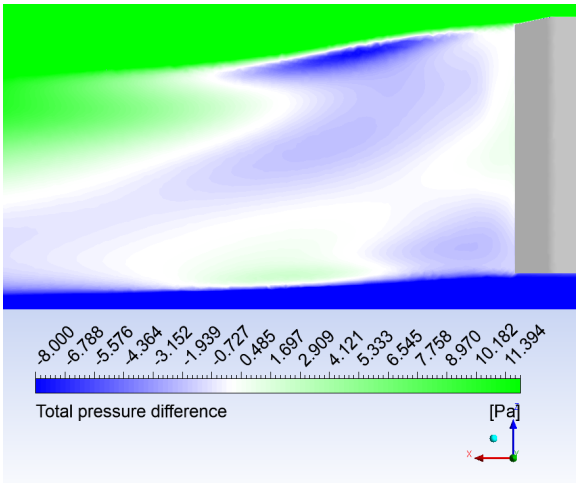


**Figure 3.53:** Total pressure difference [$p_t$(ABL) - $p_t$('No-ABL')] contours near the boat-tail's wake region ($y = 0$ plane i.e. side view)

## Drag force reduction

| | **Drag (N)** | **Drag reduction caused by boat-tail** |
|---|---|---|
| **ABL with boat-tail** | 904.2 | 20 % |
| **'No-ABL' with boat-tail** | 874.9 | 20 % |

**Table 3.8:** Drag force and drag reduction experienced by both the ABL and 'No-ABL' cases when a boat-tail is attached

Table 3.8 shows the drag forces attained when a boat-tail is attached to both the ABL and 'No-ABL' cases. With an attached boat-tail, the drag force for the ABL case is 904.2 $N$ while for the 'No-ABL' case is 874.9 $N$. The decrease in drag force with the attachment of a boat-tail is 20% for both the ABL case and 'No-ABL' cases. This means that the use of ABL as an inflow has a very minute, practically negligible effect on the drag-reducing

capabilities of the boat-tail. However, since the ABL case with the attached boat-tail still has higher overall drag compared to the 'No-ABL' case, this means that the ABL inflow effect still exists, even though it has a less impact compared to the cases without a boat-tail. This may be because the boat-tail only affects the base pressures in the wake region due to which the front and side drag values will be unaffected. Hence, differences between the ABL and 'No-ABL' cases will remain even with a boat-tail due to differences in front and side drag.

## 3.9. Summary

1. The ABL inflow effect induces slightly more drag by reshaping the wake vortex in such a way that the upper vortex increases in size and the lower vortex decreases in size. Since the upper vortex is more dominant in size compared to the lower vortex, that may be leading to more decelaration for the ABL case which is particularly larger in the upper wake region than the lower wake region.

2. The function of the boat-tail is to recover pressure by ensuring a gradual change of geometry from the curved panels after flow crosses the HDV's top surface. This decreases the amount of separation, thus reducing the wake size. For our particular configuration, the upper vortex size gets significantly reduced and the lower vortex size gets moderately reduced. This effect is much more dominant than the ABL inflow effect thereby reducing the difference brought on by the ABL inflow. This is why the difference between the ABL and 'No-ABL' case gets decreased when this particular boat-tail is attached. The drag reduction efficiency of the boat-tail is unaffected by the ABL inflow.

3. Due to higher pressure on the front surface and higher wall shear stress on the side surface above $z_{eq}$, the ABL case faces 17% higher front surface drag and 2% higher side surface drag compared to the 'No-ABL' case. Lower pressures on the rear surface and lower velocities in the wake region lead to 2% higher rear drag for the ABL case. Overall, the ABL case faces 3.5 % more total drag than the 'No-ABL' case.

# 4

# HDV Aerodynamics - Effect of non-zero wind yaw angle $\psi$

This chapter focuses on the effect of a non-zero yaw angle on the ABL simulations across an HDV. Section 4.1 specifies the changes in the numerical setup which were introduced because of a non-zero wind yaw angle. Section 4.2 presents and explains the results obtained by dividing them into two parts for more clarity. One part describes the effect of the ABL inflow on the cases with a non-zero wind yaw angle and the other part describes the effect of the wind yaw angle on the ABL inflow. Changes in drag force trends due to these effects are explained. Section 4.2.3 then explains the changes brought by the attachment of a boat-tail when a non-zero wind yaw angle is used. Finally, section 4.3 summarises the findings.

## 4.1. Changes in numerical setup

Due to the presence of a non-zero wind yaw angle $\psi$, the inflow at the inlets is going to change because a lateral velocity component will be added at the inlets. The orientation of the incoming velocity vectors among themselves and how the geometry is going to encounter them is shown in Figure 4.1.

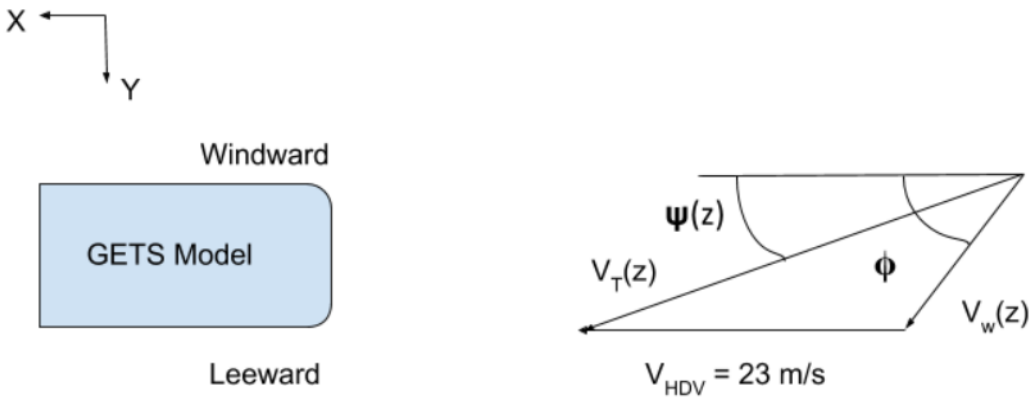


**Figure 4.1:** Schematic showing the orientation of driving velocity $V_{HDV}$ and wind velocity $V_w(z)$ w.r.t. the geometry (Top view)

Since due to the ABL profile $V_w(z)$, the wind velocity will vary with height, according to (1.7), the wind yaw angle will also vary with height. The wind yaw angle $\psi(z)$ looks as shown in Figure 4.2.

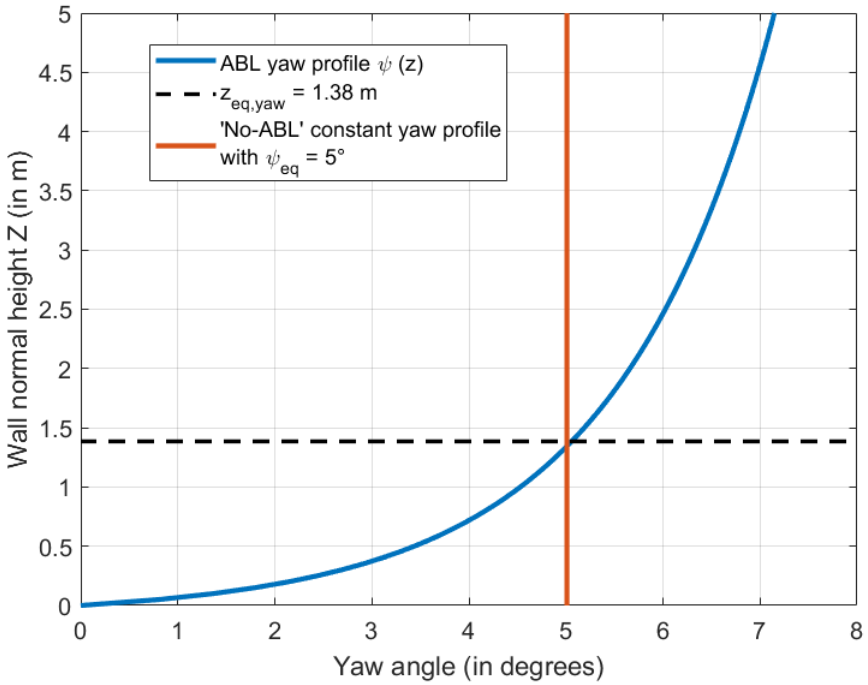


**Figure 4.2:** Wind yaw angle variation in z-direction

For easier interpretation and plotting of results, we define an equivalent wind yaw angle. Before presenting results for the HDV simulation, we calculate the reference velocity for the non-zero $\psi$ case and the equivalent wind yaw angle using a procedure similar to what was described before.

$$\psi_{eq} = \frac{1}{H_m}\int_0^{H_m} \psi(z)\, dz. \tag{4.1}$$

$$\text{where } \psi(z) = tan^{-1}\frac{V_{T,y}(z)}{V_{T,x}(z)}. \tag{4.2}$$

$$V_{T,y}(z) = V_w(z)sin(\phi) = \frac{3}{log(21)}log\frac{z+z_O}{z_O}sin(\phi). \tag{4.3}$$

$$\text{and } V_{T,x}(z) = V_{HDV} + V_w(z)cos(\phi) = 23 + \frac{3}{log(21)}log\frac{z+z_O}{z_O}cos(\phi). \tag{4.4}$$

To observe the effect of the wind yaw angle, we aim $\psi_{eq} = 5°$ for our numerical setup. An equivalent wind yaw angle of 5° is chosen based on the literature study in chapter 1. Yaw simulations are performed by adding a lateral wind component to both the inlets.

To obtain this, we use a trial and error method where different values of $\phi$ are inserted in (4.1), so as to obtain $\psi_{eq} = 5°$. By doing this, the value of $\phi$ comes out to be 54.71°. This leads to $\psi_{eq} = 5.01°$.

$V_{T,eq}$ also has to be recalculated because of a non-zero $\phi$. We define it by $V_{T,eq,yaw}$ and calculate it by integrating the total velocity magnitude over the HDV's height.

$$V_T(z) = \sqrt{V_{T,y}^2(z) + V_{T,x}^2(z)}. \tag{4.5}$$

$$V_{T,eq,yaw} = \frac{1}{H_m}\int_0^{H_m} V_T(z)\, dz = 24.6\ m/s. \tag{4.6}$$

$V_{T,eq,yaw} = 24.6\ m/s$ is used as the reference velocity for the $\psi_{eq} = 5°$ case.

We then reinsert the value of $V_{T,eq,yaw}$ in the equation of $V_T(z)$ to get the value of $z_{eq,yaw}$, which comes out to be $z = 1.38\ m$. This is the height at which the ABL case experiences $V_{T,eq,yaw}$. Similar to the zero yaw

case, at heights above $z_{eq,yaw}$, the ABL case will have higher velocities in the inflow and below $z_{eq,yaw}$, it will have lower velocities. One should note that $V_{T,eq,yaw} < V_{T,eq}$.

The reader should note that $V_{T,eq,yaw}$ and $\psi_{eq}$ are experienced at different heights. While $\psi_{eq}$ is experienced at $z = 1.35\ m$, $V_{T,eq,yaw}$ is experienced at $z = 1.38\ m$. The equivalent value for both variables cannot be obtained at the same height. However to avoid confusion, we assume that the heights are the same for both $V_{T,eq,yaw}$ and $\psi_{eq}$. This is a safe assumption as both heights have a very small difference.

## 4.2. Results

Before we proceed to the results, one should note the changes made in the computational setup. The inner refinement box size is increased for the yaw case, so as to capture flow physics on the leeward side of the model. While the spanwise dimension of the inner refinement box is $1.2W_m$ for the zero yaw case, for the non-zero yaw case, it is increased to $1.8W_m$. This can be observed in Figures 4.3 and 4.4.

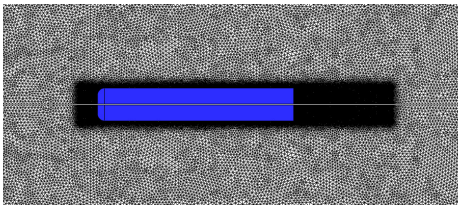

**Figure 4.3:** Top view of the computational mesh for zero yaw case

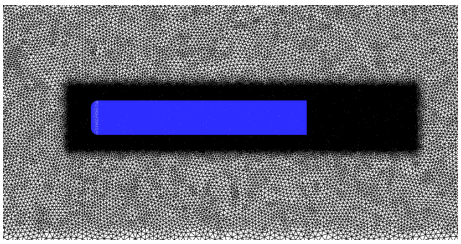

**Figure 4.4:** Top view of the computational mesh for non-zero yaw case

### 4.2.1. Effect of the ABL inflow on non-zero $\psi$

This section compares two cases where both face a non-zero wind yaw angle $\psi_{eq} = 5°$. The difference between the two is brought solely by the ABL inflow, similar to the previous chapter. The reader is urged to only focus on the effect of the ABL when looking at quantitative results. Due to the presence of a wind yaw angle, one can notice qualitative changes by comparing the results with the previous chapter, such as shifting of trends in the y-direction. One cannot quantitatively determine the effect of yaw on the ABL inflow in this section, such as drag changes induced by the introduction of yaw in ABL inflow cases. Hence, a separate section i.e. section 4.2.2 is dedicated to this, which begins right after this section.

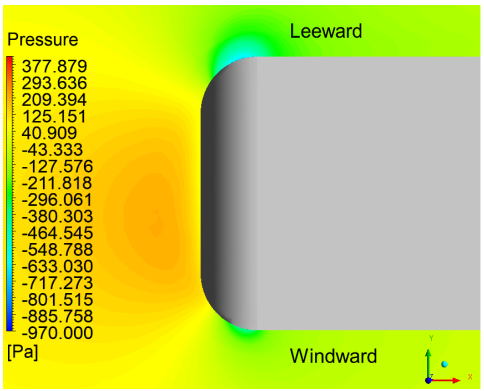


**Figure 4.5:** (Top view) Pressure (for ABL case with yaw) contours near the HDV's front surface ($z = 0.75\ m$ plane)

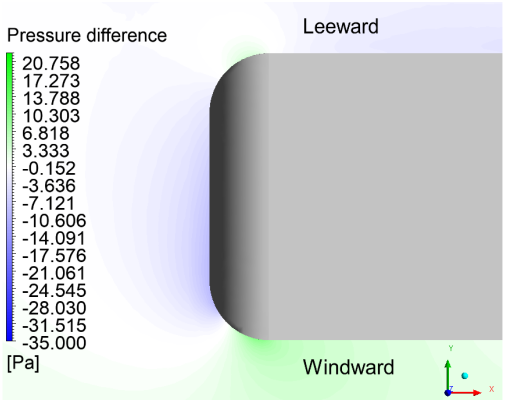


**Figure 4.6:** (Top view) Pressure difference [p(ABL) - p('No-ABL')] (with yaw) contours near the HDV's front surface ($z = 0.75\ m$ plane)

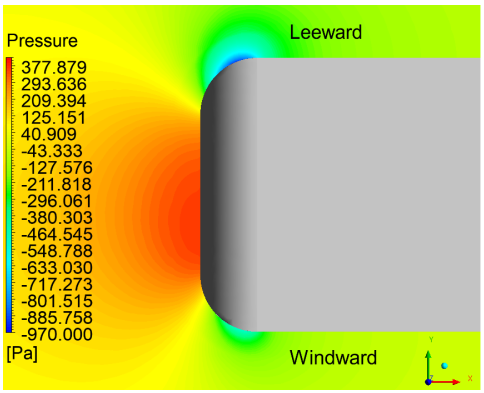


**Figure 4.7:** (Top view) Pressure (for ABL case with yaw) contours near the HDV's front surface ($z = z_{eq,yaw} = 1.38\ m$ plane)

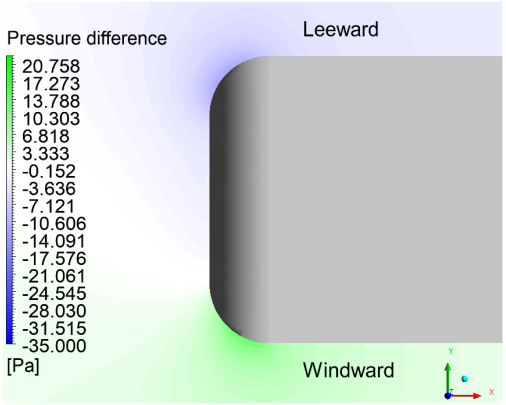


**Figure 4.8:** (Top view) Pressure difference [p(ABL) - p('No-ABL')] (with yaw) contours near the HDV's front surface ($z = z_{eq,yaw} = 1.38\ m$ plane)

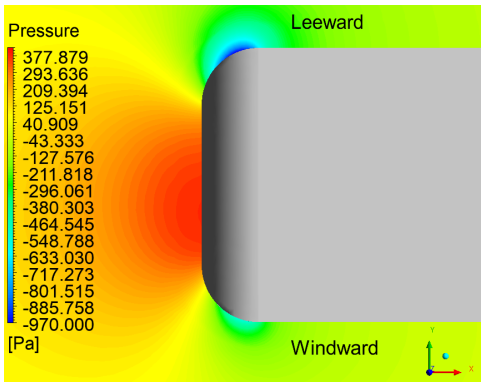


**Figure 4.9:** (Top view) Pressure (for ABL case with yaw) contours near the HDV's front surface ($z = 2.25\ m$ plane i.e. mid-HDV height)

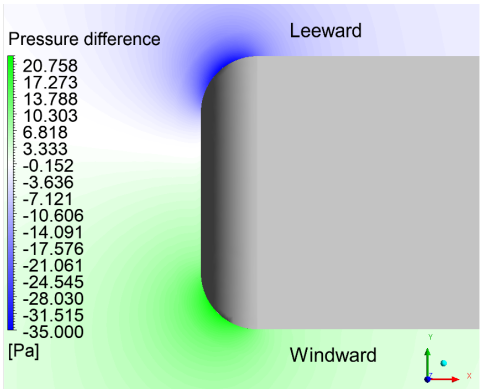


**Figure 4.10:** (Top view) Pressure difference [p(ABL) - p('No-ABL')] (with yaw) contours near the HDV's front surface ($z = 2.25\ m$ plane i.e. mid-HDV height)

Figures 4.5, 4.7 and 4.9 represent how the pressure varies for the ABL case with yaw as we proceed in the z-direction. The crosswind flows in the positive y-direction. One can notice that the high pressure core in front

of the HDV's stagnation region shifts to the windward side. Also, the low pressure cores on the side radiuses are different in size. While the leeward core is larger, the windward core is smaller. This is because the yawed inflow has to turn across the HDV by a larger angle on the leeward side which will accelerate the flow more on the leeward side compared to the windward side where the flow has to turn by a smaller angle which will accelerate the flow less, leading to lower pressures on the leeward side and higher pressures on the windward side (compared to the $\psi = 0°$ case).

As we go from $z = 0.75\ m$ to $z = 2.25\ m$, both the high pressure area near the stagnation region and the low pressure area near the curved side radius increase in size. This is because of the increase in velocity as we proceed in the z-direction. The higher velocities lead to higher pressure in the stagnation region and lower pressure near the curved side radius area.

Figures 4.6, 4.8 and 4.10 represent how the difference between the two cases looks like when we proceed in the z-direction. Both the velocity and the wind yaw angle $\psi$ increase in the z-direction. Now if the wind yaw angle had not been varying and only velocity differences had been there, we would have observed a negative difference (dark blue) near the front surface stagnation region at $z = 0.75\ m$, followed by an almost zero value (white) at $z = z_{eq,yaw}$, then a positive difference (green) near the front surface stagnation region, just like Figures 3.24, 3.26 and 3.28.

However with the presence of a wind yaw angle varying in the z-direction in the ABL case, at $z < z_{eq,yaw}$, the 'No-ABL case' has higher wind yaw angle. Due to this, the negative pressure difference (blue region near the front surface stagnation region) on the windward side is larger than what is observed on the leeward side. As we go to $z > z_{eq,yaw}$, the ABL case has a higher wind yaw angle. Because of this, the positive pressure differences on the windward side (green region near the front surface stagnation region) are larger than what is observed on the leeward side.

To summarize, an increase in velocity in the z-direction leads to pressure differences which increase/decrease the magnitude (hence, size) of the green (high positive pressure difference) or blue (high negative pressure difference) spots in the pressure difference contours. On the other hand, an increase in wind yaw angle in the z-direction shifts the green/blue spots near the front surface stagnation region in the y-direction depending on whether $z < z_{eq,yaw}$ or $z > z_{eq,yaw}$.

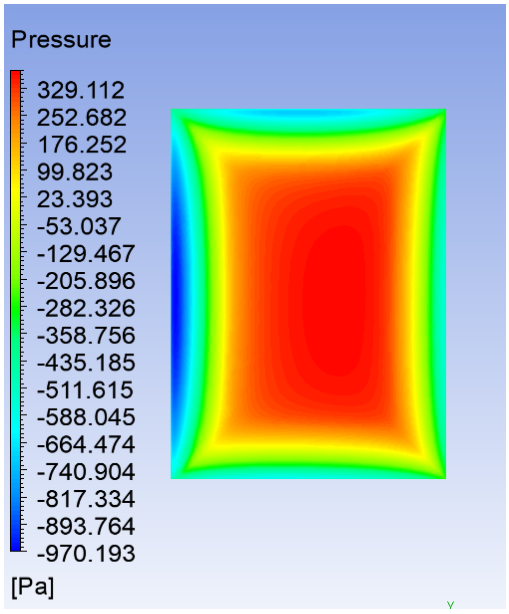


**Figure 4.11:** Pressure contours (for ABL case with yaw) on the HDV's front surface

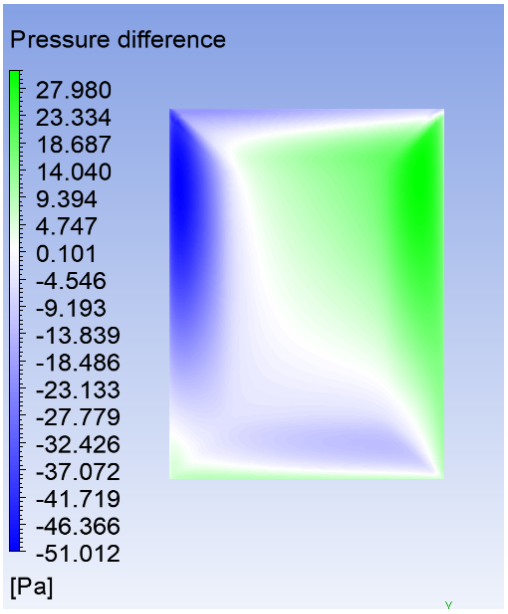


**Figure 4.12:** Pressure difference [p(ABL) - p('No-ABL')] contours on the HDV's front surface

Figure 4.11 shows how the pressure values differ on the front surface when compared to pressure values seen near the front surface in Figure 3.21 for zero $\psi$. The value of the maximum pressure experienced reduced from 380 $Pa$ to 330 $Pa$. This means that lower pressures are faced by the front surface when a non-zero wind yaw angle is introduced. This happens because the front surface faces lower equivalent relative velocity

($V_{T,eq,yaw} < V_{T,eq}$) when a non-zero $\psi$ is introduced. The rear surface however does not face much of a difference in pressure values when a wind yaw angle is introduced, as can be seen by comparing Figures 4.15 and 3.36. This explains why the front drag values reduce when a wind yaw angle is introduced, as the pressure difference between the front and the back region decrease. A shift of the pressure values towards the windward side in Figure 4.11 is also observed, as shown before.

The pressure difference distribution in Figure 4.12 is similar to the top view pressure difference contours in Figures 4.6, 4.8 and 4.10. Looking at Figure 4.12, on first glance, it may seem that positive difference values dominate. However the magnitude of the negative difference values (up to 50 $Pa$) is greater than that of the positive difference values (up to 29 $Pa$). This means that for a major portion of the front surface, the 'No-ABL' case faces higher pressure. Due to higher pressure differences across the HDV for the 'No-ABL' case, it faces 5.5% higher front surface drag as shown in Table 4.1. This is different from the $\psi = 0°$ case where the ABL case had higher front surface drag. However, since the pressure difference distribution across the front surface varies throughout and does not suggest higher pressure for the 'No-ABL' case for a major part of the front surface, the front surface drag change is lower (5.5 %) compared to the $\psi = 0°$ case (17 %)

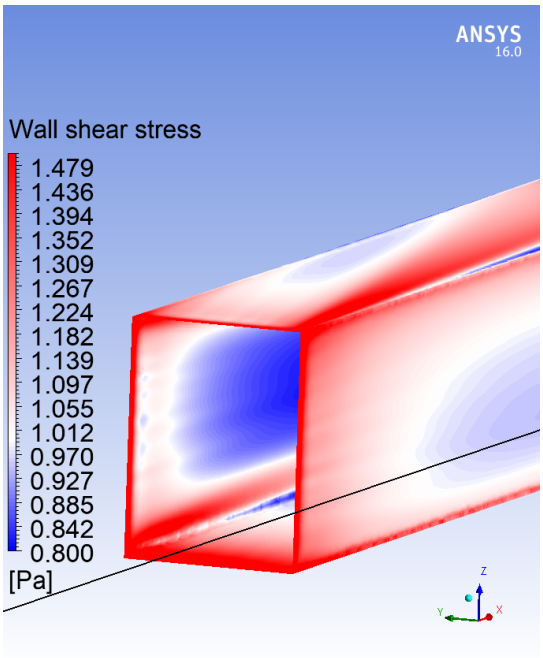


**Figure 4.13:** Wall shear stress (for ABL case with yaw) contours on the HDV's side surface (Black line marks the $z = z_{eq,yaw}$ line)

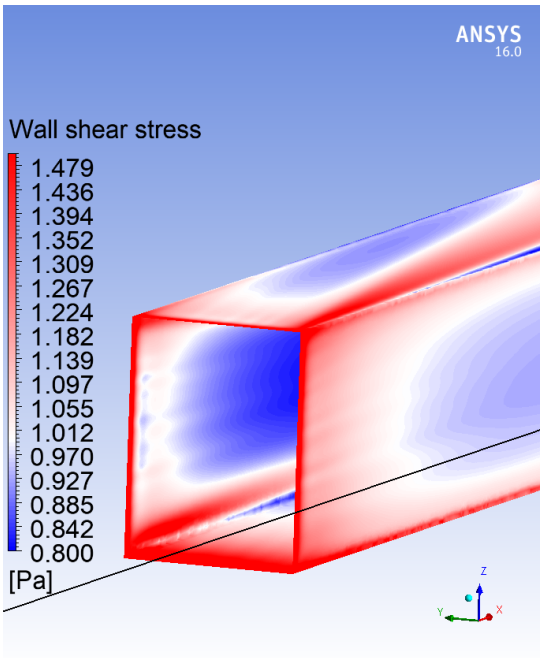


**Figure 4.14:** Wall shear stress (for 'No-ABL' case with yaw) contours on the HDV's side surface (Black line marks the $z = z_{eq,yaw}$ line)

Similar to the case without a wind yaw angle, Figures 3.30 and 3.31 show that the ABL case has higher wall shear stress above $z_{eq,yaw}$ than the 'No-ABL' case and lower wall shear stress below $z_{eq,yaw}$ due to the difference in velocities brought by $V_T(z)$ discussed before. Since the area above $z_{eq,yaw}$ is greater than the area below, this leads to 2.5 % higher side drag for the ABL case with yaw compared to the 'No-ABL' case.

Figure 4.13 shows that the wall shear stress trend behaves in a similar manner to what is shown in Figure 3.30. However, due to a non-zero wind yaw angle, the high wall shear stress lines which were along the corners of the HDV have shifted in the leeward direction, indicating the direction in which the boundary layer is progressing. Also, the leeward side faces lower wall shear stress compared to the windward side. This happens because a thicker boundary layer forms on the leeward side, compared to the windward side because of $\psi_{eq} = 5°$.

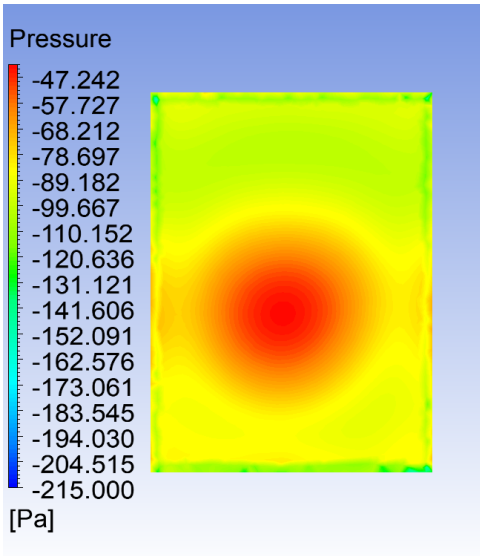


**Figure 4.15:** Pressure contours (for ABL case with yaw) on the HDV's rear surface

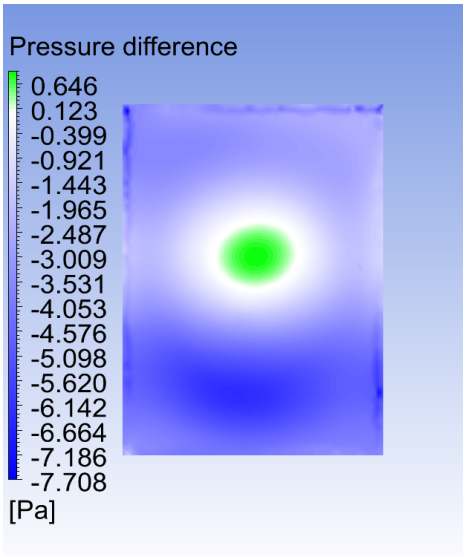


**Figure 4.16:** Pressure difference [p(ABL) - p('No-ABL')] contours on the HDV's rear surface

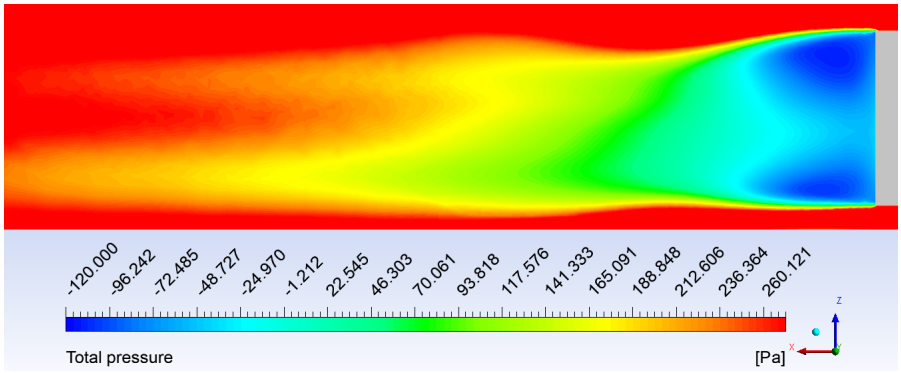


**Figure 4.17:** (Side view) Total pressure contours (for ABL case with yaw) near the HDV's wake region

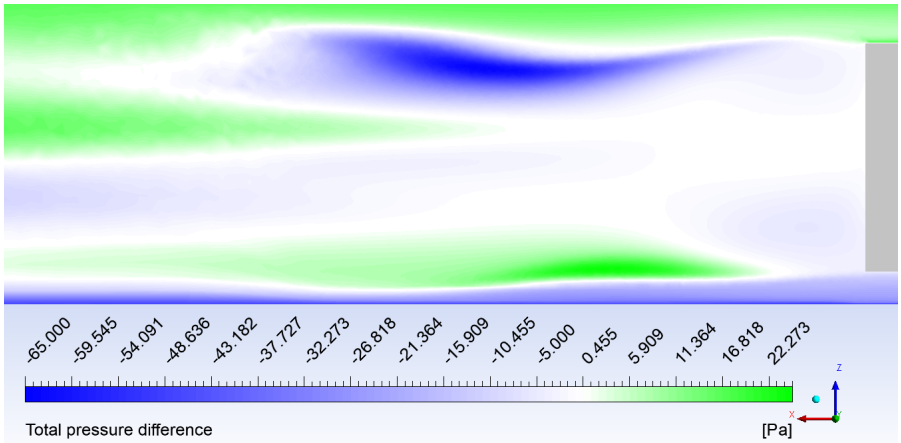


**Figure 4.18:** (Side view) Total pressure difference [$p_t$(ABL) - $p_t$('No-ABL')] contours near the HDV's wake region

The pressure peak on the rear surface shifts to the windward side when a wind yaw angle is applied as

shown in Figure 4.15. No change in size is observed. This is similar to the behaviour near the front surface , where higher pressures are observed in the windward side. This indicates that the wake region may have shifted in the windward direction.

Pressure difference trend on the rear surface shown in Figure 4.16 is similar to what is observed in Figure 3.37 where $\psi = 0$. Majority of the rear surface has lower pressures for the ABL case indicating the reason behind the 4 % higher rear drag for the ABL case (Table 4.1). The central region where the 'No-ABL' case has lower pressures has shrunk significantly with positive difference values being less than 1 $Pa$. This is the reason why the increase in rear drag for the non-zero yaw case is much higher (4 %) than the increase in rear-drag for the zero-yaw case (2 %).

Looking at Figure 4.18, the total pressure difference behaviour is different from what was observed in Figure 3.39. Not only is almost the entirety of the wake region experiencing lower total pressures by around 10 $Pa$ for the ABL case, the magnitude of the maximum negative difference has increased to 65 $Pa$ in Figure 4.18 from 21 $Pa$ in Figure 3.39. This again indicates why the rear drag significantly increases for the ABL case compared to the 'No-ABL' case.

The size of the vortices in the backflow region seem to have decreased in Figure 4.17, compared to Figure 3.38. However, the change observed in the $y = 0$ plane is not clearly discernible. Section 4.2.2 will represent figures in the $z = 2.25$ $m$ plane which is the mid-height of the HDV. This phenomenon will be more easily seen there.

Figure 4.19 when compared to Figure 3.32 show how the wake is influenced by a non-zero wind yaw angle. The vortices in the backflow region have reduced in size, similar to the total pressure plot in Figure 4.17. The streamwise extent of the wake region has reduced too.

Figure 4.20 again illustrates why the rear drag is higher for the ABL case. The decelaration for the ABL case is considerably higher as the magnitude of the maximum negative x velocity difference goes up to 2.6 $m/s$ from 0.85 $m/s$ in Figure 3.33. One can see traces of the ABL inflow effect where there is higher decalaration in the upper wake region and lower decelration in the lower wake region.

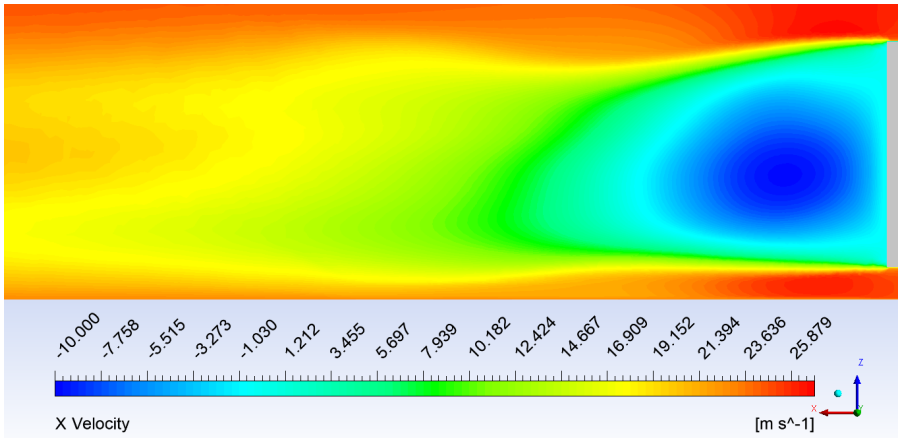


**Figure 4.19:** (Side view) X Velocity contours (for ABL case with yaw) near the HDV's wake region

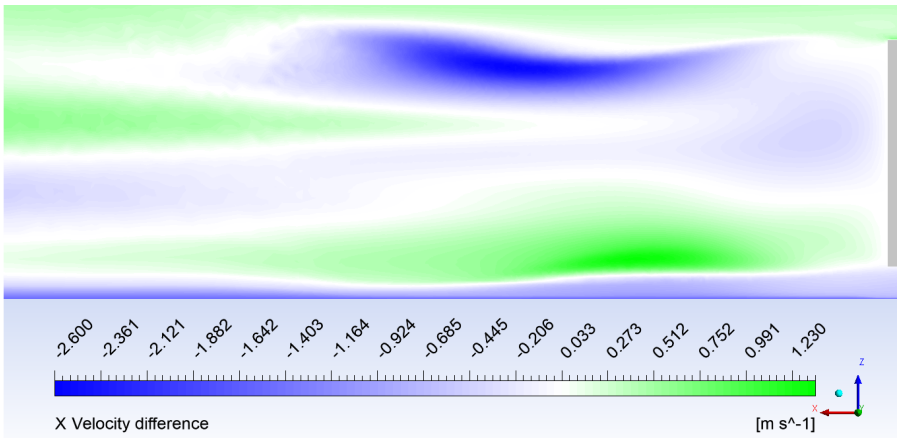


**Figure 4.20:** (Side view) X Velocity difference [$V_x$(ABL) - $V_x$('No-ABL')] contours near the HDV's wake region

## Drag force

| | Front drag (N) | Side drag (N) | Rear drag (N) | Drag (N) |
|---|---|---|---|---|
| **HDV with ABL and $\psi_{eq} = 5°$** | 68.5 | 208.8 | 791.2 | 1068.5 |
| **HDV with 'No-ABL' and $\psi_{eq} = 5°$** | 72.6 | 203.6 | 762.3 | 1038.6 |

**Table 4.1:** Values of drag force and its components for the non-zero yaw angle case

Front drag is 5.5% higher for the 'No-ABL' case because of higher pressures faced on the front surface by the 'No-ABL' case as shown in Figure 4.12. Side drag is 2.5% higher for the ABL case because of higher overall wall shear stress as shown in Figures 4.13 and 4.14. Rear drag is 4% higher for the ABL case because of higher overall deceleration in the wake region for the ABL case as shown in Figures 4.20 and 4.18. The increase in total drag for the ABL case is 3% higher than the 'No-ABL' case. However, one should look at the changes in the components of the drag force due to the introduction of a yaw angle and not at the total drag to understand the complete picture.

| **Drag force (N)** | $z > z_{eq,yaw}$ | $z < z_{eq,yaw}$ |
|---|---|---|
| **ABL and** $\psi_{eq} = 5°$ | 859.3 | 209.3 |
| **'No-ABL' and** $\psi_{eq} = 5°$ | 832.7 | 205.8 |

**Table 4.2:** Drag force faced by the HDV under $\psi_{eq} = 5°$ for $z > z_{eq,yaw}$ and $z < z_{eq,yaw}$

Table 4.2 shows that for $z > z_{eq,yaw}$, the ABL case with yaw faces higher drag, again due to higher velocities for $z > z_{eq,yaw}$. However, even for $z < z_{eq,yaw}$, it faces higher drag. This is because of the dominance of the rear drag for the ABL case in this region which can be understood by looking at the bottom portion of the rear surface in Figure 4.16. The ABL case has lower pressures of up to 7.5 $Pa$ compared to 'No-ABL' case in the bottom portion. The negative pressure difference in Figure 4.16 has a higher magnitude at $z < z_{eq,yaw}$, indicating that the rear drag difference between the two cases is higher at $z < z_{eq,yaw}$. Hence, for the region $z < z_{eq,yaw}$, the higher rear drag for the ABL case counteracts the higher side and front drag faced by the 'No-ABL' case.

## 4.2.2. Effect of non-zero $\psi$ on the ABL inflow

This section compares two cases where both face an ABL inflow but one case has a zero wind yaw angle and the other has an equivalent non-zero wind yaw angle $\psi_{eq} = 5°$. The difference between the two is brought solely by the wind yaw angle.

### Drag force

| | Front drag (N) | Side drag (N) | Rear drag (N) | Drag (N) |
|---|---|---|---|---|
| **HDV with ABL and** $\psi_{eq} = 0°$ | 122.2 | 212.3 | 796.2 | 1130.7 |
| **HDV with ABL and** $\psi_{eq} = 5°$ | 68.5 | 208.8 | 791.2 | 1068.5 |

**Table 4.3:** Values of drag force and its components for the ABL cases with and without yaw.

On first glance, it seems counter intuitive that including a non-zero wind yaw angle will decrease the total drag. However, there are multiple reasons behind this trend. Firstly, relevant literature focuses on $C_D$ values and not drag force values. This is because previous studies on the effect of yaw angle apply the yaw angle to the driving velocity due to which the reference velocity for the zero and non-zero yaw cases are same.

In our case, the yaw angle is applied solely to the wind velocity $V_w(z)$ and not to the driving velocity $V_{HDV}$. By using (4.5) and equating the mass flow through integration, the equivalent relative velocity faced by the HDV is calculated which is also used as the reference velocity. The non zero yaw case has a reference velocity of $V_{eq} = 24.6\ m/s$ while the zero yaw case has a reference velocity of $V_{eq} = 25.6\ m/s$. The lower reference velocity for the non-zero yaw case is one of the major factors behind lower drag for the non-zero yaw case. $C_D$ values are purposefully not used as the reference velocity for the non-zero yaw and zero yaw cases are different.

Also, Gheyssens [14] reports the increase in $C_D$ when a yaw angle of 3° is introduced for the GETS model. The total $C_D$ increases by 0.004, the rear $C_D$ increases by 0.005, the side $C_D$ increases by 0.002 and the front $C_D$ decreases by 0.002 when $\psi = 3°$ is introduced. These minute changes show that the GETS model is not very sensitive to a change in yaw angle unlike realistic geometries. One should note that the yaw angle was applied to the driving velocity in Gheyssens [14].

A major contribution from a lower reference velocity (as a result of the ABL inflow equations) and a minor contribution from the low sensitivity of the GETS model to a non-zero yaw angle has led to the above drag trend.

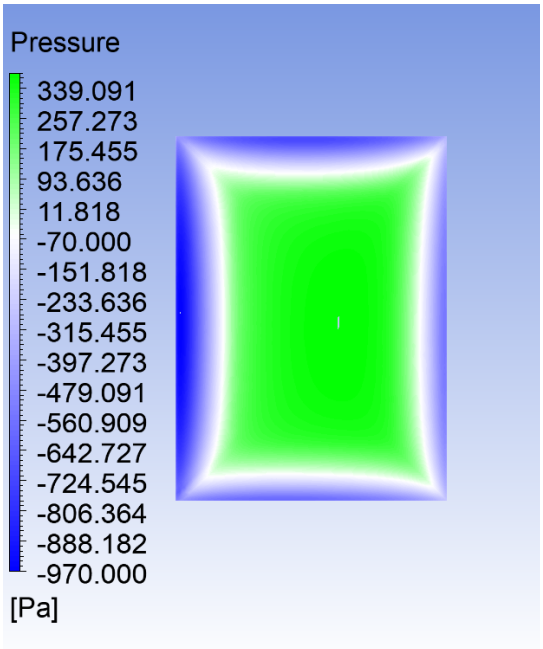


**Figure 4.21:** Pressure contours on the HDV's front surface (for ABL case with yaw)

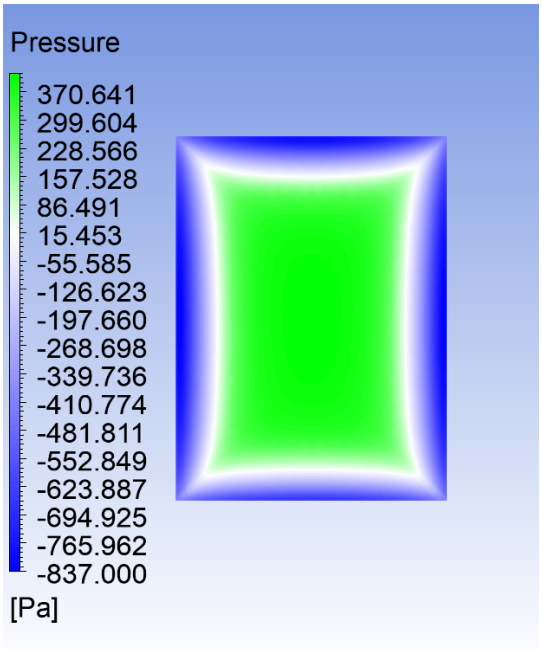


**Figure 4.22:** Pressure contours on the HDV's front surface (for ABL case without yaw)

Figure 4.21 shows that lower pressures are faced by the front surface when a non-zero wind yaw angle is introduced. Both the minimum and the maximum value of pressure on the front surface are lower for the non-zero yaw case, compared to Figure 4.22. This again shows why the zero yaw case faces 44% higher front drag.

By comparing Figure 4.23 to 4.24, one can notice that the zero yaw case has higher wall shear stress on the side surface. This is again caused by higher equivalent relative velocity faced by the HDV when $\psi = 0°$. This indicates why the $\psi_{eq} = 0°$ case has 1.5 % higher side drag force.

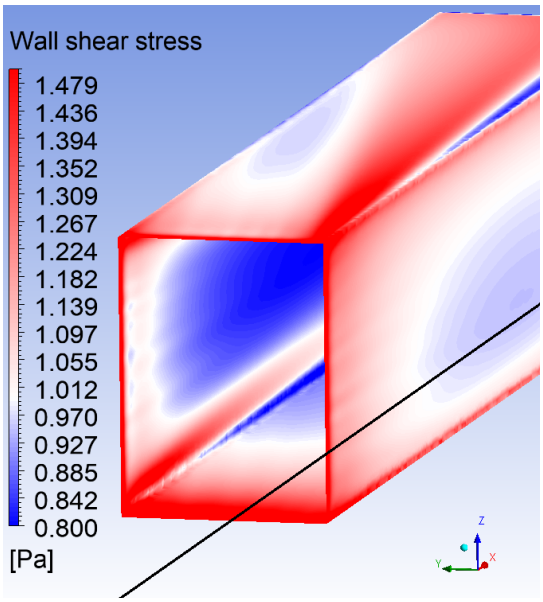


**Figure 4.23:** Wall shear stress contours on the HDV's side surface (for ABL case with yaw)

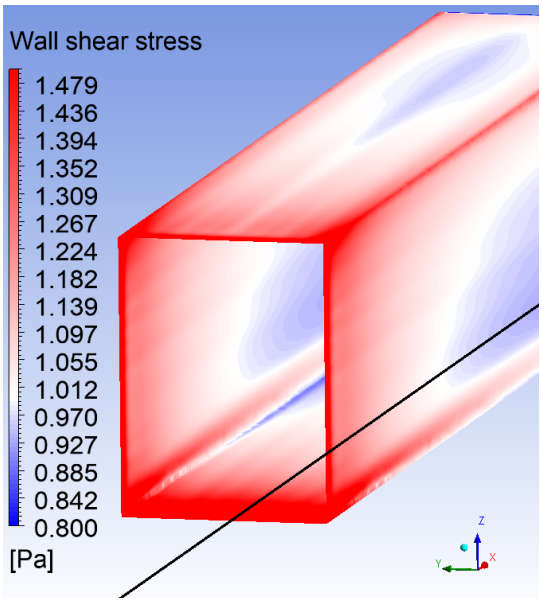


**Figure 4.24:** Wall shear stress contours on the HDV's side surface (for ABL case without yaw)

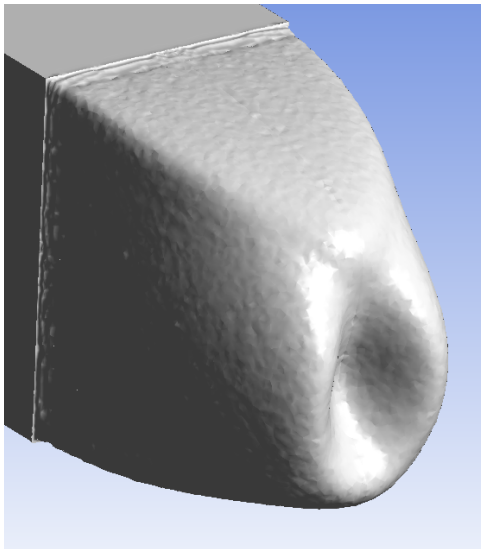

**Figure 4.25:** Isosurface of total pressure = 0 (for ABL case without yaw) behind the HDV's rear surface

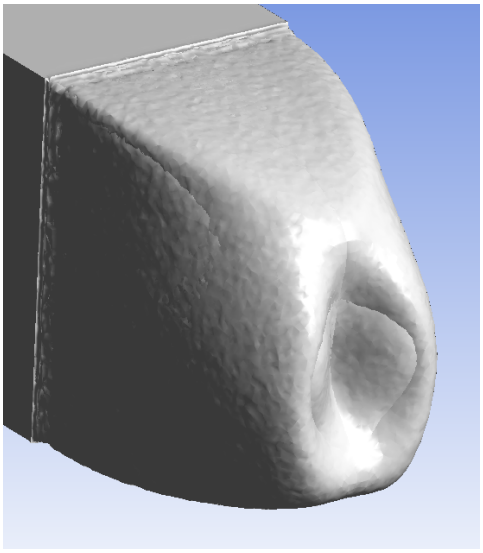

**Figure 4.26:** Isosurface of total pressure = 0 (for ABL case with yaw) behind the HDV's rear surface

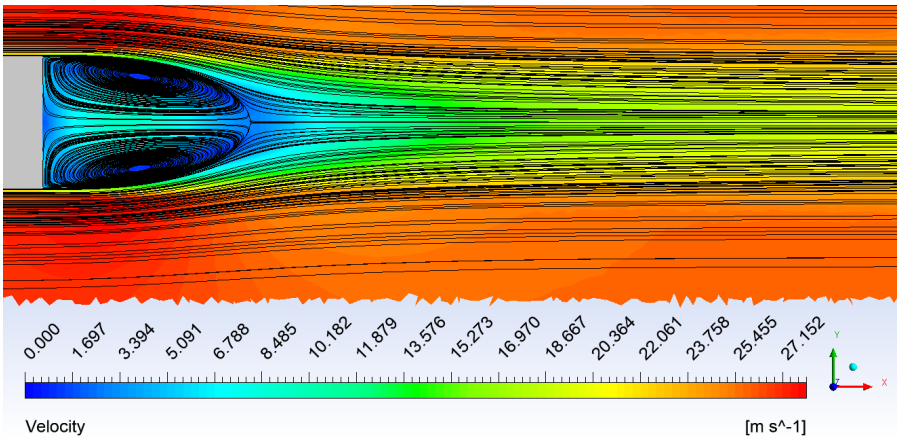


**Figure 4.27:** Velocity magnitude contours (for ABL case without yaw) in the $z = 2.25\ m$ plane i.e. mid-truck height (Top view)

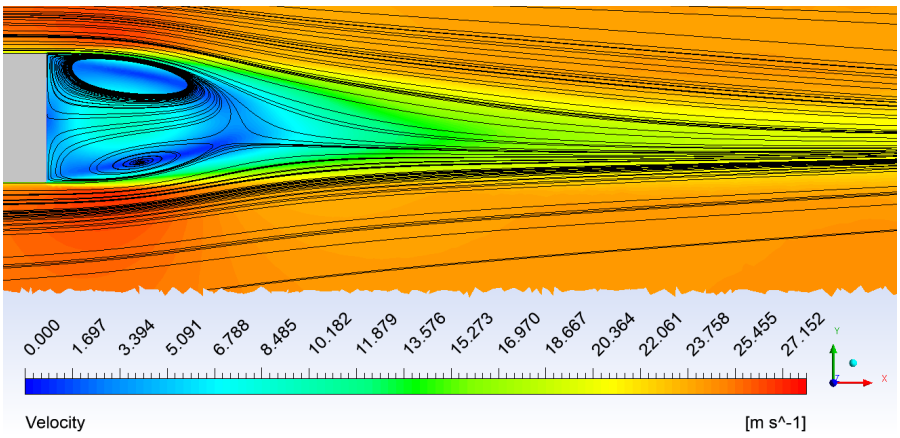


**Figure 4.28:** Velocity magnitude contours (for ABL case with yaw) in the $z = 2.25\ m$ plane i.e. mid-truck height (Top view)

0.5% higher rear drag for the $\psi_{eq} = 0°$ observed in Table 4.3 occurs because both the wake vortex size and the streamwise wake size reduce for the $\psi_{eq} = 5°$ case. Figure 4.26 and 4.28 show the reduced wake vortex size when compared to Figure 4.25 and 4.27 respectively. This occurs mainly because the non-zero $\psi(z)$ reduces the equivalent relative velocity faced by the vehicle. This can also be observed by comparing the freestream region in Figures 4.27 and 4.28. The non-zero $\psi$ case has lower freestream velocity magnitude.

Figure 4.28 also shows that the wake region shifts to the windward side. This coincides with the shifting of the pressure peak on the rear surface shown in Figure 4.15. Gheyssens [14] also reports the shifting of the wake in the direction opposite to where the cross wind is coming from i.e. the negative y-direction in our case.

### 4.2.3. Effect of an attached boat-tail ($\psi_{eq} = 5°$)

Figure 4.29 shows that the pressure peak on the boat-tail's rear surface barely shifts to the windward side compared to Figure 4.15 when no boat-tail was attached.

Figure 4.30 when compared to 4.16 reduces the differences brought by the ABL inflow, as was observed for the cases without the wind yaw angle. The ABL case faces lower pressures over the entire boat-tail rear surface than the 'No-ABL' case. The rear surface pressure differences increase from up to 2 $Pa$ for the zero $\psi$ case to 4.5 $Pa$ for the non-zero $\psi$ case.

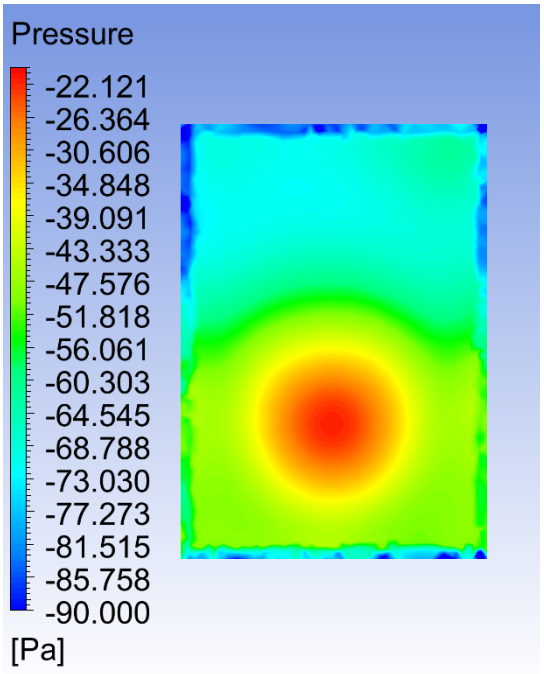


**Figure 4.29:** Pressure contours (for ABL case with yaw) on the boat-tail's rear surface

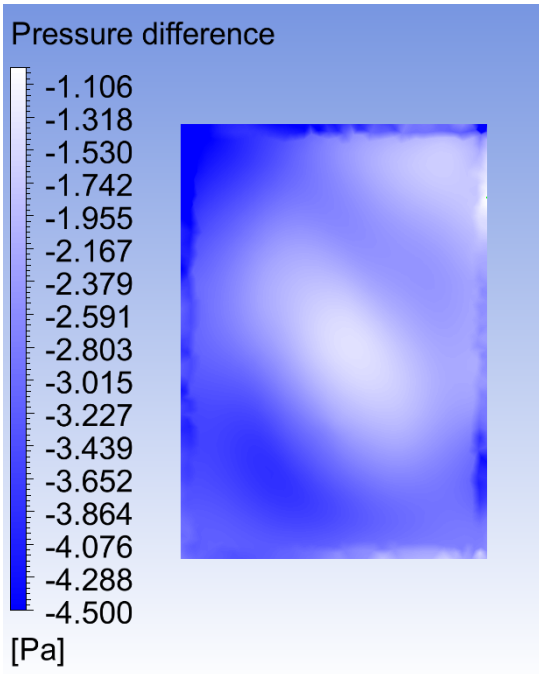


**Figure 4.30:** Pressure difference [p(ABL) - p('No-ABL')] contours on the boat-tail's rear surface

Compared to Figure 3.50, Figure 4.31 shows that the wake vortex decreases in size when a wind yaw angle is applied, similar to the cases where no boat-tail was present. Figure 4.32 shows that in the wake region, differences between the ABL and 'No-ABL' region are negligible. Compared to Figure 4.20, the differences are even less. This again shows that the boat-tail functions in a way which reduces the effect of the ABL inflow. Once reattachment begins, effect of the ABL inflow begins resurfacing which can be observed in the gradient in the upper left corner of Figure 4.32.

The reduction of the wake size when a non-zero $\psi$ is introduced, which is observed by comparing Figures 3.32 and 4.19 is reduced by the boat-tail when we compare Figures 3.50 and 4.31.

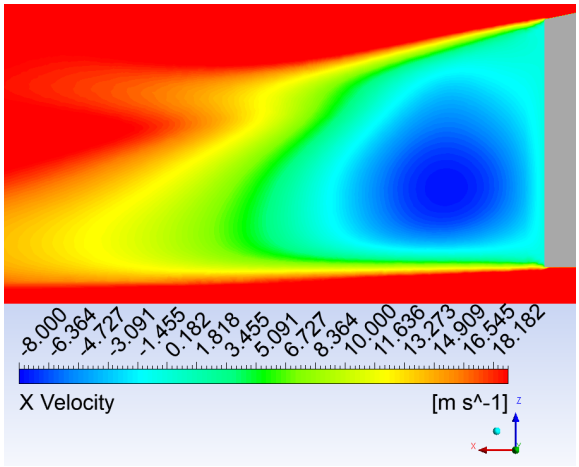


**Figure 4.31:** (Side view) X Velocity contours (for ABL case with yaw) near the boat-tail's wake region

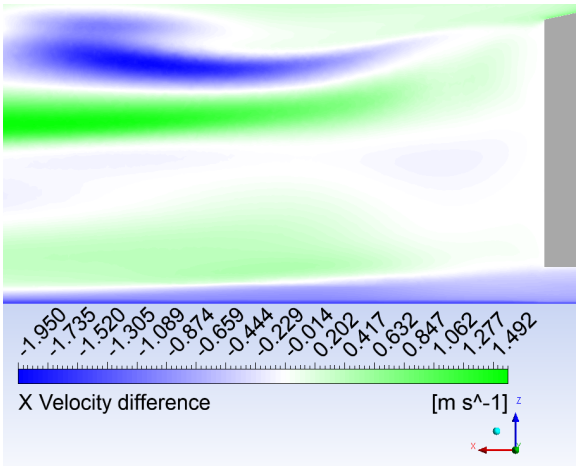


**Figure 4.32:** (Side view) X Velocity difference [$V_x$(ABL) - $V_x$('No-ABL')] contours near the boat-tail's wake region

### Drag force reduction

| | **Drag (N)** | **Drag reduction caused by boat-tail** |
|---|---|---|
| **ABL with boat-tail** | 858.6 | 20 % |
| **'No-ABL' with boat-tail** | 830.6 | 20 % |

**Table 4.4:** Drag force and drag reduction experienced by both the ABL and 'No-ABL' cases when a boat-tail is attached

Table 3.8 shows the drag forces attained when a boat-tail is attached to both the ABL and 'No-ABL' cases facing a non-zero wind yaw angle $\psi_{eq} = 5°$. With an attached boat-tail, the drag force for the ABL case is 858.6 $N$ while for the 'No-ABL' case is 830.6 $N$. The decrease in $C_D$ with the attachment of a boat-tail is 20 % for the ABL case and 20 % for the 'No-ABL' case. This again means that the use of ABL as an inflow has a very minute, practically negligible effect on the drag-reducing capabilities of the boat-tail, even when a wind yaw angle is applied.

## 4.3. Summary

1. The introduction of a non-zero wind yaw angle brings changes to the drag trends of the HDV by mainly shifting high pressures on the front stagnation region to the windward side, reducing the size of the wake vortex and shifting the wake region to the windward side.

2. When this effect is combined with the ABL inflow effect, trends which were seen in the $\psi = 0°$ case are altered. Near the front surface, the non-zero wind yaw angle decreases the front drag by 44% (when both cases have an ABL inflow) and the ABL inflow decreases the front drag by 5.5% (when both cases face $\psi_{eq} = 5°$). This change in trend is due to the shifting of the high and low pressure zones near the front surface in the y-direction.

3. Side drag changes are observed in the wall shear stress difference contours. The differences are brought in due to the difference in velocity magnitude experienced, between the various cases.

4. Rear drag is decreased due to a decreased wake size when $\psi_{eq} = 5°$ is introduced. However, the difference between the ABL and 'No-ABL' cases increases when a wind yaw angle is introduced. This is because of much higher decelaration for the ABL case in the wake region when $\psi_{eq} = 5°$.

5. The difference in the wake region brought by $\psi_{eq} = 5°$ is also reduced when a closed boat-tail is introduced. This can be observed by the negligible movement of the pressure peak in the windward direction on the boat-tail's rear surface and the less than expected wake size reduction for $\psi_{eq} = 5°$ compared to the cases where no boat-tail was attached.

# 5

# Conclusion, recommendations and limitations

This chapter discusses the effect of the mechanisms discussed in the previous chapters and tries to answer the research questions posed in the literature review through the findings in this study.

## 5.1. Conclusion

### 5.1.1. ABL development

The development of the ABL is sufficiently minimised till 10 m in front of the HDV, where the maximum deviation from the inlet profile is just 2%. This has been possible even after violating (2.1) stated by Blocken [4]. This is why (2.1) and (2.2) are guidelines stated by Blocken and are not strict rules to be followed. For minimal development of the input ABL profile, a number of factors are important such as the turbulence model used, wall functions, values of $y_P, k_S, C_s$ and top and outlet boundary condition. For $z_O = 0.1\ m$, $k_S = 0.9793m$ is used by following (2.2). High turbulence intensity of 5 % and high turbulent length scale of 5 $m$ is chosen. As one proceeds in the positive streamwise direction, from 10 m in front of the HDV to right in front of the HDV, the development experienced by the ABL profile is majorly due to the presence of the HDV.

### 5.1.2. Zero $\psi$ case

Starting with the ABL inflow effect, under zero $\psi$, the change in the components of drag are driven by a higher overall pressure distribution on the front surface stagnation region, higher overall wall shear stress on the side surfaces and lower overall pressure distribution on the rear surface. For the front and side surfaces, this is caused by velocity differences brought by the ABL profile. For the rear surface, the mechanism behind the lower pressure distribution is unclear. It is tough to pinpoint the exact mechanism behind this as the flow in this region is highly viscous and a RANS solver may not be the best method to figure out the reason behind it.

In the wake region, the ABL inflow condition reshapes the vortices in the backflow region in such a way that the upper vortex increases in size while the lower vortex decreases in size. This might be understood by looking at the vorticity difference contours which suggest higher vorticity for the ABL case near the upper free shear layer separating from the HDV rear surface and lower vorticity for the ABL case near the lower free shear layer. This leads to higher decelaration for the ABL case in the upper wake region and lower decelaration in the lower wake region. Since the upper vortex in the backflow region is usually larger than the lower vortex, a major portion of the wake faces higher decelaration and thus lower velocities for the ABL case. This explains why the rear drag is 2% higher for the ABL case. Considering total drag, the ABL case faces 3.5% higher drag than the 'No-ABL' case.

The attachment of the particular boat-tail configuration used reduces the ABL inflow effect by reducing the differences between the ABL and 'No-ABL' case. Effectively, the boat-tail significantly reduces the upper wake vortex size and moderately reduces the lower vortex size. This dominates over the ABL inflow effect. The drag reduction percentage by the boat-tail is 20 % for both the ABL and 'No-ABL' cases. Hence, one can conclude that the drag reduction efficiency of the boat-tail is unaffected by the ABL inflow.

### 5.1.3. Non-zero yaw case

A non-zero equivalent yaw angle of 5° is applied to the wind velocity profile $V_w(z)$. Due to this, both velocity and the yaw angle vary in the z-direction. This shifts the high pressure core near the front surface stagnation region to the windward side. The low pressure cores near the side curved radius become asymmetrical in the y-direction. The leeward side curved radius has a larger low pressure core and the windward side curved radius has a smaller low pressure core compared to the zero yaw case. The wake region shifts windward and also reduces in size. The pressure peak on the rear surface shifts to the windward side.

Due to the non-zero yaw angle, the effect of the ABL inflow gets altered. The front surface faces lower pressures for the ABL case. The side and rear surface on the other hand follow a similar trend as the zero yaw case, having higher wall shear stress and lower pressures on the rear surface for the ABL case. This leads to 5.5% lower front drag and 2.5% higher side and 4% higher rear drag for the ABL case. The increase in total drag for the ABL case is 3 % higher than the 'No-ABL' case.

On comparing the ABL cases with zero and non-zero yaw, the front drag decreases by 44% while the side and rear drag decrease by 1.5% and 0.5% . This is because the non-zero yaw case faces lower pressure on the front surface, lower wall shear stress on side surface and a smaller wake region indicating less deceleration. A major reason behind this is the lower equivalent velocity of 24.6 $m/s$ faced by the non-zero yaw case compared to 25.6 $m/s$ for the zero-yaw case. Also, the results expected are different from what is observed in literature because the yaw angle is applied solely to the wind velocity $V_w(z)$ and not the driving velocity $V_{HDV}$.

The introduction of a boat-tail combined with a non-zero yaw angle reduces the ABL inflow effect but not as significantly as was observed for the zero yaw case. The drag reduction by the boat-tail for the ABL and 'No-ABL' cases under yaw are approximately 20 %. This means that the ABL inflow brings a very minute difference in the drag reduction efficiency of the boat-tail even with non-zero $\psi$.

The changes brought in by the ABL inflow are overall minute. Qualitatively, differences are observed. However, quantitatively, it is difficult to ascertain the magnitude of change brought in by the ABL inflow. The ABL and 'No-ABL' cases differ only at the inflow with maximum velocity magnitude differences of only 2.5 $m/s$. Hence, differences in the flow field are expected to be small. At the same time, discretisation errors may lead to changes in the differences observed between the two cases and a shift from positive difference to negative difference (and vice versa) may be observed. When the value of the difference of any physical variable is multiple orders below the order of the physical variable itself, it is possible that the difference is a result of discretisation error and does not physically exist. Nevertheless, the differences observed can be explained physically and are not a result of solely discretisation error.

## 5.2. Limitations and/or recommendations

1. To be able to make a comparison between the ABL and 'No-ABL' cases, all settings were kept the same apart from the inlet profile, top and floor boundary condition. This way, we can attribute any changes experienced in the flow to the ABL inflow effect. However, this thesis focuses on the overall impact of realistic conditions on the drag force by using settings such as high turbulence intensity, high turbulence length scale and wall roughness which are usually not considered in traditional simulations of flow across an HDV. Each of these factors has a contribution to the flow field experienced and the drag force calculated in this thesis for the ABL cases have taken all of these settings into account. All these factors together will make a considerably bigger difference than what is observed in the thesis. Considering future work, one should study the effect of each of these factors and then compare CFD simulations with traditional settings to the ABL inflow simulations.

2. The ABL inflow and non-zero yaw angle effect will have greater implications on realistic geometries which contain tractor-trailer gap, side mirrors, underbody geometry etc. Higher or lower pressures on these key parts of an HDV can contribute to greater changes in the drag.

3. To truly be able to compare the zero yaw and non-zero yaw cases, one needs to ensure that both cases face a flow of equal equivalent relative velocity. The minute difference in the side drag will definitely change in such a case.

4. For the sake of simplicity, constant values of turbulent length scale and turbulent intensity are used at the inlet. However apart from the velocity profile, the turbulence intensity and the turbulence length scale also vary in height in an ABL. Future studies on the effect of ABL on the aerodynamics of an HDV should take this into account.

5. The equivalent velocity is calculated by equating the mass flow over the vehicle height for the ABL and 'No-ABL' cases. However, important aerodynamic phenomena occurs not only over the height of the HDV but also slightly above (boundary layer growth) and below (underbody effect in case of a geometry more complex than the GETS model). One should have equal mass flow slightly above and below the HDV model too. Ideally, mass flow should be equated from the bottom to the vertical point at which the ABL is no longer affected by the presence of the truck.

6. By employing $z_O$ type wall functions such as those described by Richard [31], one can eliminate the need to employ $k_S$ because the roughness is expressed directly in terms of $z_O$ instead of $k_S$. One no longer needs to adhere to guidelines suggested by Blocken then. However, these wall functions have only been obtained for the standard $k-\epsilon$ model and need to be reconfigured for other turbulence models.

7. Since the differences induced by the ABL inflow in the flow field across the HDV are small, statistical analysis indicating how significant the data is, shall help in determining the confidence interval of the calculated values such as the drag forces.

# Bibliography


[1] Bluff body flow - wake behavior behind a heated circular cylinder. Technical report, Jan-Jaap Mastenbroek, 2010.

[2] Surface vehicle recommended practice. Technical report, SAE, 2013.

[3] J.D. Anderson. *Fundamentals of Aerodynamics*. McGraw Hill, 2001.

[4] Stathopoulos T. Carmelieta J.0 Blocken, B. Cfd simulation of the atmospheric boundary layer: wall function problems. *Atmospheric Environment*, 2007.

[5] Guido Buresti. Bluff-body aerodynamics, June 2000.

[6] Campbell W.F. Cooper, K. R. An examination of the effects of wind turbulence on the aerodynamic drag of vehicles. *Journal of Wind Engineering and Industrial Aerodynamics*, 1981.

[7] Kevin R. Cooper. Improving the wind tunnel simulation of surface vehicles and the interpretation of wind tunnel data. In *Aerodynamics: Wind Tunnel Construction, Testing and Calculations TOPTEC*, 1999.

[8] K.R. Cooper. The effect of front-edge rounding and rear- edge shaping on the aerodynamic drag of bluff vehicles in ground proximity. *SAE TECHNICAL PAPER SERIES*, 1985.

[9] K.R. Cooper. Truck aerodynamics reborn - lessons from the past. *SAE TECHNICAL PAPER SERIES*, 2003.

[10] Watkins S. Cooper, K. R. The unsteady wind environment of road vehicles, part two: Effects of vehicle development and simulation of turbulence. *SAE TECHNICAL PAPER SERIES*, 2007.

[11] George A.R. Duell, E.G. Experimental study of a ground vehicle body unsteady near wake. *SAE TECHNICAL PAPER SERIES*, 1999.

[12] eurostat. Greenhouse gas emissions by ipcc source sector, eu-28, 2016. `https://ec.europa.eu/eurostat/statistics-explained/index.php?title=Climate_change_-_driving_forces`.

[13] ANSYS Fluent. Ansys fluent 12.0 theory guide. `https://www.afs.enea.it/project/neptunius/docs/fluent/html/th/main_pre.htm`.

[14] T. Gheyssens. *Aerodynamic analysis of a platoon of bluff bodies subjected to cross wind*. PhD thesis, Technische Universtiteit Delft, 2016.

[15] Chauhan K. et al Hutchins, N. Towards reconciling the large-scale structure of turbulent boundary layers in the atmosphere and laboratory. *Boundary Layer Meteorology*, 2012.

[16] American Transportation Research Institute. Sustainable vehicle practices. `https://truckingresearch.org/sustainable-vehicle-practices-2/`.

[17] F. Kruijssen. *The effect of asymmetric base flaps on the drag of a tractor-trailer for four crosswind angles*. PhD thesis, Delft University of Technology, 2017.

[18] Marco Lanfrit. Best practice guidelines for handling automotive external aerodynamics with fluent. Technical report, Fluent Deutschland GmbH, 2005.

[19] Søren Ejling Larsen. *The atmospheric boundary layer over land and sea: Focus on the off-shore Southern Baltic and Southern North Sea region*. PhD thesis, Technical University of Denmark, 2013.

[20] W. Solecki F. Aragon–Durand W. Cramer S. Humphreys M. Kainuma J. Kala N. Mahowald Y. Mulugetta R. Perez M. Wairiu K. Zickfeld M. Allen, O. P. Dube. Global warming of 1.5°c, 2018.

[21] MATLAB. How the genetic algorithm works. https://nl.mathworks.com/help/gads/how-the-genetic-algorithm-works.html.

[22] B.R. et al McAuliffe. Measurement of the on-road turbulence environment experienced by heavy duty vehicles. *SAE International*, 2014.

[23] Axelle Viré Michiel Zaaijer. Introduction to wind turbines: physics and technology.

[24] R. Muncrief and B. Sharpe. Overview of the heavy-duty vehicle market and co2 emissions in the european union. *International Council on Clean Transportation*, 2015.

[25] NASA. The drag equation. https://www.grc.nasa.gov/www/k-12/airplane/drageq.html.

[26] J. Ortega and K. Salari. An experimental study of drag reduction devices for a trailer underbody and base. *AIAA Journal*, pages 2004–2252, 2004.

[27] Prayash Panda. Determination of standard values of yaw angle and exponent for the atmospheric boundary layer profile at vehicle height. 2018.

[28] Harms T.M. Pieterse, J.E. Cfd investigation of the atmospheric boundary layer under different thermal stability conditions. *Journal of Wind Engineering and Industrial Aerodynamics*, 2013.

[29] S.B. Pope. *Turbulent Flows*. Cambridge University Press, 2013.

[30] Gandert Marcel Rita VAN RAEMDONCK. *Design of Low Drag Bluff Road Vehicles*. PhD thesis, Technische Universtiteit Delft, 2012.

[31] Hoxey R.P. Richards, P.J. Appropriate boundary conditions for computational wind engineering models using the k–e turbulence model. *Journal of Wind Engineering and Industrial Aerodynamics*, 1993.

[32] Lily Hoffman-Andrews Thomas Curry, Isaac Liberman and Dana Lowell. Reducing aerodynamic drag and rolling resistance from heavy-duty trucks: Summary of available technologies and applicability to chinese trucks. *International Council on Clean Transportation*, 2012.

[33] Riley S. et al Toloui, M. Measurement of atmospheric boundary layer based on super-large-scale particle image velocimetry using natural snowfall. *Experiments of Fluids*, 2014.

[34] Lundtang Petersen Erik Troen, Ib. *European Wind Atlas*. Ris National Laboratory, Roskilde, 1989.

[35] Arkady Tsinober. Fundamental and conceptual aspects of turbulent flows.

[36] N.J.G. van Dijk. *THE EFFECT OF THE ATMOSPHERIC BOUNDARY LAYER ON TRUCK AERODYNAMICS WITH NUMERICAL INVESTIGATIONS*. PhD thesis, University of Twente, 2016.

[37] P.M. van Leeuwen. *Computational Analysis of Base Drag Reduction Using Active Flow Control*. PhD thesis, TU Delft, 2009.

[38] van Tooren M.J. Van Raemdonck G.M. *Data Acquisition of a Tractor-Trailer Combination to Register Aerodynamic Performances*. Springer, Berlin, Heidelberg, 2009.

[39] Ed. Chen Wai-Fah. *Structural Engineering Handbook*. CRC Press, 1999.

[40] Saunders-J. Watkins, S. A review of the wind conditions experienced by a moving vehicle. *SAE TECHNICAL PAPER SERIES*, 1998.

[41] F.M. White. *Viscous fluid flow*. McGraw-Hill, 2006.

[42] Richard M. Wood. A discussion of a heavy truck advanced aerodynamic trailer system. Technical report, SOLUS-Solutions and Technologies LLC.

[43] S. Wordley and J. Saunders. On-road turbulence. *SAE TECHNICAL PAPER SERIES*, 2008.

# A

# Additional computational results

## A.1. Vorticity magnitude contours

This section presents the vorticity magnitude and vorticity magnitude difference contours for the various cases explored in this study.

### A.1.1. HDV with ABL inflow ($\psi = 0°$)

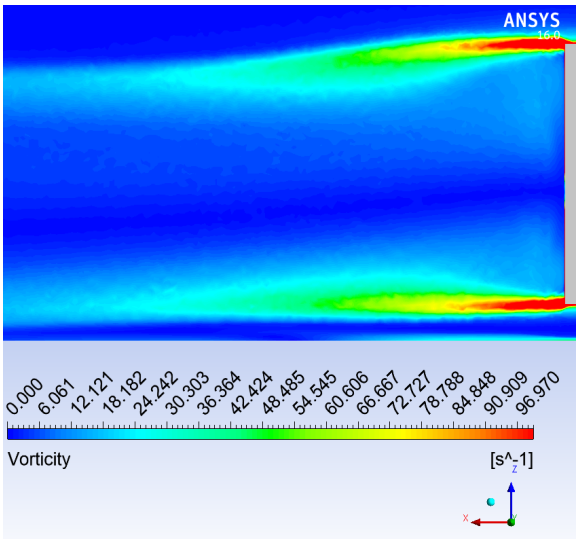


**Figure A.1:** (Side view) Vorticity magnitude contours (for ABL case) near the HDV's wake region (y = 0 plane)

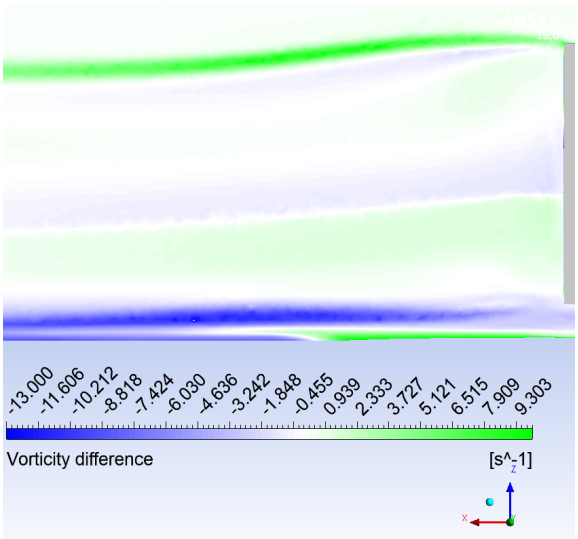


**Figure A.2:** (Side view) Vorticity magnitude difference [$|\omega|$(ABL) - $|\omega|$('No-ABL')] contours near the HDV's wake region (y = 0 plane)

### A.1.2. HDV with ABL inflow and attached boat-tail ($\psi = 0°$)

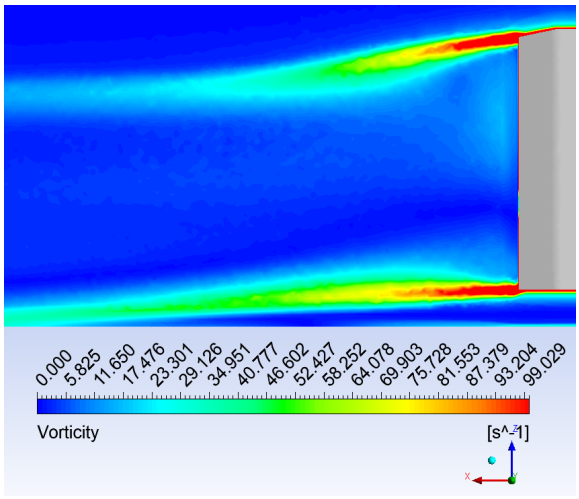


**Figure A.3:** (Side view) Vorticity magnitude contours (for ABL case) near the tail's wake region (y = 0 plane)

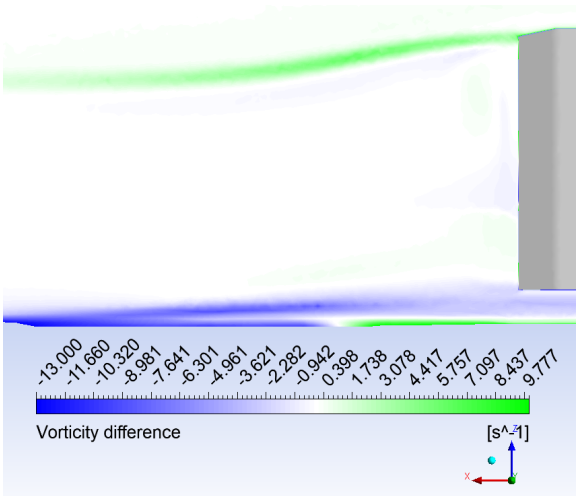


**Figure A.4:** (Side view) Vorticity magnitude difference [|$\omega$|(ABL) - |$\omega$|('No-ABL')] contours near the tail's wake region (y = 0 plane)

### A.1.3. HDV with ABL inflow ($\psi_{eq} = 5°$)

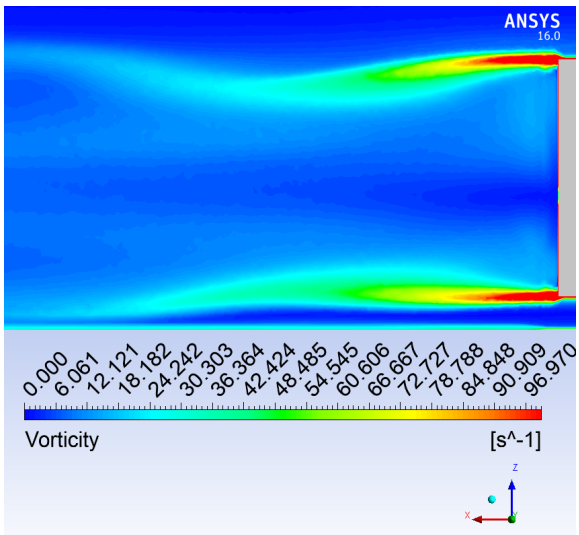


**Figure A.5:** (Side view) Vorticity magnitude contours (for ABL case with yaw) near the HDV's wake region (y = 0 plane)

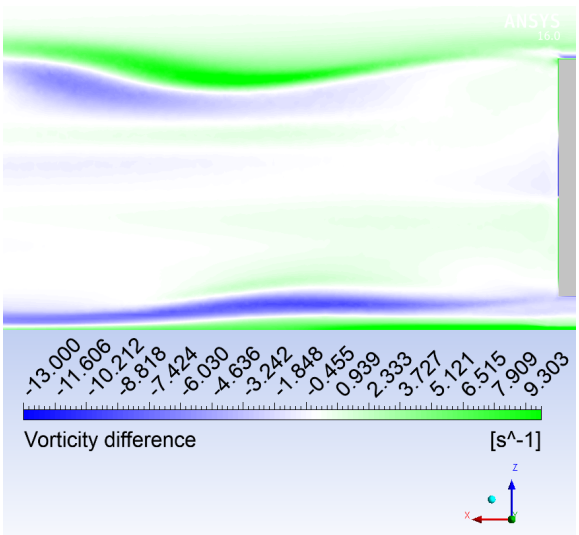


**Figure A.6:** (Side view) Vorticity magnitude difference [|$\omega$|(ABL) - |$\omega$|('No-ABL')] contours near the HDV's wake region (y = 0 plane)

### A.1.4. HDV with ABL inflow and attached boat-tail ($\psi_{eq} = 5°$)

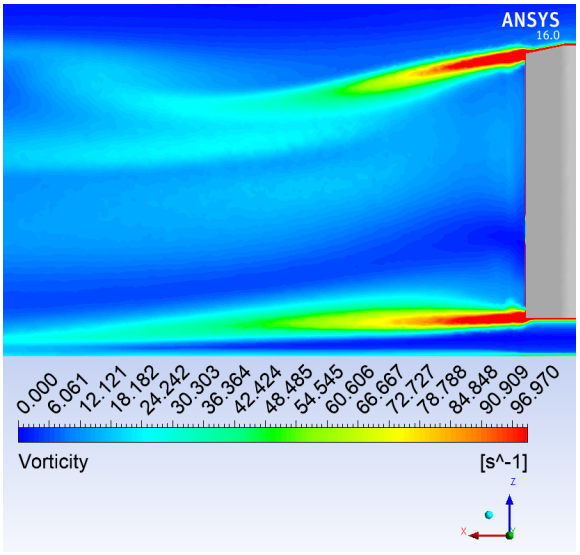


**Figure A.7:** (Side view) Vorticity magnitude contours (for ABL case) near the tail's wake region (y = 0 plane)

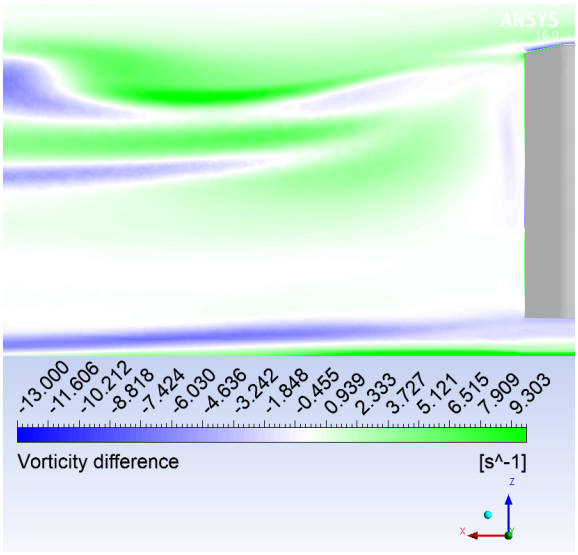


**Figure A.8:** (Side view) Vorticity magnitude difference [$|\omega|$(ABL) - $|\omega|$('No-ABL')] contours near the tail's wake region (y = 0 plane)